Dissertation

Biosensing for the analysis of raw milk

Claudia García

Biosensing for the analysis of raw milk

Vom Fachbereich für Physik, Elektrotechnik
der Universität Bremen

zur Erlangung des akademischen Grades eines
DOKTORS DER INGENIEURWISSENTSCHAFTEN
(Dr.-Ing.)

genehmigte Dissertation

von
Dipl.-Ing. Claudia García
wohnhaft in Berlin

Referent: Prof. Dr.-Ing. Walter Lang
Korreferent: Prof. Dr. rer. nat. Carsten Harms

This thesis is dedicated to my strongest and
so courageous brother.
Te amo Jay!

Abstract

Appropriate methods for monitoring raw milk in food sectors are required in order to prevent health-related issues from consuming milk or fermented dairy products such as cheese and yogurt. Conventional systems used for this purpose require sophisticated instruments, highly technical staff and several days to yield an estimated contaminant concentration profile. Currently, there is no technology available for fast and sensitive identification of unwanted substances that evidences several concentration levels in raw milk. As a contribution to the progress of innovative biochemical sensing systems, this thesis presents the design, development and construction of a prototype, which combines the expertise of sensitive immunoassay process with micro total analysis system (μTAS) to identify specific compounds encountered in raw milk.

Since the concept of μTAS appeared, the development of microfluidic devices and their application have increased enormously. Microfluidic devices offer a highly efficient platform for analysis of biomolecules due to the capacity for manipulating small amounts of liquid quickly and with high precision. Particle size estimation, particle separation, cell collection, manipulation and cell detection are some of many functions which could be performed through microfluidic systems. Based on these advantages, microfluidic devices in combination with an associated immunoassay system were used in the prototype to concentrate contamination patterns or specific compounds encountered in raw milk. The NANODETECT prototype developed in this thesis should provide an economic, efficient and sensitive platform for multicomponent detection of specific substances in raw milk without requiring sophisticated instruments and trained staff.

This thesis was performed for the European project NANODETECT (Development of nanosensors for the detection of quality parameters along the food chain) funded by European Commission within the 7th framework program.

Contents

Contents

Acronyms

Ab Antibody

Ab* Labeled Antibody

AB Anti-Mecoprop

AFM1 Aflatoxin M1

Ag Antigen

Ag* Labeled Antigen

Ar Argon

BIBIS Bremerhaven Institute for Biological Information Systems

Biocult Biocult B.V. Antibody Production Contract House

BioMEMS Biological Micro Electro Mechanical Systems

BSA Bovine Serum Albumin

CFD Computational Fluid Dynamics

CFU Colony Forming Unit

COC Cyclic Olefin Copolymer

CVD Chemical Vapor Deposition

De Dean number

DRIE Deep Reactive Ion Etching

E Energy

EC European Commission

ELISA Enzyme-Linked ImmunoSorbent Assay

em. Emission

exc. Excitation

Contents

FERA The Food and Environment Research Agency

FIA Fluorescence Immunoassay

FITC Fluoresceinisothiocyanat

FWHM Full Width at Half Maximum

GBL butyrolactone

GPIO General Purpose Input Output

GUI Graphical User Interface

h Plank Constant

HPLC High-pressure Liquid Chromatography

HRP Horseradish Peroxidase

LAN Local Area Network

LOC Lab-on-a-Chip

LOD Limit of Detection

LSM Confocal Laser Microscope

MAb Monoclonal Antibodies

MEMS Micro Electro Mechanical Systems

MGLANG Meiereigenossenschaft Langenhorn e.V.

NorayBio Noray Bioinformatics S.L.

Optotek Optotek d.o.o. Laser and optical technology

PAG Photo Acid Generator

PBS Phosphate Buffered Saline

PBS Phosphate Buffered Saline Triton

PC Polycarbonate

PDMS Polydimethylsiloxan

PE Polyethylene

Pe Peclet Number

Photoresist 1002F Epoxy-based Negative Photoresist

PMMA Polymethylmethacrylate

PMMA GS PMMA produced by Casting Fabrication

PMMA XT PMMA produced by Extrusion Fabrication

PMT Photomultiplier Tube

PP Polypropylene

PPB Parts Per Billion

PPS Photopatternable Silicon

PPSU Polyphenylene Sulphone

PS Polystyrene

PVD Physical Vapor Deposition

Re Reynolds Number

Rel.Err Relative Error

Resin 1002F Epoxy-based Resin

RIE Reactive Ion Etching

RIA Radio Immunoassay

RIKILT RIKILT, Institue of Food Safety

RINY Formargeria Granja Rinya S.L.

R-PE R-Phycoerythrin

Sa Surface Roughness Averages

SDS Sodium Dodecyl Sulfate

SEM Scanning Electron Microscope

SPI Serial Periperal Interface

SU-8 Epoxy-based Negative Photoresist

St.Dev. Standard Deviation

STEC Shiga Toxin-producing Escherichia Coli

Sz Mean Depth of Roughness

TMB Tetramethylbenzidine

Contents

ttz Technologie-Transfer-Zentrum Bremerhaven

UART Universal Asynchronous Receiver Transmitter

UC 6772 Vitralit̂I UC 6772, UV and light-curing adhesives

UHT Ultra High Temperature

USB Universal Serial Bus

UV Ultraviolet Light

v Frequency of Light

μ**TAS** Micro Total Analysis System

Xe Xenon

Chapter 1

Introduction

Immunoassays are bioanalytical methods commonly used to detect and quantify different substances in fluid samples. Immunoassay methods have become an enormous importance because of the selectivity, specificity, effectiveness and ease of using antibodies. Thus, immunoassays techniques have been used in a variety of applications, such as for chemical analysis, medical diagnostics, pharmacy analysis, food safety testing, biology analysis and for further scientific investigations. Immunoassay-based reactions implemented in microfluidic systems (known as μTAS or Lab-on-a-Chip systems) offers additional benefits. Under standard laboratory conditions, immunoassay process including washing, mixing and incubation steps takes several hours up to a couple of days. Longer process times are mostly attributed to an inefficient mass transport from sample to the surface, where the reaction takes place. The implementation of immunoassay within a microfluidic device can considerably optimize this procedure in terms of reduction of reagents, enhancement of reaction efficiency and reduction of assay time. Chemical reactions between the solution phase and the surface are much faster in microfluidic devices than using standard microtiter plates due to the short diffusion distances and high surface to volume ratio. This chapter gives an introduction to microfluidic devices and immunoassay techniques, which were the most important criteria to consider in the design and development of the NANODETECT prototype.

1.1 Microfluidic devices

Nowadays, microfluidic systems are indeed changing and revolutionizing the analytical chemistry and becoming increasingly importance in other applications. The marked increase in the development of microfluidic devices is attributed to the ability for delivering and manipulating minute amount of liquid at high precision in terms of volume, reduced reaction time and enhanced functionality. Moreover, the relative low cost of the fabrication, the handling facility and the

portability make microfluidic devices very attractive for single use in chemical analysis. Another evident advantage is the reduced size of channels; as a result, the amount of reagents required for any analysis is quite small, which is especially significant when the reagents are expensive.

Since the microfabrication techniques appeared, many miniaturized systems have been produced in very small size replacing complex instruments and procedures employed in conventional laboratories [XZZC09, CCLL08, ASI$^+$06, DSM$^+$09b]. Common techniques used to analyze and identify characteristic samples are neither sensitive nor specific. The analysis of samples is commonly performed using microbiological methods and physical or chemical analysis, such as high performance liquid chromatography (HPLC) [TP82, BCP$^+$98, MMS$^+$08]. Usually, these methods require long operation time for analysis and they can only be operated with the presence of sophisticated instruments. Hence, microfluidic technology is gaining wide acceptance for many analytical applications whereas the use of conventional methods is reducing significantly.

In the last years, the use of microfluidic systems has considerably increased in life science, analytical chemistry and biochemistry fields. Commonly, microfluidic systems have been used to analyze human biological fluids samples such as whole blood, urine, saliva, plasma, etc. According to the design and complexity of the microstructures within the microfluidic device, such systems can supply essential functions to identify or quantify specific molecules encountered in the sample. For example, cell separation [YHH$^+$06], sample mixing [TL02], cell manipulation [MML$^+$03], transport and quantity of specific biomolecules [BHH05] are some of many functions that might be successfully carried out by miniaturized fluidic devices. This achievement shows that miniaturization offers the possibility to integrate multiple functions within a single and small microfluidic device, which is also known as Lab-on-a-Chip systems (LOC) [NBW06, PTA$^+$10]. Although microfluidic systems have been directly applicable in research fields, such as biological, medical, chemistry and other biotechnologies sectors, the current thesis demonstrates that the development and fabrication of microfluidic devices may also contribute in the food quality control systems.

1.2 Immunoassay in microfluidic devices

The immunoassay technique has been widely used to selectively recognize a diverse range of protein biomarkers in a variety of applications, such as pharmaceutical analysis, medical diagnostics, food safety testing and also for scientific

investigations. The immunoassay can be classified into heterogeneous and homogeneous formats. In the heterogeneous immunoassays format, antibodies (Ab) or antigens (Ag) are immobilized on a solid support whereas homogeneous assays take place in the solution phase. Heterogeneous immunoassays have the advantage of high surface area volume ratio, which increases the sensitivity. However, additional procedures are required for the immobilization of Ab or Ag on the solid support. Homogeneous assays are very fast and take advantage of the multiplexing but preconcentration procedure is usually required [BHH05].

In the context of this thesis, heterogeneous immunoassay systems were implemented in microfluidic devices to detect specific contamination of raw milk. Specifically, the immunoassay method was implemented into the microfluidic device. Sample and reagents required for performing the immunoassay were sequentially introduced into the microchannels for immobilization, blocking, washing, reaction and detection. Using microfluidic devices, immobilization is the most important step in the assay that influences the sensitivity and specificity. Therefore, the surface of these microfluidic systems should have a good biocompatibility, so that the proteins (Ab or Ag) can be immobilized for further detection. The immunoassay known as enzyme-linked immunosorbent assay (ELISA) is the most commonly used immunoassay format because it is effective, simple and sensitive method to identify a specific protein from a sample [YLGL09]. This immunoassay is also known as sandwich assay because the antibodies and corresponding antigens form a sandwich. Figures 1.1, 1.2 and 1.3 depict the schematic representation of the general principle of the heterogeneous immunoassay ELISA within a microchannel. First, samples containing specific antibodies (Ab) are introduced into the microchannel. Then, bovine serum albumin (BSA) is injected into the channel blocking the non-occupied surface of the sensing area in order to reduce the non-specific binding.
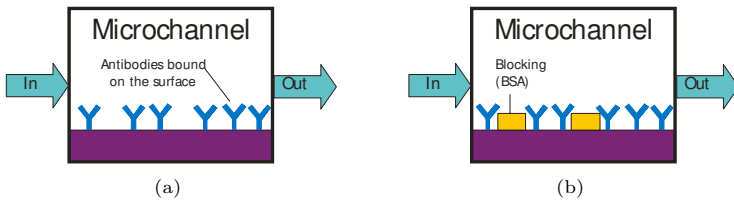
Figure 1.1: Ab and BSA binding into a microchannel (a) Binding of specific catching antibodies on the bottom, ceiling or walls of the microchannels. (b) Inactivation of biocompatible surface by means of BSA to reduce non-specific binding.

Once Ab and BSA are immobilized onto the biocompatible surface of the microchannel, a sample containing specific contamination or antigens (Ag) are introduced as well into the microchannel. As illustrated in figure 1.2, Ag representing the contamination from the sample bind to the already immobilized Ab, while free Ag are then washed off.

(a)   (b)
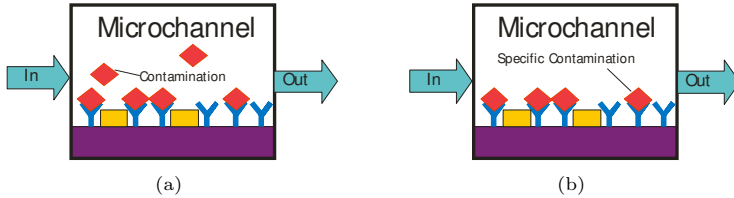
Figure 1.2: Schematic representation of Ag (contamination) binding (a) Sample with contamination of interest or Ag flowing through the channel. These antigens are specifically enriched by the already immobilized antibodies. (b) Non-specific antigens or proteins are then washed off from the surface of the microchannel.

In a separated step, antibodies are then labeled and chemically attached to an enzyme that catalyzes the chemical reaction. These enzyme labeled antibodies are introduced into the microfluidic channel, which are then bound by the corresponding Ag. Unbound labeled antibodies are washed off as shown in figure 1.3 (a). Enzyme labeled Ab generate a signal, such as a color, fluorescent or luminescent (see figure 1.3 (b)), so that it can be then measured by an optical sensor. The resulting signal in this immunoassay represents the concentration of Ag in the fluid sample using the wall, bottom or ceiling of a microchannel as solid support.

(a)   (b)
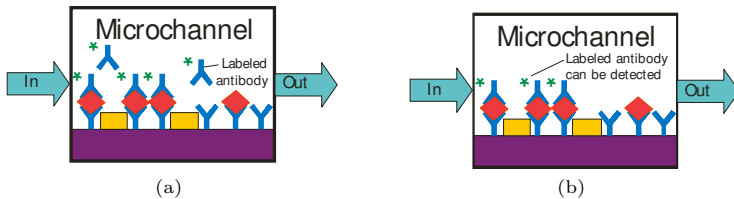
Figure 1.3: Labeled Ab are introduced into the microchannel (a) Labeled Ab bind onto other site of corresponding Ag. (b) Unbound labeled Ab are washed off. Labeled Ab generate an optical signal with an intensity proportional to the enriched amount of Ag [GSK+09].

1.3 Motivation

Milk is one of the most consumed products in the world. Its rich composition of proteins, vitamins, fats, carbohydrates and minerals, such as calcium and phosphorus are the main reason as well as its availability. Although the quality of milk is strictly controlled by the milk industry, there are still cases of illnesses caused by the consumption of milk. The most common cases of contaminated milk involve foodborne pathogens, toxins or antibiotics used to prevent or treat disease of lactating cows [Wat].

In the milk industry, a high hygienic standard is demanded to avoid risk factors for the consumer's safety. The quality of milk can be only guaranteed, if several tests have been performed in different phases of milk transportation, which starts at the farm and finishes at the consumers. Laboratories offer a broad range of testing service for several types of contamination in raw milk. But the main problem of the food market is the lack of user friendly monitoring systems that could detect the presence of microorganisms or specific toxins with high efficiency at short times. For the detection of such compounds, different procedures based mainly on microbiological methods and physical or chemical analysis, such as high performance liquid chromatography (HPLC) are used [MMS+08]. But, these methods are expensive, limited for testing large volumes and limited in multiple detection. Furthermore, these techniques require the assistance of an expert, sophisticated analytical instruments and also expensive reagents making these testing methods less accessible than desired.

To prevent foodborne illness caused by the consumption of contaminated milk, it is important to be able to detect contaminants on-site, but to date a completely integrated system for on-site monitoring of specific substances in milk has not been demonstrated. In order to contribute to the development of accessible and user friendly system to monitor contaminants in the food chain, the current thesis presents the development of an innovative measurement system for testing milk quality. This thesis demonstrates the application of biosensing technology for the development of a measurement system that combines the specificity of immunoassay within microfluidic device technology with the sensitivity of fluorescence-based detection methods. The prototype to be developed in this thesis focuses on a fast on-site recognition of substances in raw milk. This has the advantage of preventing the distribution of contaminated milk before it gets mixed with clean milk from other sources. The prototype further allows simultaneous detection and quantification of multiple and non-desired contaminant particles encountered in raw milk.

1.4 NANODETECT project

The current thesis was realized within the NANODETECT project. This project emerged from the 7th framework program of the European Commission and started in September 2008 with a 36 month duration and six month extension approved by the European Commission. Nine leading European Institutions have joined this ambitious project. NANODETECT was an ambitious project aiming at providing a flexible and user friendly prototype for testing raw milk. The technology used in this prototype might be easily transferred for quality monitoring in fluid-related industrial applications, such as controlling drinking water and fish farming water.

The substances listed below, with exception of the fraud, are examples of pathogenic microorganisms, mycotoxins or residues from an antibiotic therapy. These compounds can contaminate raw milk and cause illness, thus the importance of an early detection. The specific contaminants to be detected within the scope of this project are the following:

- Pathogenic microorganisms (listeria monocytogenes)

- Mycotoxins (aflatoxin M1)

- Drug residues (gentamicin)

- Fraud (high value goat milk mixed with cheaper cows milk)

Listeria monocytogenes is a pathogenic microorganism and can be particularly found in raw milk. This bacterium can cause serious illness for some people; especially newborns, old people, pregnant women and people with weakened immune systems. After ingestion of listeria monocytogenes, symptoms, such as, nausea, vomiting, abdominal cramps, headache and permanent fever occur. Although listeria can be eliminated by means of pasteurization and cooking, contamination might occur after pasteurization, but before the product is packaged. Listeria can also grow and multiply at refrigerator temperatures [OJA05]. In accordance with the Commission Regulation EC 2073/2005 on microbiological criteria for foodstuffs, listeria must be absent in 25g or not exceed 100cfu/g throughout shelf life of the product.

Besides the contamination with microorganisms, raw milk could also contain microbial toxins, as for example aflatoxin. Aflatoxin are mycotoxins, which can be found in several types of foods destined for both human and animal consumption, such as corn, sorghum, rice, cottonseed, peanuts, tree nuts, dried coconut meat, cocoa beans, figs, ginger, and nutmeg. Aflatoxin is carcinogenic

and therefore, they must be closely monitored in the food supply. Aflatoxin B1 (AFB1) presents the highest degree of toxity for animals and is followed by the aflatoxin M1 (AFM1), AFG1, AFB2 and AFG2 [GB95]. When aflatoxin B1 is ingested by lactating animals, aflatoxin M1 can be then found in the milk and processed milk products. The maximum limit of aflatoxin in food allowed varies according to the legislation of each country. In Europe, aflatoxin levels are regulated by the Commission Regulation EC 1881/2006. According to this, the limit of AFM1 in milk is about $0.05 \mu g/kg$ or $0.05 \mu g/L$ [JOI01]. These minimum levels of aflatoxin in foodstuffs should be detected on time, due to the high risk to human health.

Antibiotics and other drugs are used to treat cows with infections. The use of antibiotics may result in drug residues, which are found in products from the animal in different concentration levels. According to the Council Regulation 2377/90, established maximum residue limit for residues in milk is about $100 \mu g/kg$. Normally, the milk of treated cows should be withheld from the bulk tank until their milk is free of drug residues. But treated cows might be occasionally overlooked and thereby, milk contaminated with drugs could enter the bulk tank. Traditional test methods such as microbial inhibitor tests have been used for detection of drugs residues in milk, which involve incubating a susceptible organism in the presence of the milk sample. In the presence of an antibiotic, the organism fails to grow while in the absence of it, the organism grows. Both cases can be then detected visually either by opacity or by color change [MAB+03]. However, these standard methods are cumbersome and time consuming and because the results are not available immediately, they are not suited for checking milk prior to receipt.

The authenticity of the milk should be also detected. Recently, goat milk has become popular, because it is highly nutritious for physically weak people increasing the demand of consumers. The increasing demand for goat milk results in adulteration by cow milk, which can be obtained at lower prices than goat milk [CCC+04]. At the first view, goat milk mixed with cow milk cannot be easily recognized due to the similarity in colors, chemical composition and organoleptic properties. Thus, analytical methods with high sensitivity to verify and quantify fraudulence in goat milk are desirable.

The aim of the NANODETECT project was the design, development and construction of a transportable prototype that provides fast, selective and sensitive identification of specific substances in raw milk. Specific concentration of contaminants in raw milk might be detected by means of immunoassay and microfluidic technologies offering simple, relatively inexpensive and self- admin-

istered bioanalytical tests of raw milk. The NANODETECT project involved partners from EU member states offering different expertise and knowledge bases. The required immunoassay techniques were established and developed by the project partners ttz [1] (Germany), RIKILT [2] (Netherlands) and Biocult [3] (Netherlands). Information technology lied at FERA [4] (England) and NorayBio [5] (Spain). The design and development of the optical detection system were performed by Optotek [6] (Slovenia). Required microfluidic devices were designed and fabricated by IMSAS/MCB [7] (Germany). The design, development and manufacturing of prototype parts and subsequently assembly of the functional NANODETECT prototype were also carried out at IMSAS/MCB. The application and evaluation of the prototype were undertaken by RINY [8] (Spain) and MGLANG [9] (Germany).

1.5 Outline of thesis

Based on immunoassay and microfluidic technologies, the aim of this thesis is to design, develop and construct a prototype for monitoring raw milk quality. This thesis is structured in eight chapters.

1. Chapter 1 introduces the technologies required for the development and implementation of the NANODETECT prototype.

2. Chapter 2 presents a description of the immunoassay principles. This chapter describes also the theoretical background of microfluidics and microfabrication technology. The basic operation of the optical detection system implemented in the NANODETECT prototype is also given.

3. Chapter 3 shows some alternative materials, which can be used to fabricate microfluidic devices. The characteristic properties of these materials are evaluated in this chapter, including the biocompatibility and emitted background fluorescence.

4. The shape and geometry of the microchannel influence the interaction of the biomolecules within the microfluidic devices. Chapter 4 presents

---

[1] Technology-Transfer-Zentrum, Bremerhaven
[2] Institute of Food Safety, Wageningen
[3] Antibody Production Contract House, Leiden
[4] The Food and Environment Research Agency, York
[5] Noray Bioinformatics S.L., Bilbao
[6] OPTOTEK d. o. o., Laser and optical technology, Ljubljana
[7] Microsystems Center Bremen. IMSAS is member of MCB
[8] Formargeria Granjua Rinya S.L., Valencia
[9] Meiereigenossenschaft Langenhorn e.V., Langenhorn

the expected trajectory of the biomolecules based on the flow velocity profile of microchannels with common shape geometries. The design and simulation of different microfluidic structures are also given in this chapter.

5. Chapter 5 focuses on the definition of requirements to produce microfluidic devices involving materials and methods for their fabrication.

6. Chapter 6 shows the characterization of fabricated microfluidic devices using luminescent nano particles. Characteristic dimensions of selected microfluidic devices were adapted in accordance with the final specifications of the optical sensor. The enrichment efficiency within redesigned microfluidic devices was evaluated.

7. Chapter 7 presents the work performed to integrate the NANODETECT prototype. Different concentrations of specific substances were measured using the prototype to verify its functionality.

8. Summary and outlook of this thesis are described in Chapter 8.

Chapter 2

Fundamentals

This chapter reviews the theoretical concepts related to this thesis. Principal immunoassay methods based on fluorescence detection are described. This chapter presents also an overview of milk composition and microfluidics. It is followed by the description of different technologies and materials utilized to fabricate microfluidic systems. Basic concepts in fluorescence formation and detection are also reviewed in this chapter.

2.1 Composition of raw milk

Milk composition depends on the breed, genetics, feed considerations, seasonal, and geographic variations. Basically, milk is composed of water, carbohydrate, fat, protein, minerals and vitamins. Water is the main component of raw milk with 88%, followed by protein, fat, lactose and minerals. Table 2.1 shows an overview of the composition of raw milk from different species.

Table 2.1: Composition of milk from different species (amount per 100g) [Wat].

Nutrient	Cow	Buffalo	Human
Water, g	88.0	84.0	87.5
Protein, g	3.2	3.7	1.0
Fat, g	3.4	6.9	4.4
Lactose, g	4.7	5.2	6.9
Minerals, g	0.72	0.79	0.20

Fat is the most variable component in milk ranging from 3.5 to 6.0%. The concentration varies according to breeds of cattle and feeding practices. Fat in milk is formed from fat globules having a diameter between 0.1μm and 15μm.

These fat particles or globules are covered by a thin membrane, which stabilizes the fat globules in an emulsion within the aqueous environment of the milk, so that the globules do not mix with the water in milk [Wat].

The concentration of protein in milk varies from 3.0 to 4.0%. This variation depends also on the breed of the cow and on the fat amount in milk. The main milk proteins are caseins α - lactalbumin, and β - lactoglobulin being more than 90% of the total protein in cow's milk. Likewise, casein is composed of several proteins that form a multi-molecular granular structure. This structure is called casein micelle being an important part for milk digestion. Casein micelles have a tipical size from 100 to 300nm being so tiny that remain in suspension. Figure 2.1 shows the main structural components of milk. The left view from this figure is a representation of milk magnified at about 500 times and the right view at 50.000 times [Bec11].
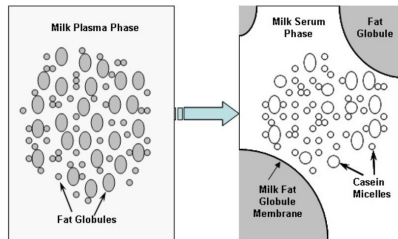
Figure 2.1: Fat globules and casein micelles in milk, taken from [Bec11].

The principal carbohydrate in milk is lactose composed mainly of D-glucose and D-galactose. In comparison to fat in milk, the concentration of lactose cannot be influenced by breeds variations, seasonal variation or geographic variations. Lactose in milk remains relatively constant between 4.8 and 5.2% [Wat]. Lactose and mineral salts are totally dissolved in the water in milk.

Undesirable components are also found in milk. Due to its nutritional composition, raw milk is ideal for microorganisms' growth. Hence, milk should be cooled to about 4°C as soon as possible to maintain its quality. High temperature, acidity or contamination by microorganisms can rapidly decrease its quality.

2.2 Immunoassay principles

The immunoassay was first investigated by Rosalyn Yalow and Solomon Berson in 1960 [YB61] spreading it out not only on clinical research and diagnosis, but

also on pharmaceutical, veterinary, forensic and food science. Immunoassays use the sensitivity of antibody-antigen reaction, which allows the enrichment, quantification and thus monitoring of small molecules, such as pathogens, drugs residues, specific proteins, virus, among others particles, from a fluid sample.

Antibodies (Ab) are very selective and only bind to their specific analytes or antigens (Ag) in despite of the presence of a large volume of other materials in a sample. Each antibody has an unique structure and can be only recognized by the corresponding antigen. Immunoassay is based on the binding reaction between the antibody and antigen and it can be described by the law of mass action [RL01]:

$$[Ag] + [Ab] \longleftrightarrow [Ag - Ab] \tag{2.1}$$
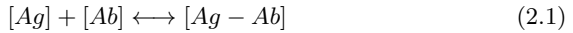
Immunoassays have a variety of formats according to the need of the experiment. Immunoassays can be divided into competitive and non-competitive [LSC01]. In competitive assays, Ab from the sample competes with labeled Ab for binding to immobilized Ag onto the solid support. When increasing the amount of analyte (Ab or Ag) to be detected, the amount of bound labeled analyte analogue decreases [RL01] (see figure (2.2)).

Figure 2.2: Representation of competitive immunoassay, where Ab: antibody, Ag: antigen, Ag*: labeled antigen, Ab*: labeled antibody [RL01].

Unlabeled Ag blocks the ability of labeled Ag to bind because binding site on the Ab is already occupied, and thus, generated signal decreases when the amount of analyte increases. The amount of Ag in the test sample is inversely related to the amount of label measured in the competitive format.

The non-competitive assay is referred to a sandwich immunoassay because the analyte is bound between two highly specific antibody reagents (see figure 2.3). The signal increases in proportion to the analyte concentration in contrast with the indirect proportionality of competitive immunoassay.
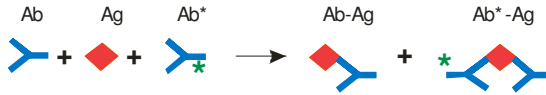
Figure 2.3: Representation of non-competitive immunoassay where Ab: antibody, Ag: antigen, Ag*: labeled antigen, Ab*: labeled antibody [RL01].

2.2.1 Biological detection system in the NANODETECT prototype

The biological detection in the NANODETECT prototype is based on heterogeneous immunoassays including competitive and non-competitive assay. These immunoassays use monoclonal antibodies (MAb) and labeled proteins phycoerythrin (PE) or Alexa with an excitation peak of 532nm and an emission peak of 575nm. In the case of listeria and fraud assays, antibodies were coated on selected surfaces whereas in aflatoxin M1 and drug assays protein conjugates were prepared prior to coating step. The biological system for the enrichment and detection of these contamination models in raw milk is described in the following paragraphs.

Listeria monocytogenes and fraud detection unit

The detection unit of listeria monocytogenes and fraud is based on the sandwich immunoassay as represented in figure 2.4. First, catching antibodies were immobilized on the surface of the microchannel, which is followed by coating of BSA. As explained in section 1.2, BSA reduces the non-unspecific binding on the surface, and thus increasing the specificity of the immunoassay. After that, antigens flow through the channel and have contact with corresponding antibodies (immobilized catching antibodies). Because the antigens did not have any fluorescent compound, a second labeled antibody was utilized for the detection. For this purpose, specific antibodies were labeled with phycoerythrin (PE) being a fluorescent protein with excitation at 532nm and emission light at 575nm. The detecting antibody bound to corresponding antigen, and then PE could be detected. Because some labeled antibodies could not bind to the antigens, a washing step was required before the detection takes place.
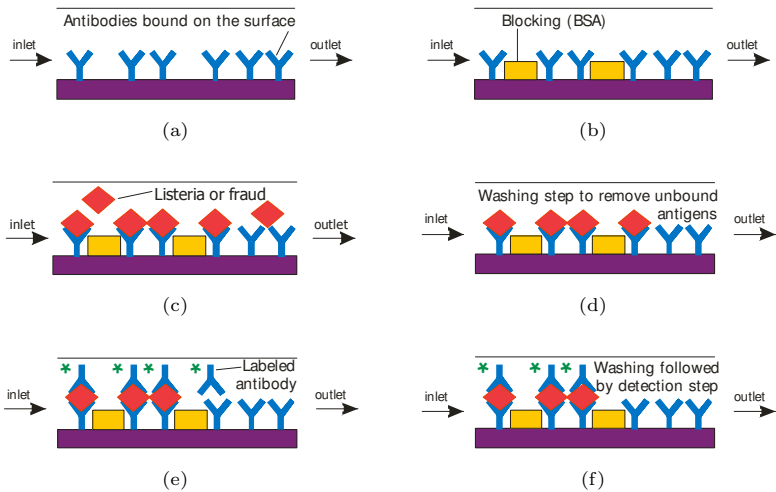
Figure 2.4: Coating steps for the bioactivation of the surface and detection procedure of listeria or fraud in raw milk (a) Coating of catching antibodies on the surface. (b) Free surface is inactivated by BSA. (c) Milk flows through the microchannel. Specific particles bind to the catching antibodies and thereby are enriched. (d) Unbound antigens are washed off. (e) PE labeled antibodies are introduced into the channel and bind to respective antigens. (f) Unbound labeled Ab are washed off. The detection can be performed by exciting PE.

Aflatoxin M1 and drug residues detection unit

The detection unit of aflatoxin M1 and drug samples cannot be performed in the same procedure as listeria and fraud assays. Aflatoxin M1 and drug antigens have significantly low molecular weight, and thereby it is impossible that a second antibody can bind to corresponding antigens. In this case, the detection unit is based on the competition assay, in which the signal is inversely proportional to the amount of antigen in the sample. Initially, antigens (aflatoxin M1 or drug residues) conjugated with BSA were coated on the surface of the microchannel. This step was followed by BSA coating to prevent unspecific binding increasing the sensitivity and detection specificity. Milk containing aflatoxin M1 or drug residues and corresponding antibodies were mixed in a vessel prior to be introduced into the microfluidic device. The difference between both assays lied on the detection procedure. Aflatoxin M1 used only one serie of labeled antibodies as catching and detecting antibodies

while drug assay required two different series of antibodies: one as catching and the second as detecting antibodies. In both assays, labeled antibodies bound competitively to free antigens (aflatoxin M1 assay) or primary antibodies (drug assay), and after the antibody-antigen binding, unbound or unspecified substances were washed away. Antibodies were also labeled with phycoerythrin (PE) that can be excited at 532nm emitting light at 575nm. The procedures are given in figure 2.5 and 2.6.
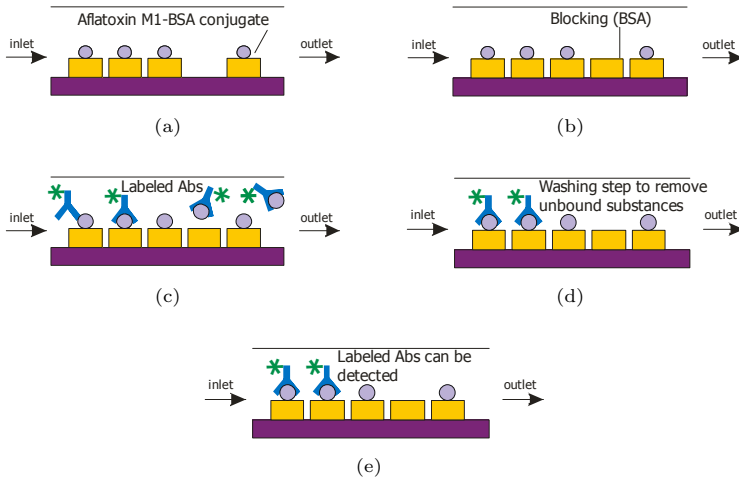
Figure 2.5: Coating steps for the bioactivation of the surface and detection procedure of aflatoxin M1 in raw milk. This procedure is based on a direct competitive assay format. (a) Coating of BSA-Aflatoxin M1 conjugated on the surface. (b) Free surface is inactivated by BSA to avoid unspecific binding. (c) Milk containing specific contamination and corresponding labeled antibodies flow through the microchannel. (d) Free labeled antibodies bind to coated antigens in absence of antigens in the milk sample. Unbound proteins are washed off. (e) Detection can be performed by exciting labeled antibodies.
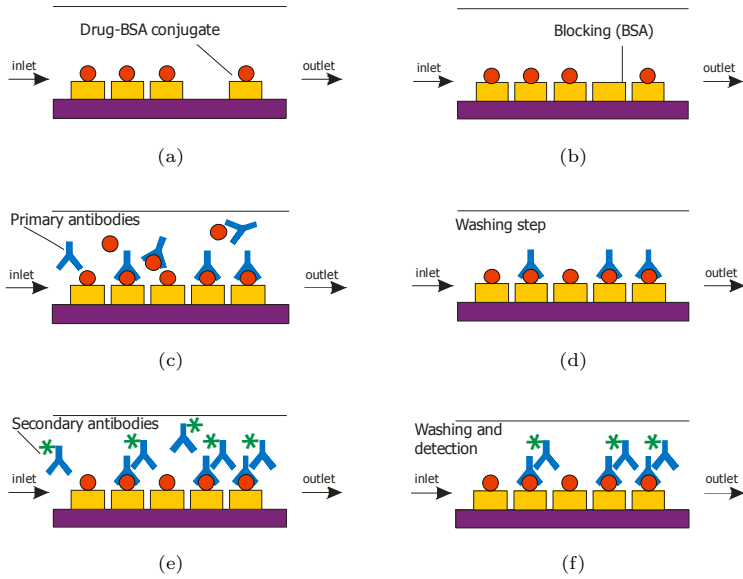
Figure 2.6: Coating steps for the bioactivation of the surface and detection procedure of drug residues in raw milk. This procedure is based on a indirect competitive assay format. (a) Coating of BSA conjugated with respective antigen on the surface. (b) Free surface is inactivated by BSA. (c) Milk containing specific contamination and corresponding antibodies (primary) flow through the microchannel. (d) Free antibodies bind to coated antigens in absence of antigens in the milk sample. Unbound proteins are washed off. (e) Secondary antibodies, i.e. labeled antibodies bind competitively to the primary antibodies. Unbound substances are removed. (f) Detection can be performed by exciting labeled antibodies.

2.3 Fluid flow in microfluidic devices

Microfluidics deals with the theory of fluid including their behavior, precise control and manipulation in micro scale. The use of microfluidic devices has gained significant attention in recent years due to several advantages of miniaturization. These advantages include short analysis time, low cost, portability, reduced volume of sample and reagent and high sensitivity for biosensing. At small scales, a wide variety of physical properties must be considered. These physical properties include the surface tension, diffusion, laminar flow, fluidic

resistance and surface area to volume ratio. The relation of these effects can be expressed by dimensionless numbers, such as the Reynolds number R_e relating inertial forces to viscous forces; the Péclet number P_e, which relates convection to diffusion [eH99]. A review of fluid flow within microfluidic devices is given in the following subsections.

2.3.1 Laminar flow

Laminar flow can be interpreted as a set of layers flowing along each other in the fluid direction. Thus, two or more streams flowing in contact with each other cannot be mixed but molecules can migrate by diffusion. In recent approaches, diffusion between laminar streams has been used in microfluidic devices for sorting particles by size and performing assays [BY97, HKH+01].

2.3.2 The Reynolds number

The Reynolds number (R_e) of a fluid describes its flow regime (laminar or turbulent). In turbulent regime of flow, there is irregular random motion of fluid particles, and unsteady vortices appear and interact with each other. Instead of that, laminar flow refers to the flow in which the streamlines are locally in parallel. The Reynolds number characterizes the relative importance of inertial and viscous force, and it can be determined by the following equation [Kue07]:

$$R_e = \frac{\rho U L}{\mu} = \frac{U L}{\nu} \tag{2.2}$$

where U is the velocity of the fluid, L is the characteristic channel dimension, ρ is the fluid density, μ the dynamic viscosity and ν the kinematic viscosity of the fluid. For example, in a pipe, the flow U is the average axial velocity, and L is the hydraulic diameter of the pipe. The transition between laminar and turbulent flow takes place when $R_e \approx 2000$. In microchannels, the Reynolds number remains generally small due to the small dimension and low flow rates.

2.3.3 The Péclet number

The Péclet number (Pe) is a dimensionless parameter that indicates the direction in which the diffusion occurs. This parameter is the ratio between mass transport due to advection and diffusion as follows [BS10]:

$$Pe = \frac{UL}{D} \tag{2.3}$$

where U is the velocity, L is the characteristic length of the microchannel width and D the diffusion coefficient. Figure 2.7 shows the schematic representation of the particle behavior characterized by the Péclet number.
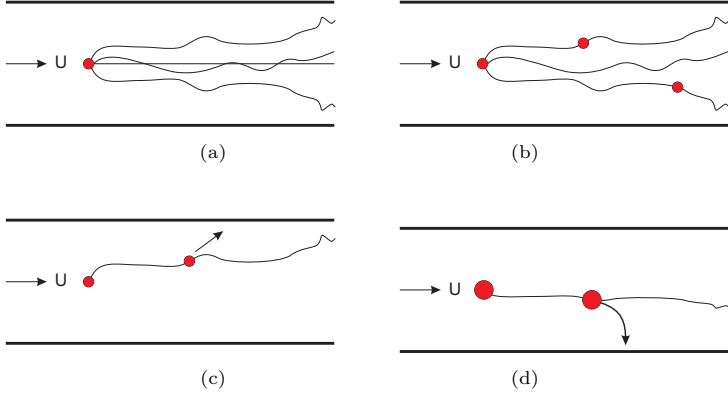
Figure 2.7: Possible transport of biochemical species in microfluidic channels. (a) When $Pe \ll 1$, diffusion plays an important role. (b) Biomolecules follow flow streamlines. (c) When $Pe \gg 1$, inertial effects force biomolecules to deviate the flow streamline. (d) Large and heavy biomolecules tend to sediment despite to the molecule interaction [BS10].

2.3.4 The Dean number

When a fluid flows in a curved channel, a secondary flow is created because of the centrifugal force developed from the channel curvature. This secondary flow is also known as Dean Flow, and it is characterized by the Dean number (De) that expresses the relation of inertial and centrifugal forces to viscous forces [BS10, SU06]:

$$De = \frac{UR}{\nu}\sqrt{\frac{R}{R_c}} = Re\sqrt{\frac{R}{R_c}} \tag{2.4}$$

where U is the average velocity, ν the kinematic viscosity, R the dimension of the channel and R_c the curvature radius of the channel. A microflow traveling in

a curved channel might produce recirculation or spiral streamlines in the curved regions, and thus may provide several advantages regarding the enrichment and mixing effect.

2.3.5 Diffusion

Diffusion describes a process in which molecules in fluids or gases caused by Brownian motion, spread out or diffuse over time, so that the average concentration of particles throughout the volume is constant. The relation between diffusion distance and migration time is given by Equation 2.5 [BS10]:

$$\tau = \frac{R^2}{4D} \tag{2.5}$$

where D is the diffusion coefficient of the particle and R is the distance that particles move in a time τ. The diffusion coefficient is given by the Einstein law as follows:

$$D = \frac{k_B T}{6\pi R_H \mu} \tag{2.6}$$

where k_B (1.38^{-23} J/K) is the Boltzmann constant that relates kinetic energy of a molecule to temperature, T the temperature in K, μ the dynamic viscosity of the fluid and R_H the hydraulic radius of the particle [BS10]. As shown in Equation 2.6, when molecular radius increases, D decreases due to the enhanced friction interactions. Typically, the diffusion coefficients of molecules in liquids are between 10^{-9} and 10^{-11} m^2/ sec [BS10].

2.3.6 Flow profile

Microchannels with a rectangular cross section and circular pipes are commonly used in microfluidic applications. Since the flow is laminar in the current thesis, the Navier-Stokes equations can be reduced and applied in each case to determine the flow profile.

Hagen-Poiseuille flow

In a Poiseuille flow, the fluid is driven through a microchannel by applying a pressure difference. Originally, Poiseuille analyzed the behavior of the fluid

within a circular cross section channel. However, in microfluidic, other channels shapes are frequently used. In the case of a circular pipe with a radius R, the velocity in the axial x-direction yields Equation 2.7 [Sta79, Kue07].

$$u(x) = -\frac{1}{4\mu}\frac{\partial p}{\partial x}\left(R^2 - r^2\right) \qquad (2.7)$$

where R is the radius of the pipe and μ the dynamic viscosity. Since p falls in the direction of flow, $\dfrac{\partial p}{\partial x}$ is negative. According to the equation above, the flow has the usual parabolic, and the maximum velocity takes place at the middle of the pipe where $r = 0$ (see figure 2.8).
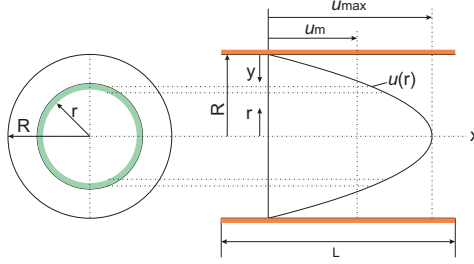
Figure 2.8: Velocity distribution for laminar flow through a circular pipe. u_{max} and u_m represent the maximal and average velocity along the pipe respectively.

Written in terms of pressure drop (ΔP),

$$\Delta P = \frac{8\mu U L}{R^2} \qquad (2.8)$$

where U is the average velocity and L the characteristic length of the channel. Since the velocity mean value is given by $U = \dfrac{Q}{Area}$, Equation 2.8 can be expressed in terms of the volumetric flow rate (Q) and diameter (d) as follows:

$$Q = \frac{\pi d^4}{128\mu L}\Delta P \qquad (2.9)$$

which is known as Hagen-Poiseuille's equation for laminar flow in a pipe. This equation can be also applied to rectangular channels by using the hydraulic diameter (d_h) as equivalent pipe diameter (d): $d_h = \dfrac{2WH}{W + H}$ where W is the width and H the height of the channel.

Flow between parallel plates

Another case of laminar flow is the fluid forced to flow between parallel plates keeping a distance h. Using a rectangular channel as shown in figure 2.9, where $l > w > h$, it can be assumed that the flow is two-dimensional. This means that $v_z = 0$ while v_x and v_y are functions of x, y and z. This assumption is related to the Hele-Shaw flow [UCZ$^+$93]. If the Reynolds number is small, the viscous forces dominate, and accordingly the inertial effects are neglible. These structures are commonly used in microfluidic system for biological applications because the biomolecules are forced to have close contact to the wall and thereby bind to immobilized antibodies on the surface of the microchannel. The flow in a narrow gap, between two parallel surfaces, is also known as Hele-Shaw flow [BS10]. This channel is shown in figure 2.9.
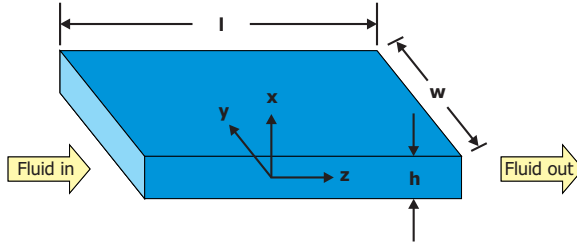
Figure 2.9: Rectangular microchannel

Since the Reynolds number is small and the ratio between the height and length of the microchannel is less than 1, the equation of motion can be simplified as follows [Kra05]:

$$0 = -\frac{\partial p}{\partial x} \tag{2.10}$$

$$0 = -\frac{\partial p}{\partial x} + \mu \frac{\partial^2 w_y}{\partial x^2} \tag{2.11}$$

$$0 = -\frac{\partial p}{\partial y} + \mu \frac{\partial^2 w_z}{\partial x^2} + pg \tag{2.12}$$

The first equation shows that pressure does not depend on x. The velocity field can be obtained from the other two equations by integrating them in the x direction [Kra05, Sta79].

$$u_y = -\frac{1}{2\mu}\frac{\partial p}{\partial y}\left(x^2 - \frac{h^2}{4}\right) \tag{2.13}$$

$$u_z = -\frac{1}{2\mu}\left(\frac{\partial p}{\partial z} - pg\right)\left(x^2 - \frac{h^2}{4}\right) \tag{2.14}$$

In accordance with the solution of the reduced Navier-Stokes equations, the velocity can be expressed as follows [Sta79]:

$$u(y) = -\frac{1}{2\mu}\frac{\partial p}{\partial x}\left(hy - y^2\right) \tag{2.15}$$

The velocity profile is in the form of a parabola as depicted in figure 2.10.
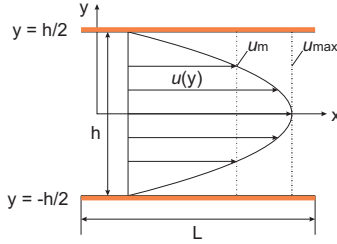
Figure 2.10: Velocity distribution for laminar between parallel plates. u_{max} and u_m represent the maximal and average velocity between the plates respectively.

The minus sign indicates that pressure (p) decreases in the direction of the flow. In terms of pressure drop, Equation 2.15 can be written as:

$$\Delta P = \frac{12\mu U L}{h^2} \tag{2.16}$$

and in terms of volumetric flow rate as:

$$Q = \frac{bh^3}{12\mu L}\Delta P \tag{2.17}$$

where U is the average velocity, L the characteristic length of the channel and the breadth d is the region in which the velocity U may be somewhat different from the velocity in the center. Assuming a large b, and effects associated with it may be negligible, the velocity U may be taken as the average velocity across the breadth [Sta79].

2.3.7 Trajectory of biomolecules within a microchannel

Biomolecule-surface interaction within a microchannel is an essential requirement in the biosensor immunoassays. An efficient interaction increases the binding capacity and accordingly, the signal intensity emitted by labeled biomolecules enhances. An analytical study can be used to determine the possible trajectory. This study consists in a simple approximation by comparing an axial convection to radial diffusion [BS10]. Particles follow the shortest trajectories to have contact to the wall, ceiling or bottom of the channel. On the other hand, particles that are in the middle of the microchannel follow the longest trajectories before having contact to the wall, ceiling or bottom of the channel [BYGA96, BS10]. The trajectory of particles within a microchannel is depicted in figure 2.11.
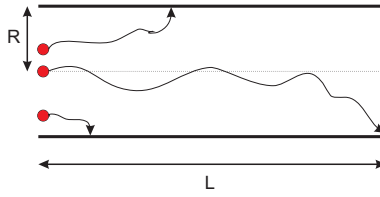
Figure 2.11: Trajectory of biomolecules within a microchannel according to their starting point [BS10].

The average time required for a particle to diffuse across the distance R to the wall can be expressed as follows [BS10]:

$$\tau = \frac{R^2}{4D} \tag{2.18}$$

where R is the radius of the channel, D the diffusion coefficient. From figure 2.11, L is the distance from the starting point from that the particle has traveled in the microchannel. L can be expressed as follows:

$$L \approx 2U\tau = \frac{UR^2}{2D} \tag{2.19}$$

The coefficient 2 in Equation 2.19 indicates that the maximum Hagen-Poiseuille velocity is $2U$ at the middle of the channel. In accordance with the previous analysis, after a distance L, all particles are going to have contact to the wall, ceiling or bottom of the inside of the microchannel. Equation 2.19 can also be expressed as a function of the Péclet number (Pe) and flow rate (Q) [BS10].

$$\frac{L}{R} \approx \frac{UR}{2D} = \frac{1}{2}Pe \tag{2.20}$$

$$L \approx \frac{Q}{2\pi D} \tag{2.21}$$

2.4 Fabrication methods

Microfabrication and micromachining are technologies and processes used to produce structures with dimensions ranging from millimeters to submicrometers. These technologies are based on thin and thick film fabrication techniques commonly used in the electronics industry. Small machines known as micro electro mechanical systems (MEMS) can be found in many devices, which are including computers, mobile phones, car airbag sensors, etc. Advanced sensing technologies are also expanding into new applications in personal healthcare and environmental monitoring. Recent applications of such microdevices include food and water monitoring, drug delivery systems, personal drug administration, blood monitoring [RMT+05, CCLL08] cell sorting [YHH+06], among others.

Microfabrication techniques vary depending on the device being built. The basic technique for producing based MEMS devices are deposition of material layers, patterning and then etching to generate desired structures. Conventional MEMS fabrications technologies include bulk etching, photolithography, surface modification, thin film etching, electrodeposition, plasma etching, bonding, etc. [Fra04, Hil06]. The main techniques to fabricate microstructures for the use in microfluidic devices are described in next subsections.

2.4.1 Substrate material

The first concern of the manufacturing of Lab-on-a-Chip is the material. The material selection varies and depends on the application. Glass, silicon and polymer are materials typically used to fabricate these systems. Due to the well developed technology and the experience in the development and manufacture of microsystems using silicon [Fra04], a considerable amount of microfluidic systems have been fabricated on the basis of this material. However, the use of silicon might be limited because of its high price and because it is not optically transparent in the wavelength range that is typically used for optical detection.

For this reason, fluidic systems based on silicon are usually fabricated in combination with glass material [BHH05]. In this case, microchannels made on silicon have been sealed by a glass cover using an anodic bonding technique at a high temperature. Thus, the optical detection system can be implemented through the glass substrate to examine the flow and the components or reagents within the microchannels. However, microfluidic devices can be also made completely of glass. Material properties, like transparency, chemical and thermal stability of glass make it a very attractive material for use in fluidic devices [FVSD01]; however, the fragility and costs restricts its use.

As mentioned earlier, polymers have been also used to fabricate microfluidic devices, and nowadays, it is even the most widely used material for many applications [BL02, SK06]. Although glass and silicon materials were frequently employed to produce microfluidic systems since their introduction in the early 1990s, the interest to fabricate polymer based microfluidic systems has been increased especially for commercial manufactures. This tendency is primarily driven by the fact that the fabrication technology requires simple manufacturing procedures at greatly reduced cost. Additional advantages with the use of polymer are its transparency, versatility, good isolating properties and mechanical resistance. Therefore, polymer is a material suggested for a wide range of microfluidic products platforms.

2.4.2 Thin film deposition

Film deposition is used in MEMS devices as passivation, stabilizing, dielectric and metallization. The selection of suitable deposition technique depends on the design of the microdevice, function of deposited film and compatibility with further fabrication techniques. Main deposition techniques include thermal oxidation, chemical vapor deposition (CVD) and physical vapor deposition (PVD) [Hil06].

Thermal oxidation

Thermal oxidation is one of the main techniques used in MEMS technology to generate SiO_2 on a silicon surface that could have functions as capacitor dielectric and insolation material. Oxide films are also used as a masking material and as a cleaning method to obtain perfect silicon surface. Thermal oxidation consists of exposing the silicon substrate to an oxidizing environment of O_2 or H_2O at elevated temperature between $600°$C and $1200°$C. Silicon

oxidizes producing oxide films of nanometer thickness in a couple or hours or days. Depending on which oxidant is used, thermal oxidation can be defined as dry (O_2) and wet (H_2O) oxidation. Such reactions are governed by following equations [Mad02]:

$$Si + 2H_2O \rightarrow SiO_2 + H_2 0 \quad (wet\ oxidation) \tag{2.22}$$

$$Si + O_2 \rightarrow SiO_2 \quad (dry\ oxidation) \tag{2.23}$$
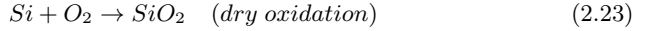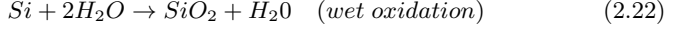
In case of the wet oxidation, water molecules can dissociate at high temperature to form hydroxide OH that can diffuse in the silicon faster than molecular O_2. Hence, the wet oxidation process has a higher oxidation rate than dry oxidation. For example, dry oxidation at a temperature of $900°C$ produces in 1h layers of approximately 20nm thick oxid while wet oxidation generates in 1h approximately 170nm [Fra04]. Because of the higher growth rate, wet oxidation is the preferred method. However, the quality of resulting layers is not as high as in dry oxidation.

Physical Vapor Deposition (PVD)

PVD is a technique, in which thin metals films are deposited on the substrate. Evaporation and sputtering are the most important technologies used in PVD [Hil06]. The choice of deposition method depends fundamentally on the properties of the material to be used. In evaporation, the substrate is placed inside a vacuum chamber in which desired material to be coated on the substrate is also located. The metallic material in block form is then heated until it evaporates. Due to the vacuum, all molecules move freely in the chamber and thus they condense on all surfaces. This technique is simple and works great for metal films with low melting points.

In sputtering technology, the substrate is placed in a vacuum chamber with the material to be deposited (target). The target is located at a high negative potential and at much lower temperatures than evaporation. An inert gas, such as argon (Ar) or xenon (Xe), is introduced at low pressure to the chamber. Gas plasma is formed by direct current (DC) or radio frequency (RF) power source, which causes the gas to become ionized. Then, the target is bombarded with positive argon ions, and the target atoms are ejected, which are deposited on the substrate placed on the anode. Sputtering is preferred over evaporation due to a wide choice of materials to work with, better step coverage and better adhesion on the substrate [Mad02].

Chemical Vapor Deposition (CVD)

CVD is a chemical process used to deposit a solid material from a gaseous state onto a substrate. In this process, the substrate is placed inside a reactor at high temperatures (higher than $300°C$) into which the reactant gases are also introduced. The constituents of a vapor phase discompose and react with the substrate to form the film. CVD is used to produce amorphous and polycrystalline thin films, such as polycrystalline silicon, silicon dioxide and silicon nitride. During CVD, the reactant ions forming a solid material might not only take place on the substrate, but also in the reactor's atmosphere. Reactions on the substrate are known as heterogeneous reactions creating films with good quality. Instead of that, reactions in the gas phase are known as homogenous reactions creating thin films with poor adhesion, low density and high defect films. Thus, heterogeneous reactions are preferred during chemical vapor deposition [Mad02].

2.4.3 Photolithography

Photolithography is a technique used to transfer copies of a master pattern on the photoresist when it is exposed to UV light through a mask. The mask used for the selective exposition is a transparent quartz frame with chrome regions representing the geometry of the microstructures that are transferred to the photoresist. There are two types of photoresist: negative and positive. Chemical properties of these photoresists change when are exposed to UV light. For a positive resist, UV exposure changes the chemical structure, so that it becomes soluble in the developer. Hence, the exposed resist could be removed by the developer solution. In the case of negative resist, it becomes polymerized and the developer solution removes only unexposed areas [Mad02].

2.4.4 Etching

Etching is used in microfabrication to remove material from selected regions of the substrate. This process requires a precise control regarding etch parameters, such time and etch rate to obtain desired cavities in the wafer, which is partially covered with resist. Etching can be either isotropic or anisotropic. Isotropic etching refers to a process in which the etch rate of the material is uniform in all directions (both vertically and laterally), meanwhile anisotropic etching refers to a process in which reactions proceeds perpendicularly (only one direction) to the substrate material at different etch rates [Men07].

The etching process can be classified into two main processes: wet etching and dry etching. In the wet etching process, the substrate is immersed in a chemical solution that dissolves specific regions of the substrate. The main advantages of wet chemical etching process are its high selectivity and etching rate. The wet etching process is in general isotropic etching, except for etching crystal materials, such as silicon that exhibits anisotropic etching. Consequently, since wet etching is isotropic etching, in which etching proceeds in a lateral direction as well, a pattern size smaller than film thickness could not be achieved by wet etching. Thus, this process is usually used whenever a layer has to be removed completely as in the case of so called sacrificial layers [Mad02].

In dry etching, plasma is used instead of chemical solutions. In this process, the substrate is placed inside a reactor in which specific gases are introduced. A radio frequency voltage is applied exciting the gas and thereby producing ions in the reactor. The ions are accelerated towards the substrate, which causes that particles are released from the substrate. The most common process of dry etching is reactive ion etching (RIE), in which anisotropic and isotropic profiles can be obtained. An extension of the RIE process is deep RIE (Deep Reactive Ion Etching) [Hil06]. DRIE is an essential processing step, with which etch depths of hundreds of micros can be achieved enabling the fabrication of deep, trenches and holes in silicon substrate with almost vertical sidewalls.

2.4.5 Plastic replication

Microfluidic devices for biological applications were initially fabricated from silicon and glass. Photolithography and etching techniques have been used to efficiently structure these materials to produce microfluidic systems. However, polymer and plastic materials have gained more attention since they are available at low cost, offer suited material properties and they can be micromachined and replicated quickly [BL02]. A variety of fabrication methods have been developed to produce disposable Lab-on-a-Chip (LOC). The most representative plastic microfabrication technologies include injection molding and hot embossing, which involve the use of a precision mold or master, from which identical polymer microstructures can be fabricated.

Injection molding is one of the most widely used polymeric fabrication process and the first application for microfluidic components was published in 1997 [MNAA+97]. In this method, a metal mold is required that offers more stability than masters made of silicon. Nickel is typically used as metal mold, which could be fabricated using silicon masters. Nickel electroform is then used to

define the pattern in the polymer. Silicon masters are generally fabricated by means of wet etching or DRIE procedures in order to provide structures with high aspect ratio as mentioned previously. Basically, in the injection molding process, selected polymer material is introduced into a heated barred and pushed into the mold cavity under a high pressure. The polymer cools down and solidifies according to the mold cavity, and then injection molded plastic components are ejected from the master.

Hot embossing is the stamping of a pattern into a softened polymer. In this method, mold masters are also required, in which desired structures are defined. Such stamps could be fabricated on glass, silicon or polymer substrate by using standard photolithography or etching processes as described in last subsections. Alternatively, fabricated silicon structures may be used to produce a metallic stamp. Nickel is typically used for this purpose as well as in injection molding process. A hard plastic material is heated just close to the softening temperature, placed on top of the mold and then pressed at lower pressures. Plastic structures could be removed from the mold when the plastic starts to solidify again [BL02].

2.5 Fluorescence

Fluorescence-based detection using fluorescently-labeled biomolecules was implemented in the NANODETECT prototype to identify the low concentration of specific compounds encountered in raw milk. The emitted fluorescence that represents the antibody-antigen concentration within the microfluidic device has been optically detected. This optical detection offers advantages, such as sensitivity, rapid detection, simple excitation and detection.

The fluorescence phenomenon is a property of some chemical substances, where atoms and molecules absorb light at a wavelength and subsequently, emit light almost always of a long wavelength. Before absorption takes place, the molecule is in the ground state. When the molecule absorbs a photon, the energy of the photon is taken up by an electron that raises to a higher energy and vibrational excited state. Thus, the electronic configuration of the molecule is altered. When the atom absorbs a photon with appropriate energy, an electron transits from a lower energy level to a higher one. Conversely, an electron transits from a higher energy level to a lower one, when a photon is emitted. Absorption and emission process can be defined with the following expressions [Ros92]:

$$E_1 + hv = E_2 \quad (absorption) \tag{2.24}$$

$$E_2 = E_1 + hv \quad (emission) \tag{2.25}$$

where E is the energy, hv represents the photon energy, h is the Plank constant and v is the frequency of light. Under normal conditions, the additional energy gained from the photon absorption has to be removed, thus ensuring that the molecule returns to the ground state again. In this process, the additional energy may be converted to heat; alternatively, this energy may be released as a quantum of radiation known as fluorescence (see figure 2.12).

Precisely, fluorescence is the process, in which a molecule with an excited singlet state returns to the ground state emitting additional energy as a photon. The component of the molecule responsible for the fluorescence is called fluorophore, which generates a fluorescent emission in the visible light spectrum.
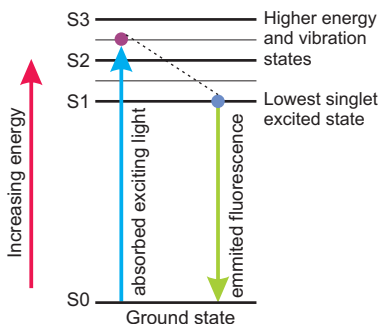
Figure 2.12: Schematic representation of an energy diagram showing how fluorescence is produced. The small colored circles represent the energy stated of the fluorophore. The lifetime of an excited singlet state being the decay time of fluorescence is approximately 1 to 10 n sec [Ros92]. This illustration is a simplified Jablonski energy diagram.

As mentioned before, the wavelength of the emission is normally longer than of the excitation. The reason of that is because the emitted photon has less energy than the excitation. Nevertheless, when the molecule is already in a higher energy level before absorption takes place, the energy of the emission is higher than of the excitation [Ros92].

2.6 Optical techniques

In this thesis, the transmission and reflection measurements were evaluated considering the low fluorescence intensity of dye-labeled molecules. In the case that microfluidic devices are fabricated using transmissive materials, such as glass or plexiglas, measurements in transmission as well as in reflection can theoretically be performed. Although the transmission measurement presents the simple solution, it is not sensitive enough. The transmission measurement is strongly influenced by light scattering being not suitable for the detection of low fluorescence signals. Despite of the use of appropriate filters in this optical configuration, laser light might leak through producing high background signal. This background signal reduces the signal-to-noise ratio and consequently sensitivity.

Conversely, the reflection measurement offers the advantage that the microfluidic devices do not have to transmit light, additional optical filters are not necessary and requirements for the emission filter are not stringent as in the case of the transmission measurement. Another important advantage over transmission measurement is the reduction of background noise in the reflection measurement enhancing the sensitivity. Hence, optical equipment based on the laser light reflection principle was selected to be implemented in the functional prototype of this thesis [opt10, GVS10].

2.7 Main components for optical sensing

A photomultiplier tube (PMT) has been selected as the detector unit for the optical system. This device is one of the detectors most frequently used in laboratory experiments and optical instrumentation because of its response speed and high sensitivity (low-light-level detection) [LC06, PC01]. In this optical configuration, an additional photodiode has been used in order to measure the intensity of the light reflected back from the microfluidic device and thus, monitor laser fluctuations in real time [Vre11]. Consequently, PMT and photodiode signals were essential values to determine the concentration of undesired compounds carried by raw milk.

2.7.1 Photodiode

Photodiodes are semiconductors photodetectors, which convert the incident light into current or voltage. These photodetectors are sensitive, but they

are not suitable for single photon read out [SA09]. A photodiode generates a current or voltage, when the p-n junction is illuminated by light. If a photon has greater energy than the gap energy ($E_{photon} \geq E_{gap}$), the electrons are excited from the valence band into the conduction band leaving holes in the valence band. This mechanism is called photoelectric effect and it is represented in figure 2.13.
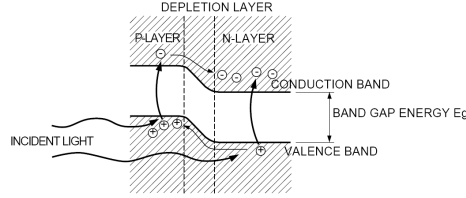
Figure 2.13: Schematic representation of a photodiode with p-n junction state. Figure from [HAM]

Figure 2.14 illustrates a photodiode, in which N material is the substrate and P-layer is the active surface. Both materials form a p-n junction that acts as photoelectric converter. The frequency and spectral response are established according to the thickness of the P-layer, substrate N-layer, bottom N^+-layer and also the doping concentration [HAM].
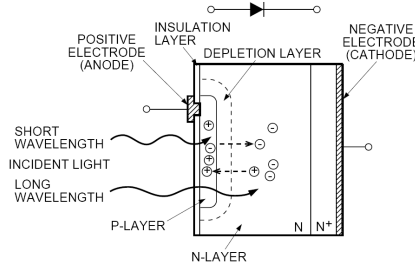
Figure 2.14: Cross section of a photodiode. Figure from [HAM].

2.7.2 Photomultiplier tube (PMT)

Photomultipliers are extremely sensitive detectors of light based on two physical principles such as photoelectric effect and secondary emissions. A PMT consists of a window, a photoemissive cathode (photocathode), focusing electrodes, an electron multiplier (dynode) and an electron collector (anode), which is

usually sealed into an evacuated glass tube. A schematic diagram of a typical photomultiplier tube is given in figure 2.15 [HAM07].
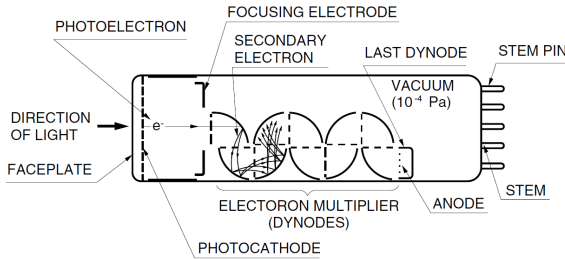
Figure 2.15: Schematic representation of a photomultiplier tube. Figure from [HAM07].

When light enters in a photomultiplier, electrons are excited in the photocathode, thus emitting photoelectrons into the vacuum. These photoelectrons are accelerated and directed by the focusing electrode onto the first dynode, where electrons are multiplied by means of a secondary emission process. Afterwards, multiplied electrons are collected by the anode being the output signal. The photoelectron emission process into a reflection mode is usually formed on a metal plate. In this case, photoelectrons are emitted in the opposite direction of the incident light as represented in figure 2.16.
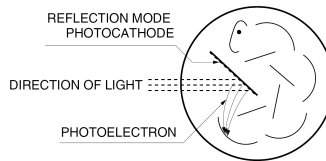
Figure 2.16: Direction of the photoelectrons within a PMT having a reflection mode photocatode. Figure from [HAM07].

The photomultiplier tube is the most sensitive detector for a large number of applications. This is due by the fact that the secondary emission offers a signal amplification ranging from 10^3 up to 10^8. Furthermore, photomultiplier tubes provide extremely high sensitivity and low noise compared to other photosensitive devices [PC01].

Photoelectron emission

Photoelectron emission is a process, in which electrons can be emitted from solids under radiation with photons of low wavelength. Since the energy of the photon is larger than the energy separation, between the top of the valence band and the vacuum level, a photon of energy is absorbed by the solid and then, electrons are emitted into the vacuum as photoelectrons. This process is expressed in the following equation [HAM07]:

$$\eta(v) = (1 - R) \cdot \frac{Pv}{k} \cdot \frac{1}{1 + \frac{1}{kL}} \cdot Ps \tag{2.26}$$

where $\eta(v)$ is the ratio of output electrons to incident photons, R is the reflection coefficient and k coefficient of photons. Pv represents the probability that light absorption may excite the electrons to a level greater than the vacuum level. Whereas Ps represents the probability that electrons reaching the photocathode surface may be released into the vacuum. L is the mean escape length of excited electrons and v is the frequency of light.

Electron trajectory

The voltage applied to the electrode, i.e. the electric field as well as the photocathode shape (planar or spherical window) influences the electron trajectory in a PMT. These parameters determine the efficiency of focusing of the photoelectrons emitted from the photocathode onto the first dynode. The impact between photoelectrons and first dynode causes the emission of secondary electrons. This process continues in a cascade from dynode to dynode generating a current signal at the anode. The electron trajectory must be carefully designed, in order to increase the collection efficiency of each dynode. Figure 2.17 shows the typical electron trajectories within a PMT [HAM07].
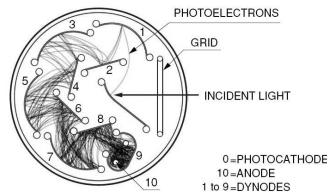
Figure 2.17: Cross section of a PMT showing the electron trajectories. Figure from [HAM07].

Electron multiplier

As explained before, photoelectrons emitted from the photocathode are multiplied by the first dynode through the last dynode amplifying the current. This current amplification depends mainly on the number and material of the dynodes. The most common materials used for dynodes are alkali antimony, beryllium oxide (BeO), magnesium oxide (MgO) and gallium phosphide (GaP, GaAsP). Dynode characteristics must be defined in accordance with the application [HAM07].

Chapter 3

Material Selection and Characterization

In this dissertation, the cell concentration within microfluidic systems was determined by means of a fluorescence detection method. The fluorescence intensity emitted by the ensemble of cells immobilized onto the inside surfaces of a system were detected by an optical sensor. Hence, materials comprising the microfluidic device, such as substrate and coating material should show low background fluorescence intensities. Fluorescence signal representing the concentration of contamination in raw milk can be measured, when substrate and coating materials exhibit very low background fluorescence levels or when the emitted signal from labeled cells are higher than background fluorescence. In order to find suited substrate and coating materials for cell immobilization and subsequent detection, different materials were characterized in this chapter. This characterization is described in terms of biocompatibility, biofunctionality and emitted background fluorescence levels.

3.1 Substrate material

A wide variety of plastic materials and polymers have gained more attention since these materials could be used for optical and biomedical applications. One of the advantages using plastic materials is the ability to structure them by methods such as hot embossing and injection molding allowing rapid prototyping of polymer microsystems. These methods offer an attractive alternative to the techniques currently being used to fabricate microsystems, because these materials are potentially a source of low cost components as explained in section 2.4.5. Another advantage using plastic material is the wide available variety of plastic materials. Examples of the more popular plastic materials include polymethylmethacrylate (PMMA), polycarbonate (PC), polystyrene (PS) and cyclic olefin copolymer (COC). From these materials, PMMA and PC are the most widely used plastic materials in the microfluidic area [BL02].

Although, there is a wide variety of plastic materials, recent research works have shown that these materials exhibit high autofluorescence [PNL+05, WFS+01] limiting its use in BioMEMS applications. Autofluorescence can reduce the sensitivity of immunoassay systems based on the measurement of fluorescent labeling of cells leading to wrong results. Thus, a good optical quality including low autofluorescence of plastic materials is crucial for the sensitive detection of specific cells by using the fluorescence detection technique. Previous research shows that COC and PMMA exhibit the lowest autofluorescence levels followed by PC and PS [HY03].

Nevertheless, results in [PNL+05] indicates that microfluidic systems exhibited higher autofluorescence than raw plastic materials from which they have been fabricated. Hence, in this dissertation several polymer samples materials and fabricated microfluidic systems are evaluated with the purpose to determine optical characteristics of each polymer under the same conditions. Available materials for this test include PC, PS, PMMA injection molded systems, systems made of COC and COC raw material. There are various types of raw PMMA materials such as PMMA XT and PMMA GS, which are commercially available. These materials were also examined.

3.1.1 Optical properties

In order to select the most appropriate plastic material, optical characteristics according to the setup of the biosensor must be studied. Based on the protocols established by ttz [ttz10] and RIKILT [rik10], fluorescent dye Phycoerythrin and Alexa532/4G10 were used as labeled detecting antibody. Thus, a bright green laser at a wavelength of 532nm was selected for illumination. All available polymer materials were characterized under this laser excitation to evaluate the background signal. This optical setup has been designed and installed by Optotek (see section 7.3.6). Each material was measured at least three times on different non-overlapping positions to evaluate also its uniformity. The measurement of each point took around 10 sec and during that time, the material was illuminated with an excitation laser. The photomultiplier tube (PMT) signal and laser intensity were sampled every 0.5 sec. All the data were normalized to the same laser strength assuming linear dependence of laser strength and PMT signal [opt10]. In that way the laser intensity fluctuation was compensated and the measurement error was lowered significantly. From corrected values of PMT signal, the average and standard variation was computed. The resulting value in conjunction with standard variation represents fluorescence intensity of evaluated materials.

Polymer raw materials

According to the measurement procedure described earlier, background flu-
orescence of PC, PS and PMMA from different providers were measured and
compared under similar conditions. The results are shown in table 3.1. The last
three columns of this table represent three statistic measures for a particular
sample. Mean and standard deviation (St.Dev.) values represent the current on
PMT in nA. These measurements reflect the inhomogeneity of each material.
As observed in this table, the lowest variation was obtained for PMMA and
PMMA GS samples being the most homogeneous materials, while PS is the
most inhomogeneous material showing extreme variability in measured signals.
It must be noted that this non-uniformity of the substrate can significantly
affect the sensing performance of the biosensor.

Table 3.1: Background fluorescence of different plastic materials such polycarbonate
(PC), polystyrene (PS) and polymethylmethacrylate (PMMA). The
materials were acquired from thinXXS Microtechnology AG [thi10], Jose
Weiss Plastic GmbH [Jos10] and Fraunhofer IFAM [Fra10].

Material	Provider	Thickness [mm]	Mean [nA]	St.Dev. [nA]	Rel. Err nA/mm
PMMA	thinXXS	1	150.09	1.85	0.012
			153.51	2.18	0.014
			156.09	2.86	0.018
PMMA XT	Josef Weiss Plastic GmbH	2	105.40	2.10	0.020
			105.60	1.80	0.017
			174.30	2.60	0.015
PMMA GS	Josef Weiss Plastic GmbH	2	86.20	1.60	0.018
			79.20	1.70	0.021
			81.10	1.50	0.019
PS	thinXXS	1	57.31	1.43	0.025
			48.18	1.44	0.030
			220.35	2.84	0.013
PC	thinXXS	1	372.45	3.24	0.009
			392.81	2.83	0.007
			379.45	4.27	0.011

As shown in the table above, samples of plastic materials with thicknesses of
1mm and 2mm were used for the characterization. Samples having the same
thickness are not commercially available for testing. Consequently, a linear

normalization to the initial fluorescence intensities must be applied in order to identify the magnitude of intensity of each material under the same conditions. The normalized results are shown in figure 3.1, where background fluorescence of each sample is represented by current in nA.

From these results, PMMA GS is the most appropriate material to be used as substrate, because it has the lowest background fluorescence and good uniformity. However, some difficulties could be presented using PMMA as substrate material, because its values vary depending on where it comes from. Different fluorescence intensities were measured from the material characterized as PMMA. For example, PMMA material from Josef Weiss Plastic GmbH with 2mm of thickness has lower signal than PMMA from thinXXS with 1mm of thickness. These materials may be chemically the same, but they are optically different. This variability between materials is due to the fact that they are from different provider, who has probably processed them in different ways or because the materials are even from different series of the same manufacturer.
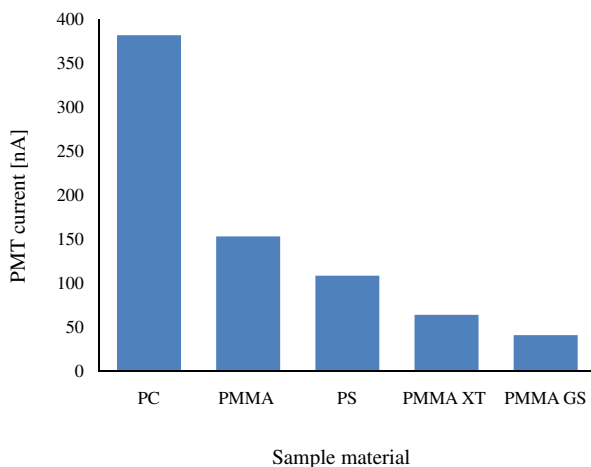
Figure 3.1: Comparison of background fluorescence of the different plastic materials types. These results correspond to normalized fluorescence intensities.

From the last results, PMMA could be identified as the most appropriate polymer to be used as substrate material. In order to find the most suitable PMMA type and confirm the usability of PMMA GS, additional PMMA types such as PMMA 6N S000, PMMA 7H and PMMA 8N have been measured using the same optical setup. According to the provider [Evo10], these PMMA series might be suited for biological applications because of their excellent optical

properties. Additional PMMA materials were provided by Evonik Industries [Evo10] and Fraunhofer IFAM [Fra10] for testing. Background fluorescence of different PMMA types were measured and compared with PMMA GS. The results are shown in table 3.2.

Table 3.2: Background fluorescence of different PMMA types. Measured signals from PMMA 6N S000, PMMA 8N and PMMA 7H provided by Evonik [Evo10] Industries and Fraunhofer IFAM [Fra10], respectively. Measurement of PMMA XT and PMMA GS have been again performed using the same optical setup together with the additional PMMA samples.

Material	Provider	Thickness [mm]	Mean [nA]	St.Dev. [nA]	Rel. Err nA/mm
PMMA GS	Josef Weiss Plastic GmbH	2	79.0	1.7	0.021
			86.2	1.6	0.018
			79.2	1.7	0.021
			81,1	1.5	0.019
PMMA XT	Josef Weiss Plastic GmbH	2	104.2	1.8	0.017
			105.4	2.1	0.020
			105.6	1.8	0.017
			174.3	2.6	0.015
PMMA 6N S000	Evonik	3	395.1	4.3	0.011
			677.4	13.9	0.020
			617.8	15.0	0.024
			394.6	4.7	0.012
PMMA 7H	Fraunhofer IFAM	2.5	189.4	2.7	0.014
			184.8	2.4	0.013
			232.9	2.9	0.012
			161.0	2.1	0.013
PMMA 8N	Fraunhofer IFAM	3	275.3	3.7	0.014
			502.9	13.0	0.026
			486.4	15.3	0.032
			283.6	2.9	0.010

As shown in the table above, PMMA materials with thicknesses between 2mm and 3mm were acquired for testing. Therefore, a linear normalization must be also applied to identify fluorescence intensity under the same conditions. The normalized results are shown in figure 3.2. According to these results, the best candidate for sensitive fluorescence detection is PMMA GS bare exhibiting very low background fluorescence and good uniformity.
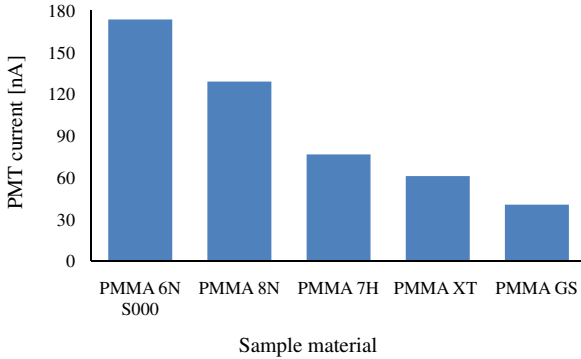
Figure 3.2: Normalized autofluorescence intensities of the different PMMA types.

3.1.2 Substrate preparation

Considering the previous analysis, PMMA GS has been selected as the best option to be used as substrate material due to its good optical properties and homogeneity. Consequently, PMMA GS has been utilized as substrate material for the deposition of biocompatible thin films to evaluate surface conditions for cell adhesion. The first step in the whole process was surface preparation. First, 2mm thick PMMA GS material was cut into 100mm diameter allowing easy handling and processing under clean room conditions. PMMA GS substrates were immersed for 30 min in an ultrasonic bath with sodium dodecyl sulfate to eliminate undesirable residues and contaminations on PMMA GS surfaces. Afterwards, the substrates were cleaned with deionized water and subsequently dried in an oven at 75°C for at least 1 hour.

PMMA GS substrates are particularly suitable for the fabrication of future microfluidic devices because of its transparency and low cost. However, their surface properties do not fulfill the requirements regarding wettability [HBO03] causing poor adhesion between coating layer and the surface of PMMA GS. Hence, additional surface modification on PMMA GS material was performed to increase the surface energy and thus improve adhesion properties. To achieve that, PMMA wafers were treated with oxygen plasma producing wettable surfaces, and consequently enhancing the adhesion with the coating material. Contact angle measurement has been the method used to characterize the adhesive properties. To identify the effective plasma procedure, the contact angle with water on PMMA GS was measured at different plasma parameters. This plasma treatment procedure will be introduced in Chapter 5, subsection 5.3.1. Once the PMMA GS substrates are completely cleaned and treated, they are ready for the deposition of biocompatible thin layers.

3.2 Biocompatible materials for cell immobilization

Biocompatible surfaces have become very important in the development of biosensing systems, where the immobilization of biomolecules takes place. Here, the combination of suitable surfaces with specific biological activation procedure is essential for effective binding of biomolecules. Choosing the proper surface as a solid support is an important step in immunoassay developments, especially if the assay is evaluated by means of optical sensors as illustrated in figure 3.3.
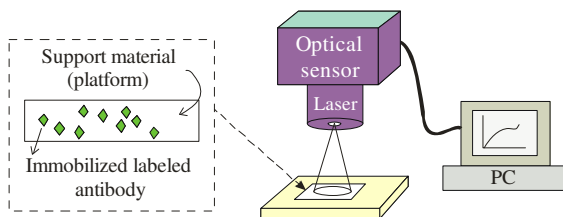
Figure 3.3: Schematic representation of a basic measurement system for biochemical assays using an optical sensor [GSC+09].

In order to find an optimal material combination for cell immobilization and subsequent detection, different biocompatible materials were selected and evaluated in terms of biocompatibility, biofunctionality and emitted fluorescence levels. Polymer materials such as photopatternable silicon (PPS), polydimethylsiloxane (PDMS), Vitralit®UC6772, photoresist SU-8, resin 1002F and its derivate photoresist 1002F have been selected as alternative materials for cell immobilization. The efficiency of each polymer material has been experimentally determined by comparing binding capacity.

Photoresist SU-8 [MSJ+06, GSK+09], Vitralit®UC6772, resin 1002F and its derivate photoresist 1002F [PWS+07] were mainly chosen in this thesis because of their chemical composition. These polymer materials have a high density of epoxy groups, which are particularly suited for the covalent attachment between the protein and the support material (see subsection 3.2.1). Using an appropriate functionalization method, polymer with epoxy groups are efficient reactive surfaces to form covalent immobilization of biomolecules such as antigens, antibodies, proteins, DNA or RNA [JPRM07]. Additional materials such as photopatternable silicon (PPS) and polydimethylsiloxane (PDMS) were chosen mainly because of their biocompatibility as confirmed in prior works [DTV08, dSdO01]. Although, these polymers do not contain any reactive epoxy

groups, published results demonstrated that PPS and PDMS have excellent biocompatibility and low background fluorescence. PPS, SU-8 and photoresist 1002F have been examined regarding to binding efficiency, background fluorescence and ability to create microstructures [JPRM07, DTV08, PWS+07, GSK+09].

In this dissertation, important surface properties such as biocompatibility, biofunctionality, wettability, roughness and emitted fluorescence values of thin films have been evaluated. The best suited polymer material has been selected with a combination of biomolecules immobilization experiments and fluorescence measurements. The results regarding autofluorescence intensities and biocompatibility are shown in sections 3.2.5 and 3.2.6 respectively.

3.2.1 Protein binding to epoxy groups

Proteins can be immobilized onto a surface through covalent interactions and physical immobilization including ionic bonds and hydrophobic interactions [RZF07]. In many cases, covalent immobilization is used because this process ensures an irreversible and selective binding. Covalent bonds involve a reaction between the surface of the support material and the surface of a protein. These surfaces must therefore provide functional groups to enable an appropriate and strong chemical binding. Epoxy-activated supports present excellent properties allowing the development of easy protocols for protein immobilization, because of its stability at neutral pH values and wet conditions. Moreover, epoxy groups are able to react with different groups of the proteins such as amino ($-NH_2$), hydroxyl ($-OH$) or thiol moieties ($-SH$) [MTFL+03, RZF07] forming extremely strong linkages. The chemistry of the epoxy group and its potential for covalent binging are summarized in the following paragraphs.

Chemistry of the epoxy group

The epoxy group is a cyclic ether with three-member ring comprising two carbon atoms and one oxygen atom that form a particularly geometry as shown in figure 3.4. The most important consequence of the geometry of the epoxy group, as also known as oxirane ring, is the reactivity towards other functional groups. Epoxy rings are very reactive electrophilic groups and thereby, they can form a covalent bond with the nucleophilic functional groups of the proteins (amino, thio, hydroxyl ones), which involves the sharing of a pair of electrons resulting in a strong and irreversible bond [MR04, RZF07].
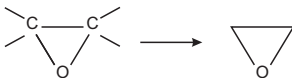
Figure 3.4: Chemical representations of the epoxy group. The epoxy group is polarized by the different electronegativities of carbon and oxygen. Oxygen has a negative partial charge and carbon is partially positively charged [Kir87].

Figure 3.5 shows the reaction of epoxy group with hydrogen atoms. As observed in this figure, each carbon of the epoxy ring is enumerated indicating the different partial charge, where carbon atom number 1 carries the strongest positive partial charge [Kir87]. The epoxy oxygen atom remains with carbon atom 2 of the epoxy resin, whereas the addition of other component takes place at the carbon atom 1.
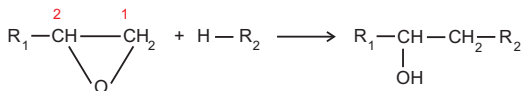
Figure 3.5: Chemical reaction when hydrogen atoms are added onto the epoxy ring [Kir87].

Epoxy resin

Epoxy resin is a polymer characterized for having epoxy groups. The rings of the epoxy groups are active bonding sites for a variety of chemicals that react with the polymer forming a bridge to another polymer, creating a crosslink [Str06]. This crosslinking is initiated by opening the epoxy ring by a reactive group on the end of another molecule. Generally, this molecule is also known as hardener because it hardens or cures the epoxy. In practice, compounds with amino groups are used as curing agents, which react very fast and even at low temperatures [Kir87]. Figure 3.6 shows the reaction of the epoxy group with the reactive amine group. As observed in this figure, by opening the ring, two new bonds are formed as follows: one with a carbon atom that was in the epoxy ring and the second between the oxygen of the epoxy ring and the hydrogen that was on the amine.

The bond between the amine and the carbon is the key bond in crosslinking, whereas the OH group represents the bondability of epoxy resin [Str06]. Usually, the amine molecule has another amine group on the other end and thereby, it can react with a second epoxy molecule.
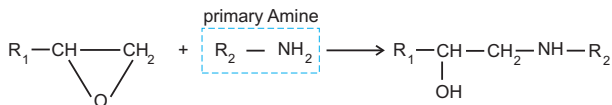
Figure 3.6: Chemical reaction of the epoxy group with primary amine [Kir87].

Covalent binding on epoxy supports

The epoxy groups form covalent bond with amino, hydroxyl or thiol moieties via ring-opening reaction facilitated under basic conditions [T. 08]. Then, material containing epoxy groups can be used to bind proteins, nucleic acids, sugars and carbohydrates and other organic molecules (see figure 3.7). [T. 08] describes the necessary protocols to immobilize thiol-, amine-, or hydroxyl-containing ligands with the proper pH level.
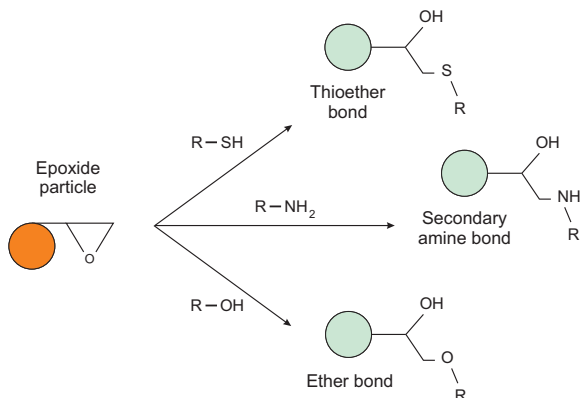
Figure 3.7: Epoxy groups can be coupled with amine, thiol-, or hydroxyl- containing molecules [T. 08].

Protein immobilization on epoxy surfaces takes places by means of two steps: in the first step, a physical adsorption of the protein on the support is produced and in the second step, a covalent reaction between the absorbed protein and the epoxy groups of the support material occurs. The epoxy groups are able to react with a high variety of reactive groups that are on the protein surface such as amino ($-NH_2$), hydroxyl ($-OH$) or thiol moieties ($-SH$). Besides the amount of epoxy groups of the surface, it must exhibit hydrophobic behavior properties [MFLA$^+$00]. The process to generate protein immobilization is represented in figure 3.8.
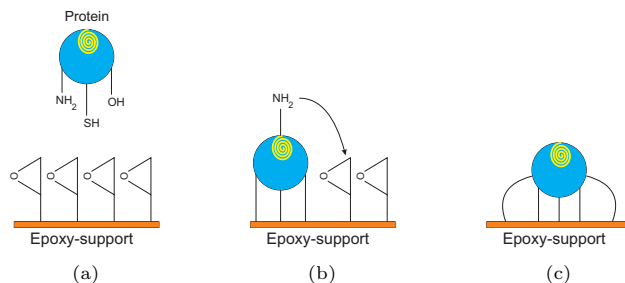
Figure 3.8: Protein binding on an epoxy support (a) Proteins having reactive groups such as amino (-NH_2), hydroxyl (-OH) or thiol moieties (-SH) can react with the epoxy support. (b) Proteins are immobilized by physical adsorption such as hydrophobic interactions. (c) Covalent binding between the absorbed protein and the epoxy support takes place.

As observed in the figure above, covalent binding could be achieved only when an adsorption interaction between the surface of the protein and the epoxy support exists. Because of this requirement, epoxy supports used for protein immobilization must show hydrophobic behavior.

Despite the positive results achieved using epoxy supports, their use can be limited in some cases. These limitations are based mainly on the hydrophilic properties of the surface of the proteins as well as of the epoxy support. Hydrophilic surfaces are not well suited for protein adsorption ability and consequently, not able for covalent binding [MFLA+00, MTFL+03]. Several protocols have been reported in the last years for improving the functionality of epoxy supports and thus hydrophobicity will be not longer necessary for protein attachment. The future development of the epoxy supports should consider preparing hydrophilic supports, keeping the good mechanical properties [MFLA+00, MGP+07].

3.2.2 Selected biocompatible materials

The following subsections introduce selected biocompatible surfaces, which might provide excellent characteristics for cell immobilization. Solid supports or thin biocompatible layers must offer reactive chemical groups to guarantee that biomolecules bind to surfaces with strong chemical binding properties. The chemical structure of the main components of each polymer is also illustrated.

Photoresist SU-8

Photoresist SU-8 acquired from micro resist technology [mic10a] is currently used for several Lab-on-a-Chip (LOC) applications due to its biocompatibility and excellent chemical properties [BKJ+08, DSM09a, HMD+07, JFG+01, LLCC02, MSJ+06, RMT+05]. This photoresist is a negative polymer, which is produced in different viscosities allowing the fabrication of structures with thicknesses from $1\mu m$ to 2mm [LTK05]. Basically, SU-8 is prepared by mixing epon SU-8 resin in a photoinitiator and a solvent.

Epon epoxy resin SU-8 is crosslinked polymer that has eight epoxy groups in its monomer forms as shown in figure 3.9. The amount of the solvent determines the viscosity and consequently, the thickness of the SU-8 film. The epoxy groups of SU-8 act as active molecular group to form crosslink reaction and thus ensuring biomolecules binding. Previous attempts ([GSK+09, DSM09a, JPRM07]) have proved that specific biomolecules could be successfully immobilized on SU-8 photoresist forming covalent bonds due to its epoxy chemistry.
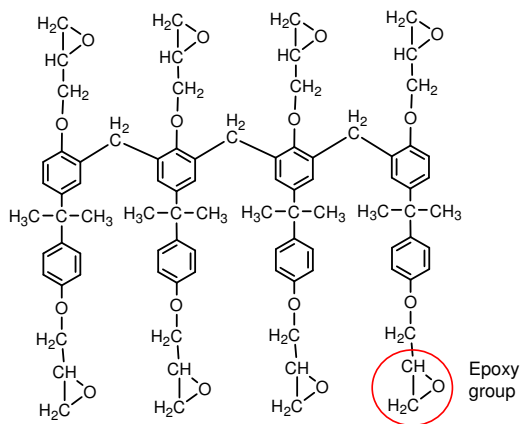
Figure 3.9: Molecular structure of Epon SU-8 [mic10a]. One of the eight epoxy groups is indicated.

Resin 1002F

Epon resin 1002F provided by Miller-Stephenson [Mil10] is a solid polymer that has epoxy groups as well as SU-8, but it contains only two epoxy groups per molecule as illustrated in figure 3.10. Usually, this epoxy resin could be used in

high performance hot melt adhesives, molding powders and in powder coatings [HEX09]. Samples containing resin 1002F were prepared in order to determine, whether this polymer can be used as support material for cell immobilization. It must be noted that resin 1002F cannot be utilized to form microstructures. However, this material can be used as adhesive layer.
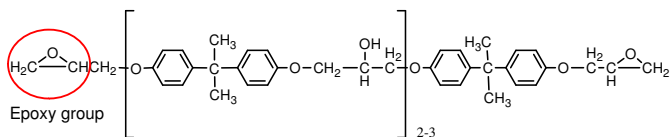
Figure 3.10: Molecular structure of Epon 1002F, poly (Bisphenol- A-co-epichlorohydrin, diglycidyl ether terminated) [HEX09]. One of the two epoxy groups is indicated.

Photoresist 1002F

Photoresist 1002F is a new material that as well as SU-8 is composed of: Epon resin 1002F (figure 3.10), a solvent (typically ç-butyrolactone (GBL)) and a photoinitiator as depicted in figure 3.11. This material has been recently developed and employed to fabricate microstructures to be used in biological applications [PWS+09]. Samples containing photoresist 1002F were prepared to evaluate its ability for cell immobilization. Resin 1002F in solid form was acquired from Miller-Stephenson [Mil10] and additional materials required for preparing photoresist 1002F such as triarylsulfonium hexafluoroantimonate and solvent (ç-butyrolactone GBL) were obtained from Sigma Aldrich [Sig10].
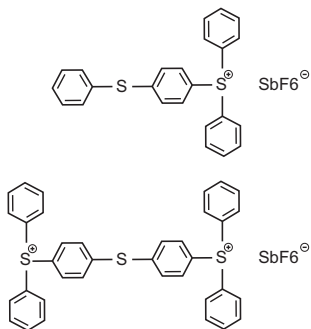
Figure 3.11: Molecular structure of the photoinitiator triarylsulfonium hexafluoroantimonate salts [Sig10].

Photoresist 1002F shows adequate chemical characteristics for biomolecules adhesion on its surface [PWS$^+$07]. Moreover, this material exhibits lower background fluorescence levels than SU-8 as illustrated in figure 3.12. This suggests that photoresist 1002F can be used for applications, in which SU-8 is currently used, since photoresist 1002F has similar chemical structure like the traditional photoresist SU-8. By using the photopolymer 1002F, the signal-to-noise ratio increases and improves the efficiency for fluorescence measurement. Consequently, small volume of labeled proteins could be detected, which is a requirement in biosensing systems.
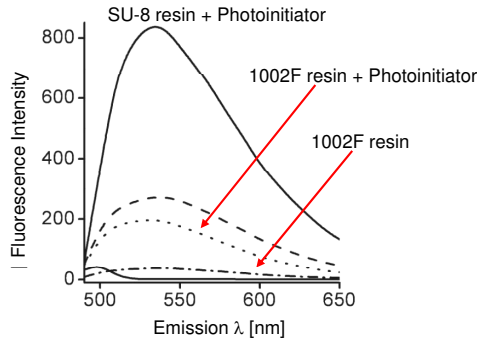
Figure 3.12: Fluorescence intensities of SU-8 and resin 1002F, excited at 485nm, max. 540nm [PWS$^+$07].

Photopatternable Silicone (PPS WL 5150/ PPS WL 5351)

Photopatternable silicon (PPS) provided by Down Corning Corporation was also chosen according to the suitability for patterning biomolecules. Although the chemical composition of PPS is primarily polymethylhydrosiloxane as shown in figure 3.13 and it does not contain any epoxy groups as SU-8 and resin 1002F. Previous published results demonstrated that PPS has excellent biocompatibility and good properties to fabricate microstructures [DTV08]. The complete chemical composition of PPS is not available, but as well as photoresist 1002F and SU-8, PPS is composed of silicon resin dissolved in a solvent, typically mesitylene [SHG$^+$03].

In [DTV08], it was also demonstrated that PPS exhibits low background fluorescence as compared to other biocompatible materials. This comparison is shown in figure 3.15. For this reason, PPS might be a good option for sensitive detection of biomarkers in the current dissertation.
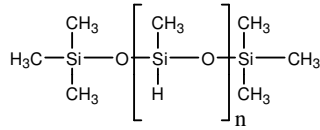
Figure 3.13: Chemical structure of polymethylhydrosiloxane [Dow10].

Polydimethylsiloxane (PDMS)

Polydimethylsiloxane provided by Dow Corning [Dow10] is a popular material that has been widely used for the fabrication of microfluidic devices based on soft lithographic techniques. Soft lithography is an inexpensive technique that does not require any clean room facilities or any expensive equipment. Consequently, PDMS structures can be fabricated in an easy low cost and fast way using only a mold structure. Besides an easy fabrication procedure, PDMS has low autofluorescence (see figure 3.15) and has good biocompatible properties [LJRW04]. Thus, it is a promising material for use in cell immobilization.
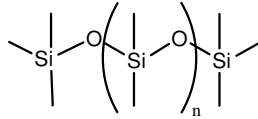
Figure 3.14: Molecular structure of PDMS.
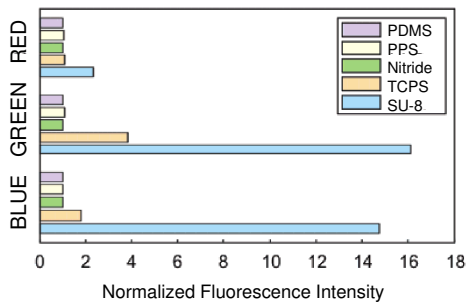
Figure 3.15: Quantitative comparison of fluorescence intensities of SU-8, PPS, PDMS among other substrates in red, green and blue channels [DTV08].

Vitralit ®UC6772

Vitralit®UC6772 provided by Panacol [Pan10] is a material that is normally used as adhesive component by means of UV exposure. Depending on the high-energy UV light, the curing time is mostly between 0.5 and 60 sec [Pan09]. Vitralit®UC6772 is composed of the materials shown in figure 3.16.
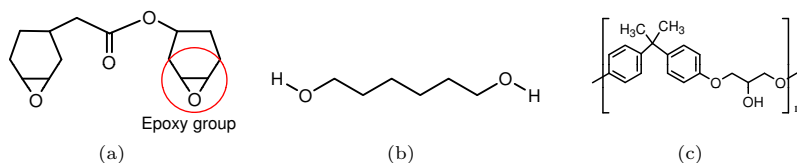
Figure 3.16: Chemical structures of ingredients in Vitralit®UC6772 and their ratio [Pan09] (a) $25 - 50\%$ 3,4-Epoxycyclohexylmethyl 3,4-epoxycyclohexanecarboxylate. One of the epoxy groups is indicated. (b) $25 - 50\%$ 1,6-Hexanediol. (c) $10 - 25\%$ Poly(Bisphenol A-co-epichlorohydrin).

Vitralit®UC6772 (hereinafter, UC6772) has been utilized up to now to seal single components systems within the space of only a few seconds. The properties of this bond material and its applicability has not been studied so far for cell immobilization. In the current application, the amount of epoxy groups within this adhesive material can make it an attractive alternative for protein immobilization on its surface as demonstrated by the epoxy groups in SU-8 [GSK+09, MSJ+06] and photoresist 1002F [PWS+07].

3.2.3 Thin layers preparation

Polymer materials were prepared under clean room conditions using PMMA GS as substrate material. Resin 1002F in liquid form was made by dissolving resin 1002F in GBL at a ratio 1:1. Photoresist 1002F was prepared using solvent GBL and photoinitiator as indicated in 3.2.2. PDMS was prepared by mixing the elastomer monomer (Sylgard 184A) and the curing agent (Sylgard 184B) in a ratio of 10:1. The deposition of uniform layers could be achieved by means of spin coating process resulting thickness from 5µm until 7µm. Table 3.3 summarizes the processing parameter used for each layer and resulting thickness.

Table 3.3: Parameters for layers preparation and their respective thicknesses.

Polymer material	Soft bake	Exposure time [sec]	Post bake time [sec]	Thickness [µm]
Photoresist SU-8	65°C 1 min	60	65°C, 1 min 95°C, 1 min	5
Epon resin 1002F	65°C, 1 min 95°C, 3 min	-	-	5
Photoresist 1002F	65°C, 1 min 95°C, 3 min	40	65°C, 1 min 95°C, 1 min	5
PPS WL-5150	75°C 120 min	30	65°C, 1 min 95°C, 20 min	7
PPS WL-5351	75°C 120 min	30	65°C, 1 min 95°C, 10 min	7
Vitralit® UC6772	65°C, 1 min 95°C, 3 min	60	65°C, 1 min 95°C, 1 min	6
PDMS	-	-	-	7

After the pretreatment process applied on PMMA GS substrate (see subsection 3.1.2) and after mixing the components, thin layers of biocompatible materials could be deposited on PMMA GS substrate for testing. Spin coating process is followed by a soft bake process using a hot plate or a convection oven to remove solvents.

The majority of the layers were then polymerized via UV exposure, followed by a post bake step. Exposure assessment in resin 1002F and PDMS was not required, because they do not have any UV curable component. According to [DTV08], PPS films must be heated at 120°C on a hot plate between 3 and 5 min using silicon wafer as substrate material. Soft bake procedure at this temperature could not be realized because PMMA GS can breakdown at high temperatures. Then, this step was replaced by a soft bake step in a convection oven at 75°C for two hours.

3.2.4 Surface characterization

Once thin films were deposited onto a PMMA GS substrate, wettability properties and surface roughness profile were evaluated. Water contact angle was used in this study as indicator of surface wettability and a profilometry method was utilized to examine surface roughness and uniformity. To assess the wettability

of the surfaces, measurement of deionized water contact angle was carried out by a goniometer (DSA-10, Krüss GmbH Hamburg) using the software DSA-II Version 2.1. In this implementation, a drop of water having a volume of 4μL was automatically deposited on coated PMMA GS substrate. Immediately after deposition, the contact angle between the drop and the substrate was measured to avoid evaporation of the water. Contact angle measurement was performed 10 times in different points on the wafer in order to verify the accuracy and precision of displayed measurements.

Measurements concerning the surface roughness profile of thin layers were performed by means of profilometry using a Sensor Scan 2300 profilometer provided by Halcyonics. 3D measurements were performed with an optical pro-filometer (Plμ2300, Sensofar) and a 20-folds objective (420-folds magnification) to distinguish the surface roughness. Two individual measurements were made on each monolayer to validate first roughness value Sa. The size of each single measurement area was 477 x 636μm^2 and contained 442368 measurement data points from which the surface roughness Sa and the maximum height of the surface Sz were calculated according to ISO 25178. The 3D data analysis was performed using SensoMap Plus software (Sensofar) version 5.0.3.4995. Neither filters, e.g., median or Fourier nor restoring of missing data points were used for the calculation of the roughness values.

Contact angle

Water contact angle was used as indicator of wettability of the surfaces, which strongly influences cell binding. When a water drop is completely spread out onto the polymer and the contact angle is close to 0°, the surface is strongly hydrophilic. While a hydrophobic solid support has a water contact angle between 70° and 90°. Angles up to 90° indicate high wettability of the surface. Contact angle greater than 90° corresponds to a non-wettable surface meaning that the fluid does not have sufficient contact with the surface forming a compact liquid droplet.

Table 3.4 shows the water contact angle of untreated polymer surfaces, which were analyzed in the scope of this dissertation. The contact angle on PDMS material is about 112° exhibiting hydrophobic behavior and poor wettability. The water contact angle of resin 1002F, photoresist 1002F, UC6772 and SU-8 is between 69 and 74° showing also hydrophob behavior, followed by PPS layer, which has 89° water drop contact angle.

Table 3.4: Water contact angle of untreated polymer surfaces. A drop of water (4μL) was deposited on coated PMMA GS substrate. After drop water deposition, the contact angle between the drop and the substrate was measured by a goniometer (DSA-10, Krüss GmbH Hamburg).

Polymer	Contact angle [°]
Photoresist SU-8	69.7
Photoresist 1002F	69.7
Resin 1002F	70.1
Vitralit®UC6772	74.4
PPS WL-5150	89.4
PPS WL-5351	89.6
PDMS	112.4

The results indicate that all thin layers showed hydrophobic properties. According to [PMGS05, CCS+02, GH06] cell adhesion takes place onto all these thin polymer surfaces and it could be also demonstrated in this thesis (see subsection 3.2.6). Cell adhesion in flow conditions depends considerably on the time domain of the cell surface interaction meaning the contact between cells and walls, ceiling or bottom of the microchannel. Hence, cell adhesion profile depends not only on the wettability of the surface, but also on the channel geometry as established in [GKA+09]. In order to demonstrate the effect of channel geometry on biomolecules immobilization, cell interaction within different fluidic geometries was also analyzed (see Chapters 4 and 6).

Surface profilometry

In table 3.5, some measurements regarding the surface roughness averages (Sa) are presented. In accordance with the measurements performed by a profilometer; SU-8, resin 1002F, photoresist 1002F and UC6772 have similar roughness values of approximately 25nm. The roughness value of PPS WL-5351 is 21.92nm indicating that this polymer has the smoothest surface, whereas PPS WL-5150 and PDMS have the roughest surfaces with 27.62nm and 31.53nm, respectively.

A series of topographic images have been also obtained for each polymer film with different magnifications. 3D data images together with total surface areas of PPS WL-5150, PPS WL-5351, UC6772 and PDMS are depicted in figure 3.17. These images reveal smooth and homogenous surfaces, free of scratches and with roughness below of 2nm.

Table 3.5: Roughness values obtained in an area of 477 x 636μm^2 using a Sensor Scan 2300 profilometer provided by Halcyonics.

Polymer	Surface roughness average Sa [nm]
Photoresist SU-8	24.82
Photoresist 1002F	25.63
Resin 1002F	25.63
Vitralit®UC6772	24.85
PPS WL-5150	27.62
PPS WL-5351	21.92
PDMS	31.53

(a) PPS WL-5150, Sa = 27.62nm

(b) PPS WL-5351, Sa = 21.92nm

(c) Vitralit® UC 6772, Sa = 24.86nm

(d) PDMS, Sa = 31.53nm
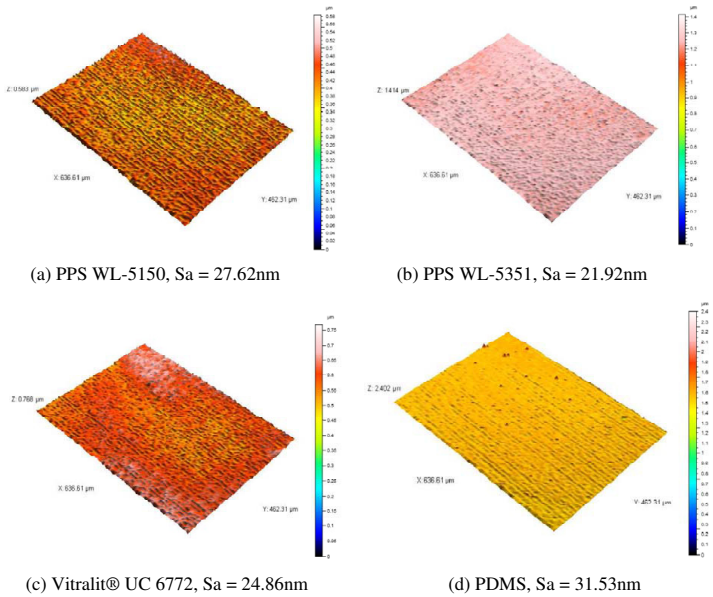
Figure 3.17: 3D surface roughness maps of PPS, UC6772 and PDMS. Images were obtained from SensoMap Plus software (Sensofar). 3D images of the rest of the polymer are not shown in this thesis, because of the similarity of roughness values.

3.2.5 Autofluorescence of thin polymeric materials

Autofluorescence of each biocompatible surface was measured by means of the same optical setup used to characterize the substrate material (see sections 3.1.1 and 7.3.6). Each material was measured at least three times on different non-overlapping positions to evaluate also the uniformity of the material. Average measurements are presented in figure 3.18. As observed in this figure, all thin polymer material proposed in this thesis emitted light in the green region of the visible spectrum. Biocompatible polymers exhibit autofluorescence by itself as well as all substrate materials tested in subsection 3.1.1. Considering these results, it can be assumed that this autofluorescence signal is probably caused by the high conjugate structure of the polymer. Consequently, autofluorescence intensity may vary in each polymer and it depends on the chemical properties or polymer composition (see more detail in section 3.4).
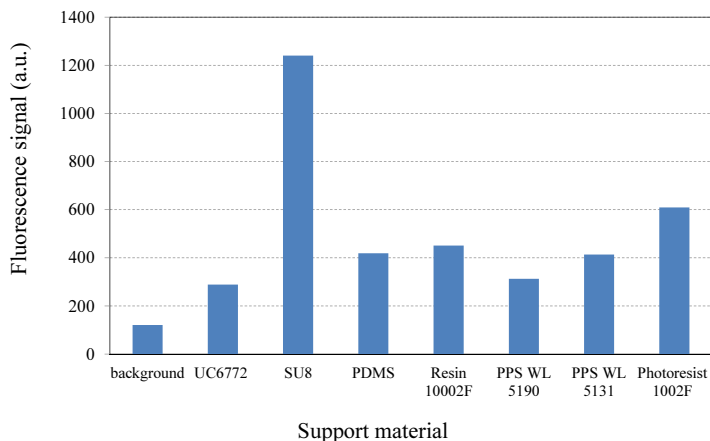
Figure 3.18: Comparison of autofluorescence intensities emitted by different thin polymer materials [GSC$^+$09].

Since thin biocompatible polymers are deposited on PMMA GS substrates, its autofluorescence intensity must be considered. Hence, emitted autofluorescence background shown in the figure above is attributed to the composition of the whole sample, which consists in PMMA GS as substrate material and the biocompatible polymer. From these results, SU-8 exhibits the highest background fluorescence levels, while UC6772 the lowest background fluorescence compared to all support materials examined here. The advantage of extremely low background fluorescence of UC6772 is that lower concentration of fluorescent label on its surface can be detected. Nevertheless, all polymer surfaces must

be evaluated concerning their biocompatibility. This evaluation comprises the total protein binding capacity including the weak and strong binding ability. These experiments are presented in the following subsection.

3.2.6 Biocompatibility

In order to prove the effectiveness of prepared layers for protein binding, the sandwich immunoassay technique based on the specific molecular recognition of a particular antibody with a certain antigen was performed. For the surface test, FITC (fluoresceinisothiocyanat) labeled protein A of staphylococcus aureus (Fluka, 82484) and FITC labeled anti-human antibody (BIOLOGO, FI-3000) were used. Fluorescent labeled proteins were selected because they can be immediately observed by means of a fluorescence microscope when a binding process takes place. For the immobilization process, 0.05mg/mL of protein A and 0.15mg/mL of anti-human antibody were used. Protein concentrations were added to PBS and after that, the resulting solution was deposited on each layer and incubated for 2 hours.

After incubation, a washing step was performed using 5mL of ultrapure water to remove all unbound proteins. Binding efficiency is evaluated subjectively under the fluorescence microscope (Axiovision, Zeiss) with an excitation wavelength of 450nm to 490nm. Pictures from coated surfaces were taken under same conditions and evaluated qualitatively. The results are shown in table 3.6. From these results, protein immobilization could be successfully demonstrated on all polymer surfaces. Molecule immobilization could take place on hydrophobic surfaces as explained in subsection 3.2.4. In order to evaluate how strong the binding between the protein and surfaces is, a washing step was performed after immobilization procedure. All biocompatible surfaces were tested under the same conditions.

After washing, protein binding on the surfaces was compared again using the pictures taken by the microscope. Immobilized molecules could be washed off easily on polymer such as PPS WL-5150 and PPS WL-5351 showing weak binding properties. In contrast to that, strong protein immobilization could be observed on all epoxy surfaces including resin 1002F, UC6772 and SU-8 after intensive washing. Figure 3.19 shows specific labeled proteins, which could be bound homogenously and strongly on respective surfaces. From the pictures and respective qualitative analysis, surface containing epoxy groups are the best suited surfaces for protein immobilization.

Table 3.6: Qualitative evaluation of protein binding efficiency on different polymer materials. Binding properties on prepared surfaces are characterized as follows: (-) no binding, (+) poor binding, (++) medium binding, (+++) high binding and (++++) best binding efficiency. Required experiments were performed by ttz/BIBIS.

Polymer	Binding results
Photoresist SU-8	++
Photoresist 1002F	+++
Resin 1002F	+++
Vitralit®UC6772	+++
PPS WL-5150	++++
PPS WL-5351	++++
PDMS	++

(a)   (b)   (c)
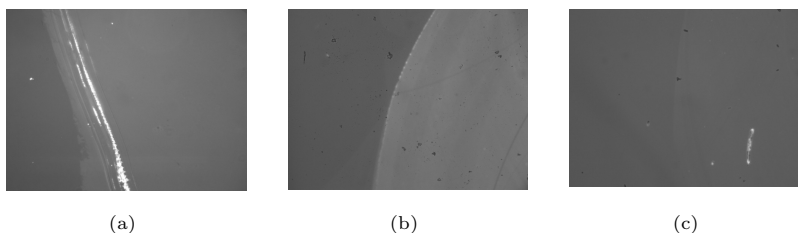
Figure 3.19: Protein enrichment on different polymer surfaces. The bright spot on the right demonstrates the successful immobilization of labeled proteins. The darker left side shows the plane surface. Pictures were taken with a wavelength of 512nm and with an exposure time of 5 sec. (a) Immobilized labeled proteins to UC6772. (b) Immobilized labeled proteins to SU-8. (c) Immobilized labeled proteins to resin 1002F.

According to the results shown in figure 3.19, UC6772 might be the best surface for protein enrichment followed by the photoresist SU-8. Protein immobilization also took place on the epoxy material resin 1002F. However, the amount of immobilized labeled protein was very low as shown in the respective picture. This poor immobilization might be caused by few amount of epoxy of resin 1002F as previously illustrated by its chemical structure (see figure 3.10).

From the results concerning biocompatibility, the presence of epoxy groups enables protein binding. In this thesis, protein binding took place on resin 1002F, SU-8 and UC6772 due to the presence of epoxy groups. Whereas, protein immobilization on PPS and PDMS surfaces might be generated by

hydrophobic properties. Based on these results, proteins bind mainly by weak interaction on hydrophobic surfaces as opposed to epoxy surface, which covalently reacts with protein surface creating strong cross links and thus result in a truly irreversible denaturation. The epoxy groups guarantee an efficient reaction ensuring a strong linkage between the biomolecules and the surface.

3.3 Identification of suitable biocompatible photopolymers: SU-8 vs. UC6772

In accordance with the results shown in subsections 3.2.5 and 3.2.6, SU-8 and UC6772 are the best suited surfaces for protein immobilization and subsequent detection. However, additional experiments using PMMA GS as substrate material, and SU-8 and UC6772 as coating material were performed to evaluate quantitatively binding efficiency and emitted background fluorescence.

3.3.1 Quantitative analysis of antibody binding

Supplementary experiments on SU-8 and UC6772 for comparing their effectiveness have been also performed. For this experiment, specific biomolecules were utilized. Mouse anti-mecoprop AB mixed with PBS was deposited and incubated onto selected epoxy surfaces followed by a blocking solution. Labeled Horseradish peroxidase (HRP) anti-Mouse was used as secondary antibody. The detection was performed by means of Tetramethylbenzidine (TMB) solution followed by a stop solution and quantification. Biomolecule immobilization efficiency on SU-8 and UC6772 surfaces was estimated by comparing relative adsorption profiles as illustrated in the following figure. As observed in figure 3.20, a negative and positive control were performed in order to evaluate binding affinity and effectiveness of the blocking solution respectively.

In the positive control, Anti-Mecoprop AB was deposited on the epoxy surfaces, followed by the deposition of a blocking solution to ensure non-unspecific binding of antibodies to the biocompatible surfaces. Then, HRP-labeled anti-Mouse was applied on pretreated surface that acts as detecting label. A measurable blue signal should be then produced indicating the binding of HPR-labeled antibody bind to anti-mecoprop AB. The intensity of the blue signal gives information about the binding efficiency of anti-mecoprop AB to the epoxy surfaces.

In the negative control, a blocking solution was deposited on the surface deactivating the biocompatible surface, followed by the deposition of HPR-labeled antibody. In this case, HPR-labeled antibody might not be bound to the deactivated epoxy surface and thus a strong or weak blue signal should be produced.
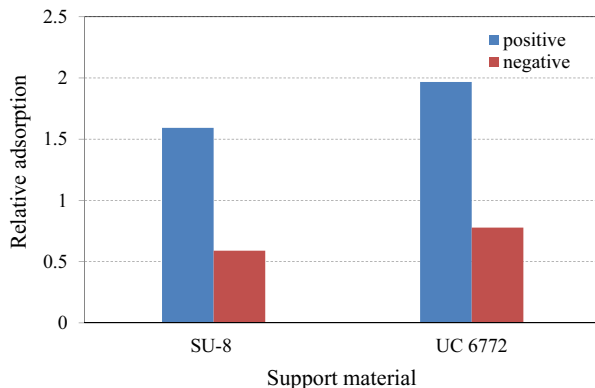
Figure 3.20: Immobilized Anti-Mecoprop AB on two different epoxy surfaces such as SU-8 and UC6772. A positive control took place in double regulation and negative control in single regulation [GSC⁺09].

As expected from previous experiments, both surfaces could be successfully activated for cell immobilization due to the epoxy groups. UC6772 and SU-8 could be also functionalized to block the affinity of epoxy groups and thus avoid the binding of non-specific proteins. By means of the positive and negative control, it could be determined which is the most appropriate surface for cell immobilization and for deactivation, respectively.

According to the results by the positive control method, the relative adsorption on UC6772 is 1.967, while on SU-8 is 1.593 indicating that UC6772 surfaces offer slightly higher sensitivity for antibody binding than SU-8. In contrast to that, by the negative control relative adsorption on SU-8 surfaces is 0.589, whereas on UC6772 surfaces is 0.778. These results show that SU-8 surfaces can be efficiently functionalized to avoid the binding of non-specific proteins as compared to UC6772, thus increasing sensitivity of the assay for quantification. Since surface bioactivation as well as surface deactivation are essential parameters for specificity, selectivity and sensitivity on the detection method, UC6772 and SU-8 surfaces have advantages and disadvantages to consider when performing immunoassay procedures.

3.3.2 Use of UC6772 and SU-8 in microfluidic technology

The selection of the fabrication process is considerably influenced by the proper-
ties of the photopolymer. Photolithography technique could be applicable when
the photopolymer SU-8 is used. In contrast to that, the use of UC6772 implies
a molding process such as injection molding or hot embossing method. SU-8
is a photoresist available in different viscosities allowing the easy deposition of
layers from $1\mu m$ to 2mm by means of variation of the spin coating conditions
[mic10a]. On the other hand, UC6772 is only available in an unique viscosity
[Pan09] avoiding the fabrication of microstructures with a high aspect ratio.
Consequently, thin layers of UC6772 could be deposited on the inner surfaces of
microchannels, which have been fabricated by conventional molding techniques.

According to the scope of this thesis, optical properties of the microstructures
must be considered for selecting the most efficient fabrication method. Hence,
a comparative study has also been carried out examining surface quality and
autofluorescence signal from the microstructures produced by photolithography
and molding techniques. By using these techniques, some limitations were
observed such as the autofluorescence of SU-8 and inhomogeneity of the surface
of the molded microstructures. These disadvantages are introduced as follows.

SU-8 thicknesses vs. autofluorescence

In several reports have been demonstrated that SU-8 is an interesting resist to
fabricate high-quality transparent fluidic channels with well-defined wall profile.
Nevertheless, despite the several benefits of SU-8, this photopolymer presents
a significant limitation for biological applications because SU-8 exhibits back-
ground fluorescence in the green spectral range.

As demonstrated in subsection 3.2.5, thin SU-8 layers exhibits high autoflu-
orescence intensities compared to other thin photopolymers. Here, emitted
background fluorescence from photoresist SU-8 as function of its thickness was
evaluated. To achieve that, different SU-8 thicknesses between $10\mu m$ to $60\mu m$
were deposited on PMMA GS substrate and then, emitted autofluorescence
intensity was measured using the optical detection system described in subsec-
tion 3.1.1. As depicted in figure 3.21, SU-8 exhibits background fluorescence
intensity having a direct and linear dependence on its thickness.

Based on the data derived from different SU-8 thickness measurements, the
higher the SU-8 thickness the greater background fluorescence intensity and
consequently, the lower signal-to-noise ratio. Autofluorescence generated by

SU-8 may limit its use in biosensor technology based on highly sensitive fluorescence detection. On the other hand, the emitted autofluorescence can be easily minimized as much as possible by reducing the volume of SU-8.
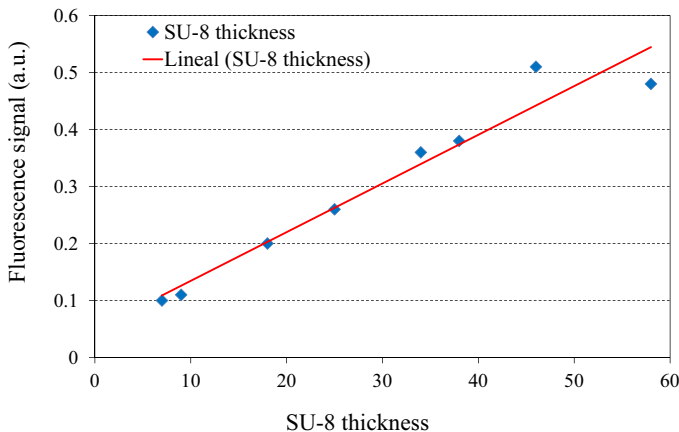
Figure 3.21: Fluorescence signal of SU-8 material with different thickness indicating a linear fluorescence intensity response [GSC+09].

Inhomogeneity of molded microfluidic devices

Background fluorescence of polymer microfluidic devices using PMMA injection molded and COC hot embossed microfluidic systems were also evaluated. Hot embossing and injection molding process are widely used for manufacturing polymer microfluidic components. Although, the mold master required for these techniques are expensive, the fabrication process is performed in short time and polymer structures can be then replicated many times, which make it attractive for mass production. Using these techniques, standard photolithography process, which is time consuming and expensive in microtechnology, can be omitted. Autofluorescence of microfluidic systems fabricated by injection molding and hot embossing process in comparison to the other polymer raw materials were evaluated and compared with raw PMMA GS material, which showed the lowest autofluorescence and best homogeneity (see subsection 3.1.1). Three different measurements were carried out on non-overlapping positions to determine the homogeneity of the materials. Table 3.7 lists all measurement results concerning the autofluorescence. Normalized measurements are shown later in figure 3.22.

Table 3.7: Background fluorescence of microfabricated systems using COC and PMMA. Fabricated microfluidic devices were acquired from thinXXS Microtechnology AG [thi10] and Fraunhofer IFAM [Fra10].

Material	Provider	Thickness [mm]	Mean [nA]	St.Dev. [nA]	Rel. Err nA/mm
PMMA GS	Josef Weiss Plastic GmbH	2	79.0	1.7	0.021
			86.2	1.6	0.018
			79.2	1.7	0.021
COC chip	thinXXS	2	334.49	3.72	0.011
			206.76	2.42	0.012
			313.23	3.13	0.010
PMMA chip	Fraunhofer IFAM	2	108.81	1.81	0.017
			75.85	1.75	0.023
			189.70	2.95	0.016

As shown in table 3.7, hot embossed COC systems exhibit high background fluorescence intensity and less homogeneity as compared to PMMA GS slides. The results also indicate that injection molded PMMA systems emit relative low background fluorescence signal, in fact similar as PMMA GS slides. However, PMMA microfluidic devices show significant variability in the measurement indicating the non-uniformity of its surface morphology.
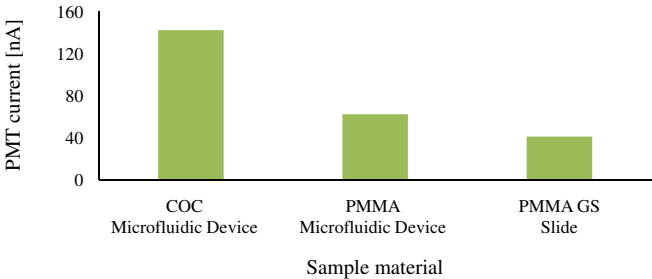
Figure 3.22: Normalized autofluorescence intensities of molded microfluidic devices. The results compared with autofluorescence emitted by PMMA GS slides.

A variety of new features could be produced in plastic material by injection molding and hot embossing technologies. In spite of that, the quality of resulting components depends on the precise manufacturing of the mold. Moreover, the quality of the molded structures is considerably influenced by the properties of the plastic material to be molded.

3.4 Autofluorescence sources

Based on the results from the last subsections, there are no materials that combine suitability for cell immobilization with excellent optical properties. All materials evaluated in this thesis exhibit background fluorescence at emission and excitation wavelengths used to detect the fluorescence intensity of labeled proteins. In order to understand these results, basic definitions concerning fluorescence signal and some potential sources of autofluorescence are described in this subsection.

Autofluorescence is the natural fluorescence of a substance, which is distributed in plants, animals and minerals. Generally, this fluorescence is generated by the presence of aromatic molecules. Thus, fluorescence can be found in substances such as proteins, coenzymes and sundry pigments. On the other hand, fluorescence in minerals is generally caused by the presence of impurities or organic materials [Ros92, Ros95]. Then, background fluorescence signal can be generated by cells or by the surfaces on which they are situated. In the most of cases, autofluorescence is an undesirable signal that overlaps with or otherwise distorts more important signals to detect. Like in the current thesis, autofluorescence can be a very disturbing factor in immunoassay systems based on fluorescence detection.

3.4.1 Fluorescent substances

Each molecule can generate fluorescence and the intensity depends on the chemical structure. Generally, the majority of organic components are fluorescent due to the presence of unsubstituted aromatic materials that exhibit strong fluorescence at ultraviolet or visible wavelengths [Ros92]. Aromatic compounds contain conjugated double bond, in which electron rotation along the aromatic ring takes places producing fluorescence light. Figure 3.23 shows the chemical structure of aromatics compounds, which generate strong fluorescent signals. Depending on the size of the conjugated material (see I, II, III, IV, V, VI, and VII of figure 3.23), so usually do the wavelength of fluorescence. For example, benzene (I) and naphthalene (II) fluoresce ultraviolet. In the case of anthracene (III), naphthacene (IV) and pentacene (V), the fluorescence is blue, green and red, respectively. In particular, fluorescein (VI) exhibits strong green fluorescence, while phenolphthalein (VII) shows weak red fluorescence. The reason of this phenomenon is due to the conjugated regions. The fluorescein molecule has a large and conjugated region, while phenolphthalein has three smaller conjugated regions which are not coplanar [Ros92].
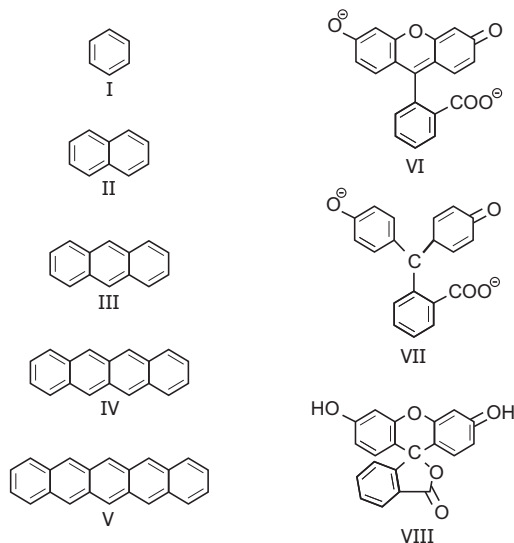
Figure 3.23: Chemical structure of several aromatics hydrocarbons as follows: benzene (I), napahthalene (II), anthracene (III), naphthacene (IV), pentacene (V), fluorescein (VI) and phenolphthalein (VII) [Ros92].

3.4.2 Environmental factors

The fluorescence of organic molecules depends also on environmental factors including ionic strength, pH, temperature, viscosity or rigidity of the medium and binding of macromolecules. PH changes affect particularly compounds such as fluorescein, which can therefore be used as pH indicators because of a marked change from strong to weak fluorescence or a change in color [Ros92].

3.4.3 Autofluorescence in optical systems

Emitted autofluorescence can also be generated from the elements implemented in the optical unit such as glass lens, filters, adhesive material used between adjacent components of multi element lens or filter or just impurities on the optical system [Ros92]. When the laser in use is a diode laser, multiple filters are required to suppress the laser emission to long wavelengths of the primary mode. The use of each filter increases consequently the background fluorescence [MF03].

Background signals from the optical system could be reduced by selecting optical components with high quality. However, background photons generated from the sample itself could not be easily eliminated. The most common case is the Rayleigh scattering coefficient at wavelength. When a molecule is excited by an absorbed photon to a higher vibration level without any electronic transition, energy is entirely conserved and a photon of the same energy is re-emitted as the molecule returns to its original state. This phenomenon is known as Rayleigh scattering [Ros92]. Rayleigh scattered photons have the same wavelength as the incident light, this is considered as elastic scattering [MF03]. This undesirable interference can be reduced by using ultraclean scratch-free substrates having the highest quality.

Another source of background fluorescence is the residual fluorescence from other impurities. This signal is directly proportional to the volume of the illuminated sample. Even if the fluorescence signal to be detected is generally weak in biosensing, unwanted impurities or molecular components, particularly in biological samples, can emit strong residual fluorescence. The reason is because many molecules of order million may be present in the illuminated volume [MF03]. To reduce this background fluorescence, the use of ultrapure solvents as well as water is required for sample preparation.

3.4.4 SU-8 autofluorescence

As explained earlier, autofluorescence is caused mainly by the chemical composition of the material. This is the case of the photoresist SU-8, which is composed of SU-8 resin and the photo acid generator (PAG). The chemical structure of SU-8, but mainly the chemical structure of PAG might be the main source in its autofluorescence. The majority of photoinitiators are aromatic carbonyl compounds, which generate fluorescence as mentioned previously. The chemical structure of PAG is shown in figure 3.24.

The photoinitiator is one of the components, which shows strong autofluorescence in the photopolymers. Fluorescent behavior of the photoinitiator has also been demonstrated by [PWS$^+$07]. In that work, several photoinitiators were tested and the results indicated that the fluorescence produced by photopolymers such as SU-8 and 1002F is associated with the use of photoinitiators. Another source of this fluorescence can be the cross linking chemistry of polymerized SU-8. During UV exposure of SU-8, PAG generates H^+-ions changing the pH.

The interaction of H^+-ions and pH change might be also the source of fluorescence in SU-8 [Voi10]. According to that reference, the intensity of SU-8 autofluorescence depends on the excitation wavelength and intensity of the excitation light.
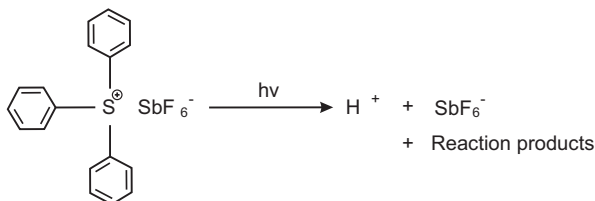
Figure 3.24: Chemical structure of PAG provided by micro resist technology [Voi10].

SU-8 autofluorescence might increase when the excitation wavelength decreases from 632 to 325nm and when the intensity of light increases. An additional factor that might affect the fluorescence intensity of SU-8 might be given by the temperature during the fabrication process. In this process, SU-8 must be baked in temperatures from 65°C to 80°C in order to evaporate the solvent and densify SU-8 structures (see Chapter 5). Hence, temperature including baking times might influence strongly SU-8 autofluorescence.

Despite the many factors that influence SU-8 autofluorescence, there is a common technique that might be applied to reduce this unwanted signal. This is the quenching method, which can be a good alternative for reducing the fluorescence as minimum as possible. According to [Voi10], dynamic quenching could be used for minimizing fluorescence in SU-8. Dynamic quenching, also known as purely collisional quenching, involves a collision between the excited energy of the fluorophore and the quencher removing excitation energy into heat instead of emitted light. Hence, quenching performance depends on how fast the quenchers can diffuse through the sample and collide with the fluorophore. The main disadvantage of the quenching method is the concentration required of quencher molecules. Thus, the quenching efficiency depends on the concentration as follows: the higher the quencher concentration, the greater their contribution to reduce the fluorescence. For improving quenching efficiency, the fluorophore and quencher molecules must also be in close physical proximity being $\leq$ 10nm [Gmb]. Due to the high price of quencher molecules and necessary conditions for the efficiency, the use of quencher molecule is limited in the current thesis.

3.5 Results and discussion

As experimentally demonstrated in previous sections, all biocompatible polymers and substrate materials tested in this thesis exhibit autofluorescence by itself and this is mainly due to their aromatic composition. Because the acquisition of materials with non-fluorescent behavior was limited, the selection of materials in this dissertation was based mainly on their homogeneity and biocompatibility.

In the case of the substrate material, the polymer material PMMA GS has been selected to be the initial substrate material for preparing and testing biocompatible surfaces. This selection was primarily based on measurements performed by the optical detection system, which indicated that PMMA GS is the best material to be used as substrate material due to its uniformity and very low background fluorescence compared to the other polymer materials.

In this chapter, the photopolymer material for cell immobilization was also selected. UC6772 and SU-8 have been selected because of the presence of epoxy groups, which provide discrete sites for immobilization of cognitive agents including proteins, antibodies and antigens. Besides the biocompatibility, the material for cell immobilization should show low background fluorescence intensity and have excellent properties to fabricate microstructures with high aspect ratio. Although UC6772 exhibits an extremely low background fluorescence compared to SU-8, its use was limited in the scope of this thesis. This limitation is caused by the fact that UC6772 is only available in low viscosities ranging between 200 and 400mPas [Pan09] avoiding the fabrication of microchannels with high resolution. Moreover, UC6772 implies the use of molded microstructures, which exhibit high background fluorescence and also inhomogeneity.

In accordance with these observations and since SU-8 has great potential for cell immobilization and fabrication of high aspect ratio microstructures, photoresist SU-8 has been selected as material for the microchannels in this dissertation.

Chapter 4

Microfluidic Devices for Heterogeneous Immunoassay

The present chapter addresses the design and simulation of different channels structures in order to examine how changes within the microchannel geometry can affect the flow profile and thereby, the behavior of biomolecules along a microchannel. For this purpose, three different geometries of microchannels were designed and subsequently simulated using the software Comsol Multiphysics 4.2. The interaction of the biomolecules was then estimated on basis of the results obtained from the simulations. An optimal microfluidic structure for the biosensor system was determined by simulation results, which were mainly focused on the pressure distributing, flow resistance and flow velocity distribution within the microchannels.

4.1 Working principle

Since the concept of micro total analysis system (μTAS) appeared, the development of microfluidic devices and their application have increased enormously. Microfluidic systems can be utilized to obtain a variety of interesting measurements, which are very useful for high throughput biomedical analysis. For example, particle size estimation, particle separation, cell collection, manipulation and cell detection are some of many functions that can be applied in research fields such as biology, medicine, chemistry and other biotechnologies sectors [CCLL08, RMT+05, YHH+06].

The material, shape and complexity of microfluidic devices vary according to their application. Some microfluidic systems are composed of a single channel [RMT+05], while others consist of many components such as mixers and valves [JFG+01, NW05, TL02]. In this dissertation, passive microfluidic devices have been fabricated, which use only hydrodynamic forces to orient biomolecules

in the flow stream and hence, heterogeneous immunoassay takes place. These microfluidic systems have been developed based mainly on the geometry and material of the microstructures considering the fabrication process technology for mass production. Selected materials have to provide excellent features for the fabrication of structures with high shape accuracies and biocompatibility. Likewise a low ground fluorescence and appropriateness for mass production are also important parameters, which were also considered in the selection of the materials. Further, a geometric design is needed to be found, which provides the required flow velocity homogeneity. The geometry and material of the microstructures are introduced in the following subsections.

4.1.1 Material of the microstructures

Immunoassay represents a powerful tool for bioanalytical systems that permits specific, rapid and sensible detection of the antibody-antigen interaction. In immunoassay applications, the selection of the support material is an important issue because it directly determines the stability of antibody-antigen adhesion. In Chapter 3, the photopolymer SU-8 was selected for the fabrication of the microstructures, because it provides excellent features to create highly precise structures with vertical sidewall profiles. Besides the excellent properties of the SU-8 to fabricate accurate microfluidic systems, this photopolymer is compatible to biosamples as demonstrated by [BKJ$^+$08] and also shown in this dissertation (see subsection 3.2.6). This biocompatibility of SU-8 allows the development of immunoassay systems directly onto its surface. It supports the possibility to immobilize microorganisms within a microfluidic device, in which the microchannels are composed of SU-8. Based on this concept, bioparticles (e.g. specific antibodies) can be fixed on the SU-8 microstructures. Figures 4.1 and 4.2 show a schematic concept of this working principle. Required reagents are introduced by way of pressure driven flow into the channel.
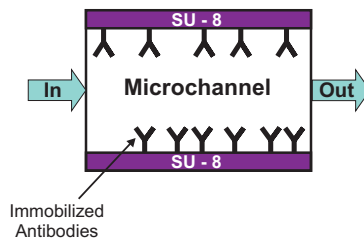
Figure 4.1: Schematic representation of the microchannel made out of SU-8, on which specific antibodies are immobilized.
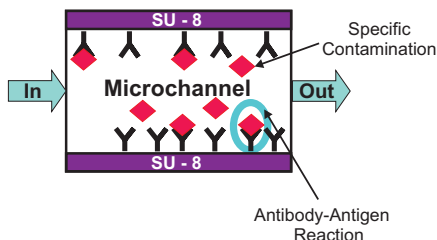
Figure 4.2: Schematic representation of the microchannel made out of SU-8, on which antibody-antigen reactions takes place [GSK+09].

When a contaminated fluid is then introduced by way of pressure driven flow, antigens that are flowing through the microfluidic system, bind to the immobilized antibodies onto the SU-8 surface. The surface of the microchannel provides an innovative tool for detecting antibody-antigen reactions, without requiring complicated and sophisticated instruments and several hours for sample preparation before the users can visualize the results. In the current thesis, passive microfluidic devices are fabricated by using SU-8 as the unique component of the microstructures, which offers the advantage of being able to biologically active all inner surfaces. Consequently, a significant number of antibodies and corresponding antigens might be immobilized on all sides of the microchannels.

4.1.2 Microchannel geometry

Microchannel geometry plays an important role in controlling cell immobilization. Channel geometry in conjunction with pressure drop governs the flow profile as well as the behavior of the contaminant biomolecules within passive microfluidic systems [GKA+09, HGL07, TL02]. The main requirement to design microfluidic devices for heterogeneous immunoassay is that the microchannel provides a flow profile with homogeneous flow velocity, thus ensuring an uniform distribution of bioparticles along the microfluidic channel. Based on this requirement, this thesis provides an analysis of the flow effect using three different shapes of microchannels. Flow behavior was also analyzed under different aspect ratios being the proportional relationship between the width and height of the channel (W/H). The results obtained from numerical simulation and corresponding experimental results have been used to find out a proper layout design for the current immunoassay procedure.

4.2 Hypothesis of particles trajectory associated with the flow profile

In microfluidic applications, Reynolds number is low and consequently, the flow becomes laminar. This is demonstrated in further analysis (see section 4.3.1). Since the flow is laminar, trajectories of the particles coincide with the direction of the streamlines as numerically and experimentally demonstrated by [XL06, AJJ+09]. So, the convective transport provides no mass production perpendicular to the flow direction. Hence, particles from the center of a channel can only reach the surface by means of the diffusive transport, which is relative low. The probability, if a particle enters the channel more likely in the center or closer to the wall is mainly influenced by the flow velocity profile within the channel. Therefore, the flow velocity profile was analyzed based on the effect of height and microchannel shape. As the size of the particle to be detected is very small and the concentration of the bioparticles is so low, like in the current dissertation, it can be assumed that the flow behavior might not be disturbed by the presence of the bioparticles. The particle-free fluid flow is then governed by the continuity-hypothesis, momentum- and diffusion equations.

4.2.1 Parallel straight microchannels

Straight microchannels are the most common configuration in microfluidic systems, in which the lenght and width are much bigger than the height of the channel. Consequently, the majority of particle-wall interactions take place at bottom and ceiling. The first microfluidic device developed in this thesis is composed of eight parallel straight microchannels (see figure 4.9). Figure 4.3 is a schematic representation of the trajectory of the biomolecules through a straight microchannel.

The streamlines are parallel to the channel length considering laminar flow in these rectangular channels. The velocity profile is nearly parabolic as shown previously in figure 2.10. The maximum velocity is given in the middle of the channel and the velocity is zero at the wall. The biomolecules initially located at the center of the channel require the longest time to diffuse to the wall. Based on the flow profile and expected trajectory of the biomolecules, a large amount of biomolecules flow at the center of the channel mainly due to the high velocities in this region. Nevertheless, the biomolecules are distributed evenly at the entrance of the channel.
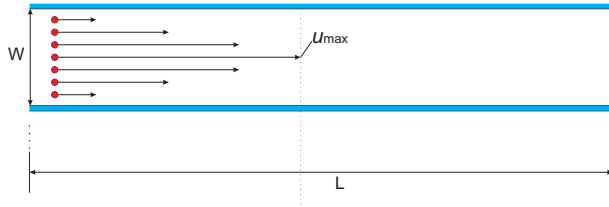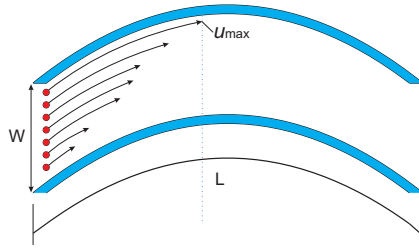
Figure 4.3: Schematic representation of the biomolecule distribution along the parallel microchannels. The red circles represent the biomolecules. Bioparticle concentration is considered to be uniformly dispersed across the entrance section. In accordance with the ballistic random walk method (BRW), microparticles show similar trajectories as well as the flow streams. Particle trajectory could be slightly modified by the effect of Brownian motion [BS10]. BRW method is not described in this thesis.

4.2.2 Meander shaped channel structures

Another common geometry used in microfluidic applications is the meander shaped channel. Depending on the velocity, the fluid is transported from the inner toward the outer wall, thus increasing the contact between the bioparticles and the surface of the channel. This effect is explained by centrifugal force as described in [SU06]. In that study, micromixing effect could be enhanced by introducing curvature and modifying the channel width. Under appropriated conditions (Re number and respectively De number), flow traveling in curved channel may be disrupted yielding chaotic particle trajectories [SU06], thus providing the contact between the particles and the wall of the curved channel. Based on that, the second microfluidic structure selected for the current thesis is a meander shaped channel design with five channels, which are parallel aligned as illustrated in figures 4.4 and 4.10.

By using the meander channel structure, diffusive transport is caused by the centrifugal effect [SU06] and consequently, the contact between the bioparticles and walls of the channels increases. Figure 4.4 depicts the schematic representation of the trajectory of the biomolecules along the meander shaped channel structure. The majority of the particles might flow near to the outer wall because of the centrifugal force as represented in this figure.

Figure 4.4: Schematic representation of the biomolecule distribution along a meander microchannel. The red circles represent the biomolecules. Bioparticle concentration is considered to be uniform across the entrance section. Under appropriated conditions (Re number and respectively De number), flow traveling in curved channel may be disrupted yielding chaotic particle trajectories [SU06], thus providing the contact between the particles and the wall of the curved channel.

4.2.3 Channel with structured columns

Obstacles within a microchannel are very useful feature in microfluidic systems. They reduce the diffusion path, homogenize the fluid and thus promote biochemical reactions on surfaces such as antigen-antibody recognition and protein interaction [BS10]. In Reference [WIHM02], cylindrical obstacles or columns have been placed in a microchannel to improve the mixing effect in microfluidic systems. At low Reynolds numbers, turbulence cannot be generated by the placement of obstacles in a microchannel. However, the obstacles improve mixing performance by affecting the flow pattern altering the flow direction and thus creating lateral mass transport [WIHM02]. Based on this concept, the third microfluidic device proposed in this thesis is realized as a microchannel with structured columns as depicted in figures 4.6 and 4.11.

An interesting advantage of the columns is the presence of the stagnation point, where the fluid is divided into diverging streams when approaching a solid surface. The stagnation point is located at the center of the solid surface between the divided streamlines and the convective velocity in this zone is reduced to zero, thus only diffusion is present. Any symmetrical obstacle like a cylinder or column placed in the stream as shown in figure 4.5 produces a stagnation point next to its upstream surface. Considering this figure as an example, the fluid from the point O to X can turn neither to the right nor to the left on reaching the point X. Hence, the velocity at X is zero that is defined as stagnation point [Sta79].
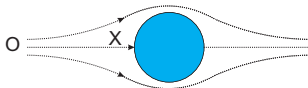
Figure 4.5: Stagnation point around a symmetrical object [Sta79]

The placement of the columns in a microchannel has a significant influence on the flow profile as well as on the trajectory of the bioparticles. A considerable amount of bioparticles are forced to flow near to the columns due to the altered flow pattern. Furthermore, the bioparticles, which have direct contact with the wall of the columns, might bind immediately to the surface due to the zero velocity in this region as explained by the stagnation point. Assuming an staggered arrangement of the columns and a parabolic velocity profile in the cross section of the entrance, small bioparticles follow a straight line until approaching the wall of the columns (see figure 4.6).
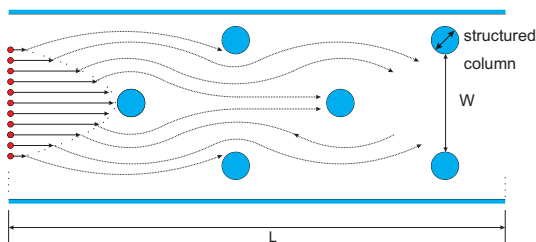
Figure 4.6: Schematic representation of the biomolecule distribution through a microchannel with placed columns. The red circles represent the biomolecules and blue circles represent the columns. An staggered arrangement of the columns is considered. Once bioparticles approach the column surfaces, bioparticles cannot continue flowing through the microchannel. Biomolecules may bind covalently to the column surface on the stagnation point, where the velocities are reduced to zero.

As observed in figure 4.6, the columns within the microchannel alter the flow direction. Thereby, fluid including the bioparticles tend to flow around to the columns area promoting the collision between desired bioparticles and the wall of the columns. A microchannel with structured columns placed inside is also used for sorting out particles and cells by Deterministic Lateral Displacement (DLD) principle. Small particles follow the streamline, whereas large bioparticles are shifted when approaching the columns [BS10]. This further increases the probability of homogenized distribution of the particles over bottom and ceiling of the microfluidic device. A parabolic flow cannot be developed, which would centralize the particle flow over the time integral.

4.3 Design of microfluidic channel structures

4.3.1 Aspect ratio

In microfluidic devices, the flow is typically considered laminar due to the low velocities and the small overall channels dimensions. In order to verify, whether the flow pattern is laminar or turbulent in the current design, the evaluation of the Reynolds number (Re) defined as the ratio of inertial forces to viscous forces was required. Using equation 2.2 Reynolds number could be calculated at different flow rates (0.6mL/min up to 3.8mL/min). Figure 4.7 depicts how aspect ratio affects Reynolds number.
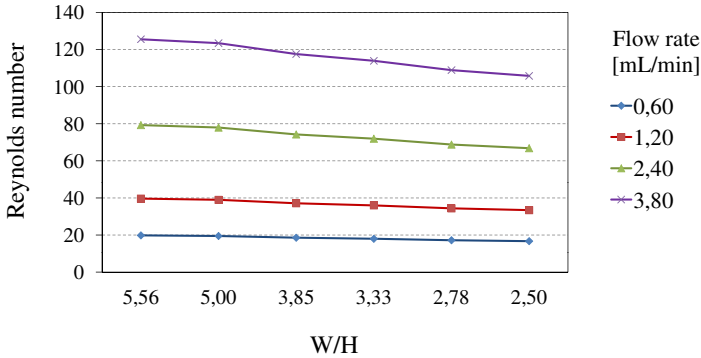
Figure 4.7: Reynolds numbers according to the microchannel cross-section at different flow rates. (W/H: width/height). First microchannels are 500μm in width, while the height range between 70μm and 210μm. Milk was considered as fluid inside the microchannel, which has a viscosity and a density of 1.76mPa·sec and 1033kg/m^3 respectively at room temperature [Fis04]

In literature, Re number up to about 2100 indicates streamline flow and values above 4000, the flow is considered as turbulent [Spu97]. Analytical calculations indicate laminar flow ($Re \ll 2100$) as given in figure 4.7. As expected, the flow becomes laminar, regardless of flow increase or decrease of the effective diameter within adequate ranges. This laminar behavior is significantly less efficient for mass transfer perpendicular to the flow direction, hence to the channel walls. The absolute dispersion of particles within the microchannels is then determined by diffusive transport.

4.3.2 Microfluidic channel design

A cross section of the flow velocity profile generated in microchannels with different shape structures should be as uniform as possible to ensure a homogeneous distribution of adherent cells. In this thesis, three different microfluidic channel geometries have been proposed with the aim to identify how the geometry affects the flow profile and thereby, the behavior of bioparticles.

A single square-shaped channel cannot fulfill this requirement, because the velocity profile in the cross section is considered to be nearly parabolic and therefore non-uniform [BS10]. Consequently, in this dissertation, microfluidic devices have been designed with multiple microchannels, which are aligned parallel and sharing the same inlet and outlet. This configuration of subchannels increases the surface and improves the velocity profile. Figure 4.8 (a) shows a single microchannel with the respective velocity flow profile. Figure 4.8 (b) depicts a microchannel separated in several subchannels. As observed in this figure, the separation of the channels influences strongly the velocity flow profile. The velocity is improved from channel (a) to (b), since the flow characteristic changed from parabolic to nearly plug-flow ensuring an uniform or constant velocity across any cross-section.

(a)

(b)
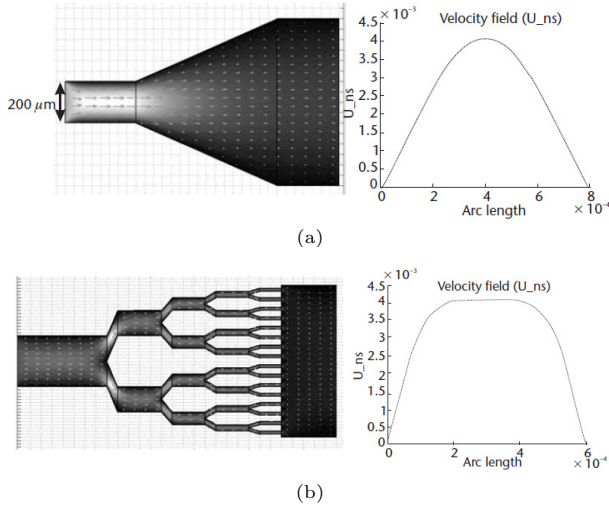
Figure 4.8: (a) Parabolic velocity flow profile along a single microchannel (b) Nearly plug-flow velocity profile along a microchannel divided into several subchannels [BS10].

Based on this concept, the fluidic structures proposed in this dissertation are based on channels divided in several subchannels and different shapes:

- Parallel straight channels

- Meander shaped channels

- Channel with repetitive staggered arrangement of columns placed perpendicular to the flow direction

These fluidic structures are shown in figures 4.9, 4.10 and 4.11 respectively. Each device consists of 3 functional sections: an inlet section, the main section for antibody immobilization/analysis and an outlet section. The in- and outlet sections have been designed identically for giving free choice to the user in connecting the device.

The parallel straight microchannels and meander shaped channel structures are composed of microchannels, which are 500μm in width. In the case of the channel with structured columns, the distance is 500μm between the columns in a row and between the rows in which column position is staggered. These microfluidic channel structures were designed on a surface of 40 x 10mm^2 enabling the parallel production of 12 units on 1 wafer with 100mm in diameter.
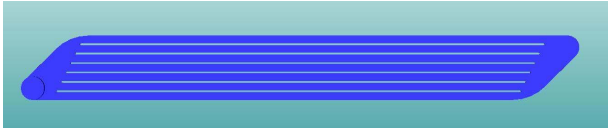
Figure 4.9: Conceptualized graphic of the microfluidic device with parallel shaped microchannels. Channels and walls are 500μm and 50μm in width respectively.

Figure 4.10: Conceptualized graphic of the microfluidic device with meander shaped channel structures. Channels and walls are 500μm and 50μm in width respectively.
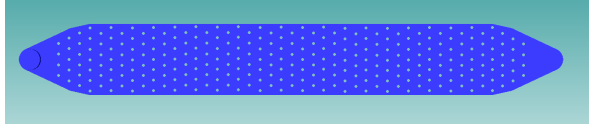
Figure 4.11: Conceptualized graphic of the microfluidic device with structured columns. The white points represent the columns in staggered arrangement, which have a diameter of 50μm. The distance between the columns is 500μm, perpendicular to the flow direction.

Besides of the channel shape, aspect ratio is another critical technical specification microfluidic devices, especially when dealing with immunoassay. The flow profile including biomolecule performance changes with the aspect ratio, even though at constant flow rates. To identify a proper aspect ratio, velocity flow profile of the proposed microfluidic structures are therefore analyzed at different channel heights: 70μm, 150μm and 210μm.

4.4 Simulation results

Computer simulations were performed using the software Comsol Multiphysics 4.2. This software can be used to design, model and simulate microfluidic structures and micro electro mechanical systems (MEMS). By means of computational fluid dynamics (CFD), the impact of local non-uniformity of the velocity profile can be examined in each microfluidic structure. To initialize the simulation using CFD solvers, boundary conditions were defined.

For the simulations run in this thesis, a fluid through a rectangular microchannel was considered. Then, the boundary conditions were set as laminar, steady state, incompressible and mono-phase fluid with constant properties. Milk was considered as fluid having a viscosity of 1.76mPa $\cdot$ sec and a density of 1033kg/m^3 at room temperature [Fis04]. Milk was pumped through the microfluidic channels under a constant differential pressure of 500mbar. Effects of dissipation, pressure-volume work and body forces are neglected. The rarefaction effects set the slip velocity at the fluid-wall interface.

The simulations presented in this thesis are focused on the analysis of the total pressure drop and flow uniformity at the center of the microfluidic chip, i.e., between the inlet and outlet ports. Additionally, the flow velocity was investigated within individual microchannels to accurately study the effect of microchannel shape on the flow behavior. These channels were numbered

downward from the top. In the simulations presented in this thesis, flow velocities and pressure are represented by the shape of the color trajectory. Red color represents high flow velocities and pressure, while blue color shows low flow velocities and pressure.

Parallel straight microchannels

Figure 4.12 shows the distribution of pressure decrease within the microchannels at room temperature. As expected from subsection 2.3.6, pressure depends on flow direcion and section size distribution.
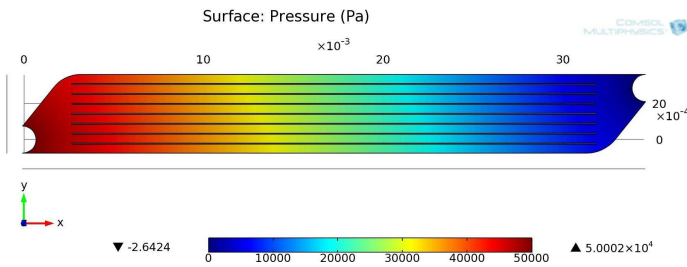
Figure 4.12: Pressure distribution along the parallel microchannels having a channel height of 70μm.

Pressure decreases gradually from the inlet to the outlet of the microfluidic system as shown in figure 4.12. It can be seen that all parallel channels are evenly affected by the pressure. Any channel has a higher or lower pressure loss than the others. The only difference between them is the starting pressure, which decreases slightly with the distance to the inlet. But the closest channel to the inlet is the farthest from the outlet, which creates the same pressure drop and an uniform pressure gradient within all channels. This simulation result shows that the optimization of the in- and outlet has been successful with regards to an even pressure distribution.

The resulting flow velocity within this microfluidic device is illustrated in figure 4.13 and represented by the shape of the color trajectory. The inlet shows a velocity gradient due to the broadening of the channel width and diameter respectively. This behavior is expected due to the incompressibility of the fluid. The distribution of the gradient around the inlet slightly differs from the velocity gradient in the outlet section. Nevertheless, the velocity within the channels does not seem to differ from channel to channel, which is also proofed by further results.

At the in- and outlet sections of the device, the velocity is higher than in the rest of the device. That is expected, due to the increased area in the middle of the fluidic device being the main section. The in- and outlet area are approximately three times less than the rest area of the fluidic device, thus reducing the velocity considerably. The design of parallel straight microchannels generates uniform velocity fields within a large area as shown in figure 4.13. As observed in this figure, the velocity along all microchannels does not have any relevant modification within the main section of the device. Nevertheless, the flow velocity needs to be analyzed in more detail to confirm the flow homogeneity. Therefore, the effect of different aspect ratios on average velocity was also analyzed by means of simulation results.
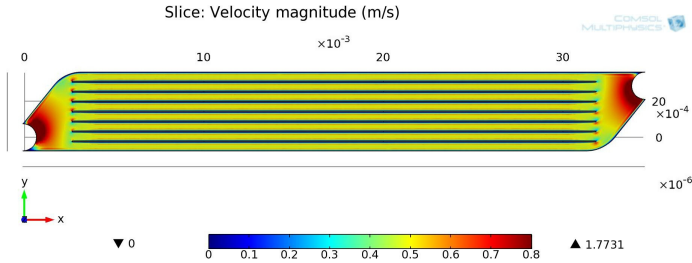
Figure 4.13: Flow velocity distribution within parallel straight microchannels with channel height of 70μm.

For this purpose, the flow velocity was examined within each individual microchannel, hence these channels were numbered downward from the top. Flow profiles of all channels were measured in the middle of the fluidic device. After that, resulting flow velocity profiles were compared. The effect of different aspect ratios on average velocity and velocity distribution are illustrated in figure 4.14. The graphs observed on the left side of this figure show the velocity field profile of one exemplary channel in the main section. These graphs also display the cross section in the middle plane in x axis of each channel, wherein the flow velocity profile was examined (red line). Additionally to that, the graphs observed on the right side of figure 4.14 depict the velocity profiles of all eight channels of the system in this cross section.

Figure 4.14 shows resulting flow velocity profiles within parallel straight channels having different heights but identical width being 500μm: figures (a)(b) correspond to channels with 70μm (b)(c) to 150μm and (c)(d) to 210μm in height. It can be seen how the aspect ratio forms a concave to a convex shaped profile.

(a)

(b)

(c)

(d)

(e)

(f)
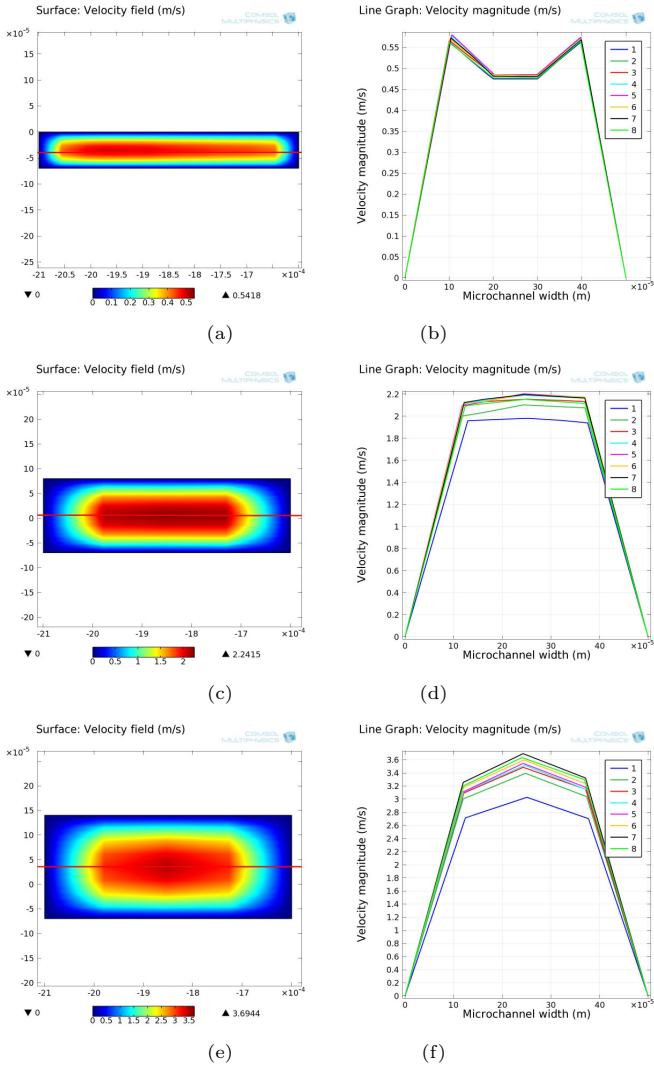
Figure 4.14: Parallel straight microchannels: flow velocity profile of microchannels with different heights (a)(b) 70μm, (c)(d) 150μm and (e)(f) 210μm. Left side: velocity field profile of one exemplary microchannel. Right side: comparison of the flow velocity along x-axis cross section of all microchannels of a microfluidic system in the main section.

In figure 4.14, the different values of velocity magnitude as a function of the channel width are compared. The microfluidic device with 150μm height shows a flow profile similar to plug-flow indicating an uniform and constant velocity magnitude along the channel (see velocity magnitude between 120μm - 380μm in x-direction in figure 4.14 (d)). Further, it can be seen how similar the flow behavior develops in each channel of one microfluidic device.

Simulation results are consistent with the general observation that flow rate decreases when approaching the channel wall, while flow rate increases when approaching the center of the channel. Interestingly, simulation results demonstrate that microchannels with 150μm in height and 500μm in width at a constant differential pressure of 500mbar leads to a trapeze shaped flow graph in the vertical middle of the channel (see figure 4.14 (d)). This distribution can be observed along all microchannels within this fluidic system in the main section. This flow profile was also observed in other simulations with lower differential pressure.

Accordingly, this design ensures that most of the cells are subject to an uniform velocity. In this area of equal velocity besides the convective transport, particles can move freely by Brownian motion and diffusion without being affected by shear stress. Hence, the immobilization of molecules within straight parallel channels with 150μm in height and 500μm in width is expected to be homogeneous. The microfluidic devices with 210μm in height and 500μm in width are not optimal for the current application. In this fluidic system, many cells are forced to move in the center of the channel because of the parabolic flow profile, thus limiting the contact between the cells and activated walls.

Meander shaped channel structures

Figure 4.15 illustrates the pressure gradient within a microfluidic device with meander shaped channels. As observed in this figure, the initial pressure decreases slightly, when approaching the outlet of the microfluidic system. In this design, an uniform pressure gradient is generated within all channels like observed in the simulation results of the parallel straight channels.

On the other hand, the velocity flow profile in this design is totally different from all the previous results observed in the simulations results of parallel straight channels. The velocity field profile of the meander shaped channel structures is shown in figure 4.16.
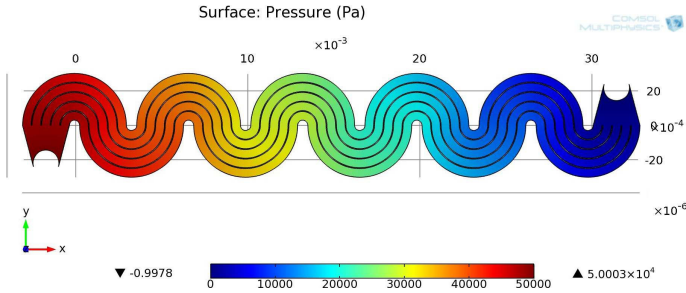
Figure 4.15: Pressure distribution along a microfluidic system with meander shaped channel structures with 70μm in height.

As estimated in the hypothesis of the particle trajectory (see section 4.2), the flow velocity would be higher at the outer side of the curve. But the specific simulation results show a higher velocity at the inner sides of each curve as observed in figure 4.16. So, centrifugal effect did not take place. The absence of the centrifugal force has not been further investigated in the scope of this thesis. However, the flow velocity changes markedly according to curvature radius. As the curvature radius is decreased, the low and high velocity zones become more different causing strong non-uniformity in the flow velocity profile. Similar results have been found in [GKA$^+$09].

The non-uniformity might cause collision between the moving cells and the already adhered cells, thereby removing them from their catching cells on the activated surface. On the other hand, the presence of low velocity on the curve implies low shear stress areas expecting the binding of a large number of molecules.
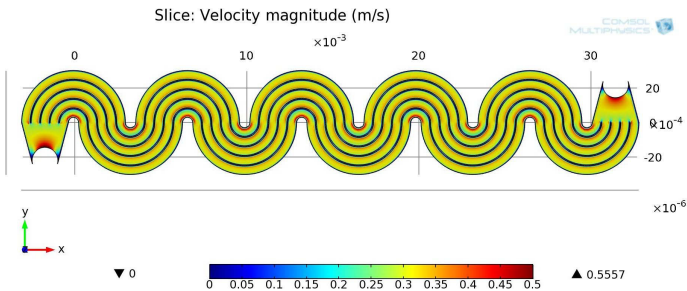
Figure 4.16: Flow velocity distribution within a microfluidic system with meander shaped channel structures with 70μm in height.

To get a better impression of this non-uniform flow velocity distribution, the individual velocity profiles of each channel were examined. The central left curve (in flow direction) in figure 4.16 was chosen as representative examination area. Therefore, the channels were also numbered downward from the top. Resulting flow profiles were measured in the middle of the system and then compared. The effect of different aspect ratios and channel shape is depicted in figure 4.17. This figure shows resulting flow velocity profiles within meander shaped channel having different height but identical width being 500μm: figures (a)(b) correspond to channels with 70μm (b)(c) to $150\mu$m and (c)(d) to 210μm in height. The graphs on the left side of figure 4.17 show the velocity field profile of one exemplary meander channel in the main section. The cross section (x axis) is also shown, wherein the flow velocity profile was examined. Velocity profiles of all five channels of the system are also illustrated on the right side of this figure. It can be observed, how the velocity at the inner side of the curve is increased and decreased in the outer curve. The velocity decreases to zero at the channel wall due to the boundary conditions.

Interestingly, the velocity flow profiles of different channels are very similar to each other. The strongest deviation of the profile of one channel towards the others are given by channel 1 within the design with a channel height of 70μm (compare figures 4.16 and 4.17 (b)) and channel 5 (the outer channel) within the design with a channel height of 210μm (see figure 4.17 (f)). The design with a channel height of 150μm is again the design with the most even conditions because the deviation between the channels are very low. The flow with the highest velocity magnitude at the inner curve ends with the curve of the channel. Then, e.g. after a left curve, as examined in figure 4.17, a right curve follows. The flow profile is swapped and realigned with its peak at the other side of the channel being the new inner-curve. Figure 4.17 shows how flows have different velocity magnitudes in the curved regions being useful for enhancing diffusive mixing as demonstrated by [SU06].

The resulting effect within curved channels is theoretically referred as Dean flow. Dean flows streams can be induced, thereby increasing diffusive transport with shorter downstream distances than in straight channel designs. The meander shaped channel structure with 150μm in height and 500μm in width shows the most homogeneous distribution concerning velocity magnitude and flow profile among all channels.

(a)

(b)

(c)

(d)

(e)

(f)
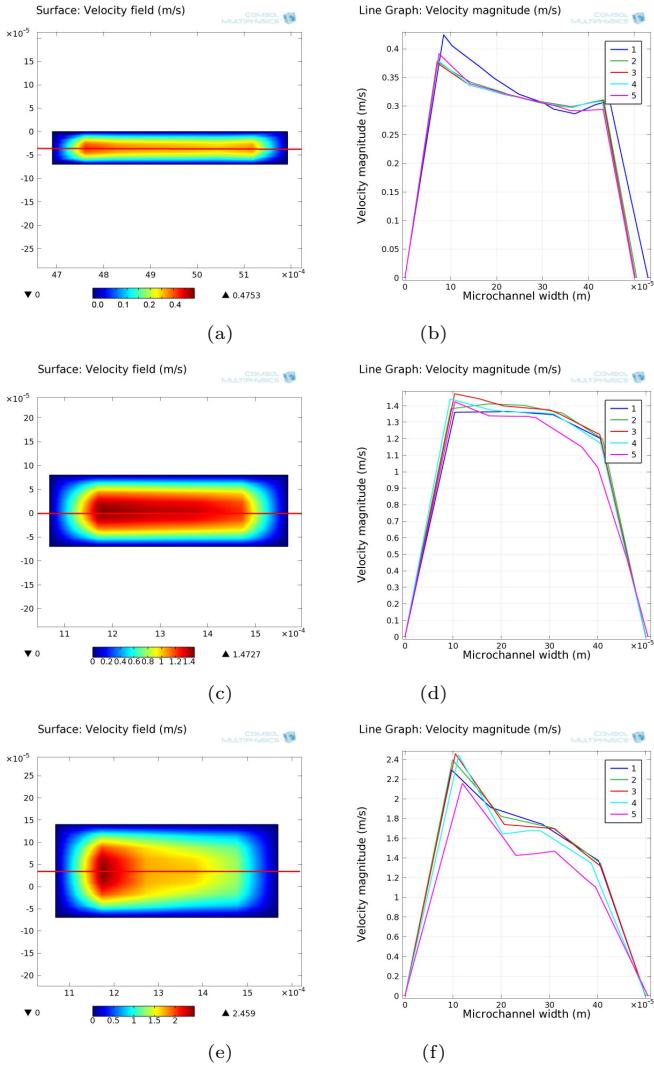
Figure 4.17: Meander shaped channels: flow velocity profile of microchannels with different heights (a)(b) 70μm, (c)(d) 150μm and (e)(f) 210μm. Left side: velocity field profile of one exemplary microchannel. Right side: comparison of the flow velocity along x-axis cross section of all microchannels of a microfluidic system in the main section.

According to the simulation results, it can be expected that a significant number of cells can be absorbed on the channel wall. Nevertheless, fluid samples cannot be examined in short times like within the straight microchannels. The maximum velocity magnitude within the straight microchannels is approximately 1.5 times higher than in the meander shaped channel structures. This assumption is also demonstrated in further simulation results, where the flow resistance of each fluidic was compared (see sections 4.4.1 and 6.1).

Channel with structured columns

The current microfluidic device contains several integrated columns in staggered arrangement, which are $50\mu m$ in diameter. Figure 4.18 shows the pressure distribution. In comparison to the already analyzed fluidic systems, the channel with structured columns presents the most homogeneous pressure distribution from the inlet to the outlet of the fluidic system.
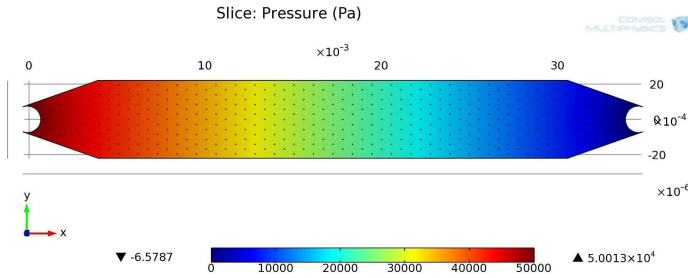
Figure 4.18: Pressure distribution along a microfluidic channel with structured columns with $70\mu m$ in height.

The pressure uniformity is caused by the symmetric position of the in- and outlet of this system and also, because of the repetitive staggered arrangement of the columns. Symmetric arrangement causes high local pressure drops, thus influencing the mixing performance [GSSM11]. The staggered arrangement provides a close contact between the fluid and activated surfaces. Although the generation of turbulence does not exist when Re is lower than 2100, the placement of staggered arranged columns in a microchannel creates complicated flow patterns. As observed in figure 4.19, flow velocities decrease in the vicinity of the columns, whereas the velocity in the rest of the channel markedly increase in x-direction. This particular flow profile influences the particle distribution, thus contributing to enhanced cell adhesion and subsequently enrichment. According to these results, a large amount of particles is expected to be immobilized around the columns assuming a homogeneous cell distribution.
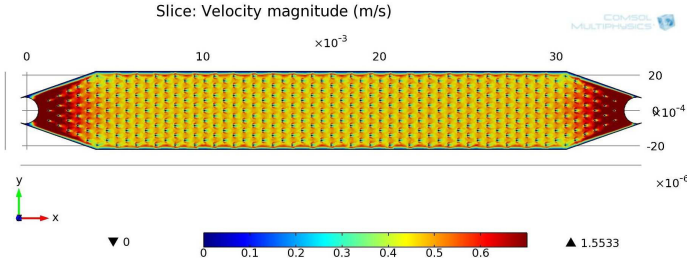
Figure 4.19: Flow velocity distribution within parallel straight microchannels with channel height of 70μm.

As performed in previous fluidic designs, the flow velocity of this channel with integrated column structures was also examined in detail, within individual microchannels. The distance between each column was defined as a channel and they were also numbered downward from the top. Flow profiles of all channels were measured in the middle of the microfluidic device. The effect of different aspect ratios on average velocity is illustrated in figure 4.20. This figure shows resulting flow velocity profiles within a microfluidic device with integrated columns structures having different heights but identical width being 500μm: figures (a)(b) correspond to devices with 70μm; (b)(c) to 150μm and (c)(d) to 210μm in height. Figures on the left side depict the velocity field profile of one exemplary channel in the main section. These figures also show the cross section in the middle plane in x axis of each channel, wherein the flow velocity profile was examined. Figures on the right side illustrate the velocity profiles of all seven channels of the system in the main section.

As observed in figure 4.20, integrated columns within a microchannel generate non-uniform flow velocity profiles. However, this fluidic design cannot be compared directly with previous fluidic designs because of it has completely different channel geometry or rather cross-section. This fluidic system consists of only one channel with integrated obstacles, i.e. columns, which may reduce the diffusion path and contribute to biochemical reactions [BS10]. Integrated columns within a microchannel in staggered arrangement improve mixing performance by affecting the flow pattern and thus, altering the flow direction [GSSM11, WIHM02]. When the main flow approaches an integrated column, the flow is split in multi narrow streams until approaching the next column. This effect takes place repetitively along all the channel. Once the flow stream approaches the columns, a significant amount of particles can be immobilized around the columns because the biomolecules mainly follow the streamlines of the laminar flow.
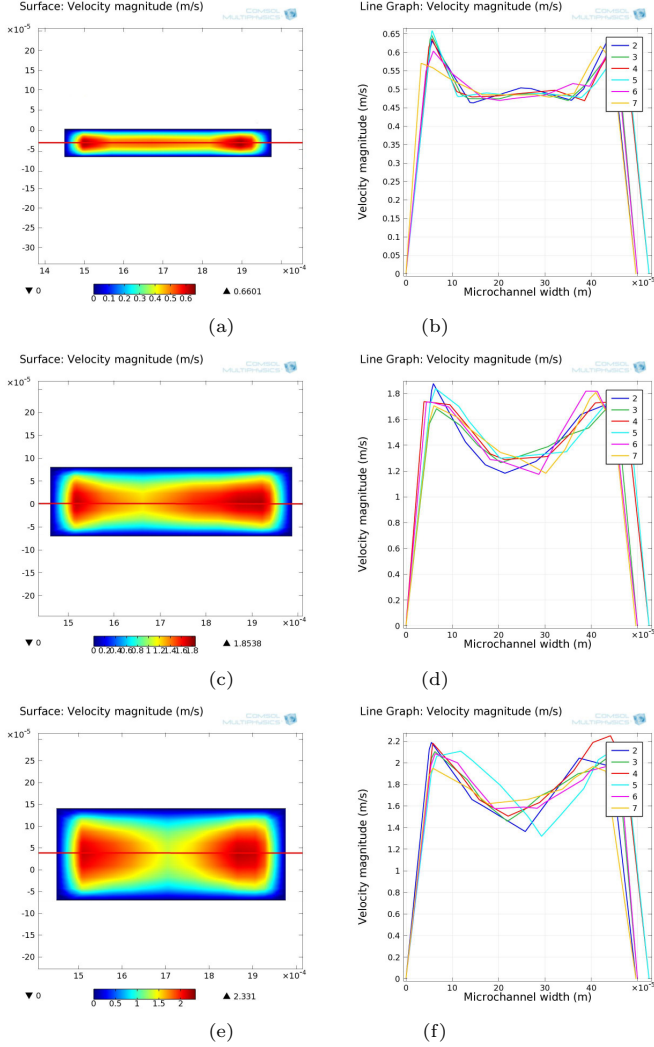
Figure 4.20: Channel with integrated columns: flow velocity profile of microchannels with different heights (a)(b) 70μm, (c)(d) 150μm and (e)(f) 210μm. Left side: velocity field profile of one exemplary gap between two structured columns (channel equivalent). Right side: comparison of the flow velocity along x-axis cross section of all channel equivalents of a microfluidic system in the main section.

4.4.1 Flow resistance

The flow resistance of all proposed microfluidic devices was also evaluated. Resulting simulation results are shown in figure 4.21. As expected, the relationship of pressure and flow rate is roughly linear (section 2.3.6). The microfluidic device with integrated columns shows the lowest flow resistance in comparison with the other channel configurations. At low flow resistance, high flow rates are generated, that is an advantage because fluid samples can be analyzed in a relatively short time.
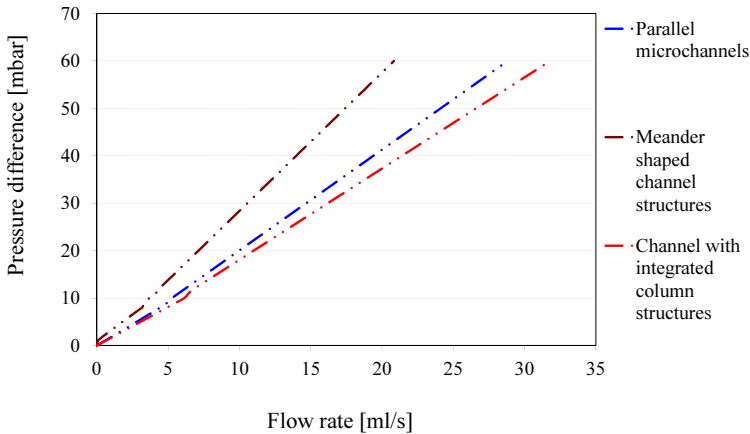
Figure 4.21: Comparison of simulation results of pressure and flow rate.

4.5 Results and discussion

In general, turbulent flows make possible that the fluid including bioparticles moves in a random manner and thereby provide contact to the surfaces. Nevertheless, on the micro scale most flows are laminar avoiding mixing effects which is indicated by low Reynolds numbers (see subsection 2.3.2). Generally, diffusion is not very effective, when microfluidic channels are over $100\mu m$ in height, especially for biomolecules with low diffusion coefficients. In that case, long channels are required to provide appropriate residual time for diffusion. However, the pressure drop is directly proportional to the length of the channel, making it difficult to drive the fluids through the channels.

In the previous sections, the influence of geometrical dimensions and shape of the distribution chambers on the velocity distribution were evaluated to find out a suitable geometry of the microchannel, so that diffusion takes place in reduced times. The flow rate and pressure drop from the simulations were used to confirm the research scope on the flow uniformity and possible diffusion trajectory of the biomolecules. Three different geometry designs of microchannels were proposed and subsequently simulated. The interaction of the molecules was estimated on basis of the results obtained from the simulations.

The simulations show that all designs cause a constant pressure drop, and that the flow is divided evenly to each channel of a microfluidic device. A closer look to the flow behavior of the different types of design revealed interesting properties of each channel structure. Therefore, a choice on just one design has been not made at this point of this thesis. Also because an homogeneous adhesion of the specific biomolecules, which was one of the main objectives of this thesis, could not be simulated. But the comparison of different aspect ratios for each design type already showed the most appropriate channel height of each design for uniform flow velocity profile.

The contours of velocity and pressure in parallel straight microchannels show that the maximum velocity appears in the center of the microchannel but the velocity near the wall is very low. On the other hand, the pressure drop is constant at any cross-section. Therefore, the conditions for cell adhesion on the activated SU-8 walls exist. An aspect ratio was also found, where the velocity profile of the simulated fluid has not the typical parabolic shape, but a similar plug-flow velocity profile. This profile is favored, because the main mass transport the channels of a microfluidic device happen in a wider area, thus increasing the probability of cell adhesion.

The contours of velocity and pressure in the meander shaped microchannels show that the maximum velocity is near to the inner wall of each curve. Based on the theory, the main velocity was expected to be near to the outer side of the curves, due to centrifugal forces. Although this effect could not be verified by the simulations, it is still expected that big molecules are driven to the outer walls of a curve due to ballistic effects. Because the diffusion path to the channel wall is shorter in the meander shaped microchannel than in straight channel design, the condition of cell adhesion also exists in this case. Cell adhesion might take place on the walls apart of the ceiling and bottom of the channels. Nevertheless, the distribution of the cells and adhesion need to be further examined.

The velocity field profile of a microfluidic device with integrated columns show that the velocity in front and behind of the structured columns is very low. Therefore, there is sufficient condition for cell immobilization to the activated SU-8 walls and columns. In this case, the structured columns are positioned in such way to ensure an even distribution of flow among the channel. Additionally, the columns promote the generation of multiple streams varying the flow velocity field and also, increasing the interaction between SU-8 walls and cells. Consequently, a significant amount of cells is expected to be immobilized on the front and behind of activated SU-8 columns.

Simulation results also show that a microfluidic device with integrated column structures has the lowest average pressure drop, respectively the highest flow rate and it is followed by the parallel microchannels. The microfluidic system with meander channel structures has the highest contacted surface causing significant friction, while the friction within the microfluidic system with integrated columns is very low. According to these results, a microfluidic device with integrated column structures is the most optimal fluidic shape for the current application. Nevertheless, the following chapters are dedicated to verify cell adhesion on SU-8 surfaces.

Chapter 5

Fabrication Process of Microfluidic Devices

Microfluidic systems can be fabricated using diverse materials including metals, glass, silicon, polymer, plastic, elastomeric materials, quartz, ceramic, or any combination of the aforementioned. In Chapter 3, several polymeric materials were evaluated regarding biocompatibility, background fluorescence and homogeneity. Based on these results, this chapter presents a detailed description of the fabrication process technology, in which SU-8 photoresist was used as structural and adhesive material, whereas materials such as glass, silicon and polymethylmethacrylate were used as substrate material for microfluidic devices.

5.1 Selection of suitable materials

The selection of the materials including substrate and coating material is the most important factor related with the fabrication process. Besides the suitability for the fabrication, these materials must fulfill the following requirements:

- Substrate materials
    - Transparent substrate materials are required. The transparency makes possible the visualization and thus, an optical evaluation of the reagents within the channels.
    - In order to fabricate disposable microfluidic devices, the selected material should be acquired at low prices.
- Coating material (material of the microchannels)
    - This material should provide the necessary features like high aspect ratio imaging and vertical sidewalls to fabricate structures employed in microfluidic devices.

– Coating material must provide good biocompatibility, so that the antibodies or antigens can be immobilized densely and uniformly onto the inside surfaces of the fluidic device.

– This material should be also transparent to allow optical detection.

5.1.1 Substrate materials

For the fabrication of the microfluidic systems, materials such as silicon and glass have been selected. The selection of those conventional materials is driven by the fact that processing techniques of the silicon are well known and developed at IMSAS. Microfluidic systems based on silicon were fabricated in combination with glass, thus components or reagents flowing through the microchannels can be easily examined through the transparent glass substrate.

In the current thesis, microfluidic devices have been also fabricated using polymeric materials, which offer great advantages such as transparency, mechanical resistances, low cost and easy fabrication procedures. The polymer PMMA has been selected as substrate material, which is even the most widely used material to fabricate microfluidic devices, especially among commercial manufactures [BL02]. Additionally, PMMA exhibits the lowest autofluorescence levels compared to other polymeric materials as shown in Chapter 3. In that chapter, different PMMA types were also examined with regard to their autofluorescence and homogeneity. The results indicated that PMMA GS is the most appropriate material to be used as substrate material. For this reason, PMMA GS was selected as an attractive alternative for the fabrication of microfluidic systems. The fabrication process using glass, silicon and PMMA GS material as substrate material is described in sections 5.2 and 5.3 respectively.

5.1.2 Material of the microchannels

In section 3.2.6, epoxy polymers such as UC6772 and SU-8 were identified as the most suitable materials for cell immobilization. Specific biomolecules (Anti-Mecoprop AB) can be fixed directly on these epoxy surfaces showing a strong covalent immobilization. Although these epoxy materials are suitable for cell binding, they show some disadvantages as verified in section 3.3.2. These disadvantages must then be considered in the fabrication process of microfluidic devices. SU-8 shows high background fluorescence limiting the sensitivity of the detection, because this autofluorescence might overlap the fluorescence signal emitted by labeled proteins.

In the case of UC6772, the limitation is related to the fabrication procedure. The properties of this material hinder the fabrication of structures with high aspect ratio. UC6772 is only available in one viscosity enabling the deposition of thin layers. Additionally, multilayer process cannot be used because UC6772 polymerizes thermally but only after exposure to UV light.

SU-8 photoresist was consequently selected for manufacturing of microstructures due to its several advantages and benefits over already tested polymer (see more details in section 3.2). SU-8 has excellent characteristics to form microstructures due to its high aspect ratio with almost vertical sidewalls and its chemical stability. In addition to that, SU-8 can be also used as adhesive layer as demonstrated by [TF05, GSK$^+$09]. In order to pattern microfluidic structures on the photoresist, standard photolithography process can be used as described in the following paragraphs.

SU-8 photolithography process

In the past few years, SU-8 has been widely used in MEMS field and is becoming the preferred resist for high aspect ratio micromachining. SU-8 is also a suited material for the fabrication of microchannels because of its high thermal and chemical stability against several acids and bases. This photopolymer is produced by Microchem in different viscosities allowing the fabrication of structures with thickness from 1μm to 2mm [LTK05], which depend on the dispensed volume, viscosity and SU-8 coating process. The process parameter can be found from manufacturer's specifications.

SU-8 microstructures were built on the substrate material using conventional photolithography process, which consists basically of the following steps: wafer preparation, photoresist coating, soft baking (SB), exposing to UV light, post exposure baking (PEB) and developing [Mic10b]. Each of these steps are detailed below.

1. Wafer preparation

   - Contaminants are removed from the wafer surface.

   - The wafer is then dehydrated on the hot plate or in the oven.

2. Photoresist coating

   - Spin speed and time are determined in accordance to desired film thickness.

- Photoresist is deposited on the wafer. Photoresist should be applied on the substrate at one to avoid the formation of air bubbles, which could decrease feature quality. Recommended amount is 1mL of SU-8 per inch of substrate diameter.

3. Soft baking

   - Soft bake temperature is determined.

   - A hot plate or oven can be used to perform the softbake process. This process is required to evaporate the solvent and densify SU-8 layer.

   - Ramping softbake temperature is recommended, which results in better film quality and adhesion to the substrate.

4. Exposing to UV light

   - Photoresist is exposed through the mask. The exposure dose depends on the film thickness.

5. Post exposure baking

   - Post exposure baking (PEB) temperature is defined.

   - PEB is performed either on a hot plate or in a convection oven. This process is required to selectively cross link the exposed areas of the film.

   - In order to minimize the stress of the film, a slow ramp or multiple stage contact hot plate process is recommended. Slow cooling after PEB is also recommended.

6. Developing

   - Developing time is defined. This time depends on the film thickness. One minute per 100μm approximately.

   - Coated wafer is immersed in the developer solution and agitated during the development time.

   - Wafer is removed from the developer solution and then rinsed in 2-propanol (IPA).

Once the photolithography process was completed, areas that remain protected by the mask were removed forming desired microstructures. Figure 5.1 shows fabricated SU-8 structures.
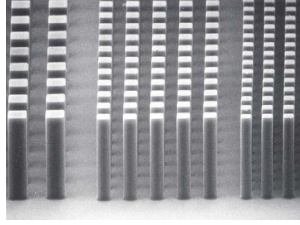
Figure 5.1: Structure with high aspect ratio using SU-8 [Mic10b]

5.2 Fabrication in silicon and glass

Silicon and glass were selected as substrate material, because processing techniques of silicon are well developed and because SU-8 provides good adhesion to both materials. Epoxy polymers (SU-8 2 and SU-8 3050), silicon and glass wafers were used for first experiments. In addition to that, two chrome glass masks were used to fabricate the microfluidic devices. The first mask defines inlet and outlet and the second mask defines the geometry of the microstructures that involves the width and length of the microchannels. Figure 5.2 illustrates a conceptualized design of the microfluidic system, where SU-8 is used as the unique component of the inside surfaces of the fluidic channel. Microfluidic structures were made on a glass wafer, meanwhile inlet and outlet of the microfluidic device were made on a silicon wafer. Fabrication procedures for bottom wafer (silicon) and top wafer (glass) are explained step by step and represented in figures 5.3 and 5.10 respectively.
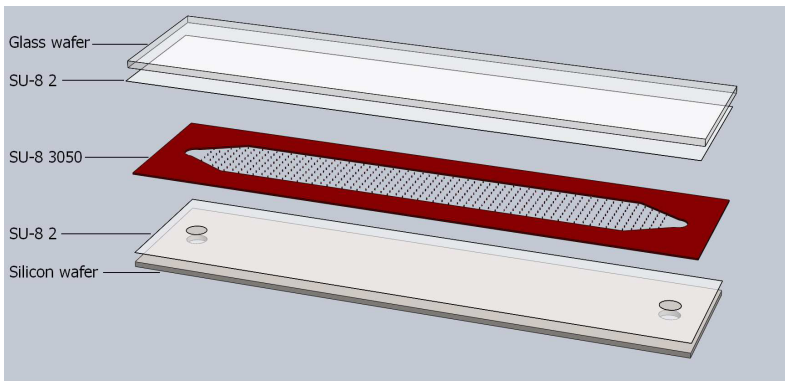
Figure 5.2: Schematic drawing of a microfluidic device. Glass and silicon wafers were used as substrate material, while SU-8 was used to create the microstructures and also used as adhesive layer [GSK+09].

5.2.1 Glass wafer processing

The process sketched in figure 5.3 describes the fabrication steps of SU-8 structures, which were implemented on a glass wafer. The adhesion of SU-8 to the wafers is an important requirement for the fabrication process. To improve it, the glass wafer was prepared immediately to prior SU-8 processing. For this purpose, Caro's acid was used to clean and thus remove organic materials from the glass substrate. Then, it was heated at 200°C for at least 45 min in an oven, thus removing water from its surface. Afterwards, a thin film of SU-8 2 was applied and coated for 30 sec at 3000 rpm on the glass wafer, resulting in a film thickness of about 3μm. This procedure was followed by a prebake for one minute at 65°C and another three minutes at 95°C on a hotplate to evaporate the solvent contained in SU-8. The wafer was unstructured exposed to UV light (flood-exposure) for 30 sec and a post expose bake was performed at 65°C for 1 min and 95°C for 1 min. The deposition of thin SU-8 film was required before thick SU-8 layers were deposited to improve the adhesion between glass substrate and SU-8 structures. Additionally, this fabrication process offers microfluidic devices where bottom, ceiling and walls of the microchannels are made completely out of SU-8 photoresist. As a result of this fabrication method, a large surface area composed of SU-8 is provided to immobilize specific biomolecules. Consequently, a large amount of contaminant particles can be collected and then analyzed through the microfluidic device.
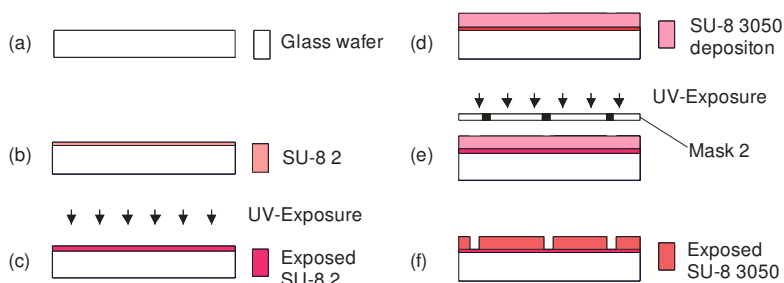
Figure 5.3: Schematic illustration of the fabrication process for SU-8 based channel structures. (a) Cleaning procedure using Caro's acid. (b) Deposition of a thin SU-8 (3μm). (c) Flood-Exposure. (d) SU-8 3050 was spin coated followed by a soft bake process to eliminate solvent components. (e) Exposure of coated SU-8 layer through the mask in which the microstructures are designed. (f) Non-exposed SU-8 areas were removed by SU-8 developer creating the microstructures.

According to the manufacturer's specification [Mic10b], the height of the structures can be defined depending on the dispensed volume, viscosity and SU-8 coating process. Microchem Corporation provides information about parameters such as viscosity, spin speed, recommended times and temperature for prebake and postbake steps and exposed time. Figure 5.4 displays film thickness vs. spin speed curve for the SU-8 3050 photoresist provided by Microchem.
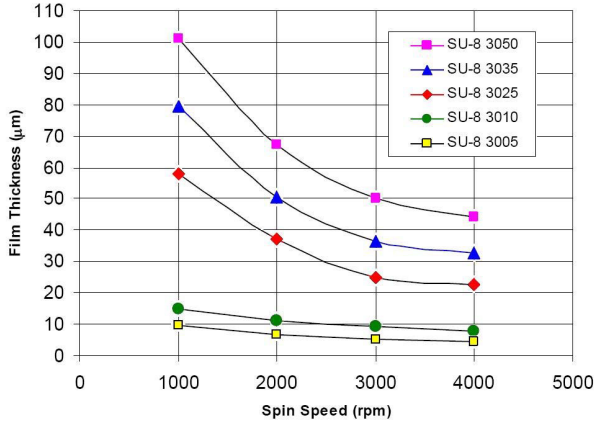
Figure 5.4: Spin speed vs. Thickness for SU-8 3000 resists [Mic10b]

For the first experiments, SU-8 3050 was coated according to the manufacture's specifications to obtain a thickness of $100\mu m$. However, resulting layer presented a thickness variation of about $30\mu m$ as shown in figure 5.5. The film at the center was thinner than that at the wafer edge. Previously published results [PHBF03] and current experimental results demonstrated that by thick layers of SU-8 (up $100\mu m$), the thickness varies significantly. This non-uniformity of the layer leads to an inappropriate contact between silicon and the glass wafers in bonding process. This variation must be controlled in the fabrication process to avoid not seal microfluidic systems.

In order to improve the homogeneity of this layer, parameters of the standard coating process were modified, in which two layers of SU-8 3050 were coated on a glass substrate as represented in figure 5.6. The first layer of SU-8 3050 was spin coated on an exposed SU-8 2 glass wafer at 1000 rmp for 30 sec, followed by soft bake at $65°C$ and $95°C$, for 5 and 15 min, respectively. When the temperature of the substrate cooled down to about room temperature, the second layer of SU-8 3050 was coated at the same spin speed as the first film.

Figure 5.5: Thickness variation of SU-8 film.

After the coating process, the baking process proceeded at 95°C for 2h within a slow ramping to reduce the internal stress of the thick SU-8 layer. Coated SU-8 films onto the glass wafer were exposed to UV light for 120 sec. In the postexposure baking step, the wafer was heated for 20 min at 95°C using a slow ramping. The development was performed by immersion of exposed structures in SU-8 developer during 7 min.
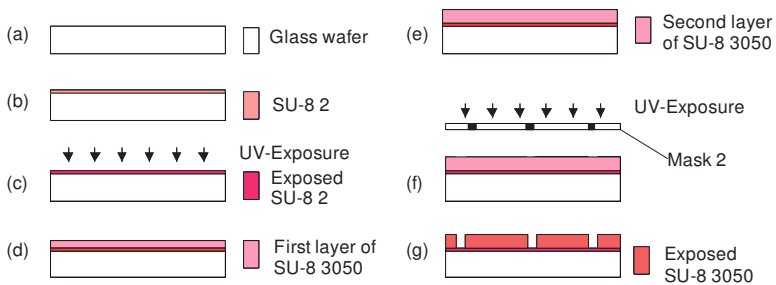
Figure 5.6: Fabrication process of SU-8 structures using multilayer deposition procedure [GSK+09] (a) Cleaning procedure using Caro's acid. (b) Deposition of a thin layer of SU-8 (3μm). (c) Flood-Exposure. (d) SU-8 3050 was spin coated followed by a soft bake process. (e) A second layer of SU-8 3050 was applied on the same glass wafer. A baking process was performed again using slow ramping. (f) Exposure of coated SU-8 layer through the mask, in which the microstructures were designed. (g) Non-exposed SU-8 areas were removed by SU-8 developer.
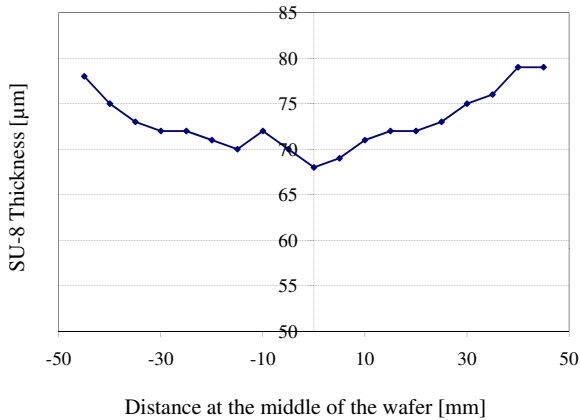
Figure 5.7 depicts the thickness variation of a thick SU-8 layer generated by means of the multilayer deposition process. This technique enables the fabrication of SU-8 layers with less thickness variation and good uniformity in the wafer edge region as compared to the original fabrication process. Depth and homogeneity of resulting SU-8 microstructures can be observed in figure 5.8.
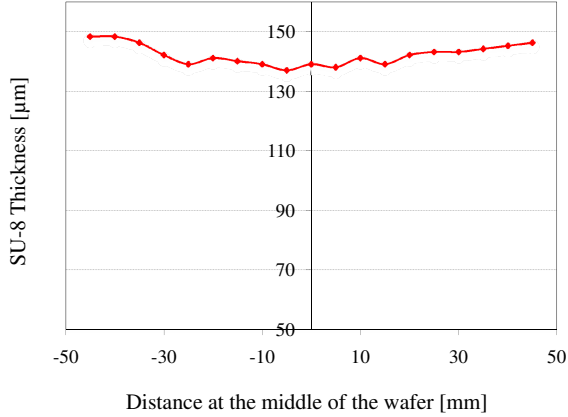
Figure 5.7: Thickness variation of SU-8 film using multilayer deposition procedure.
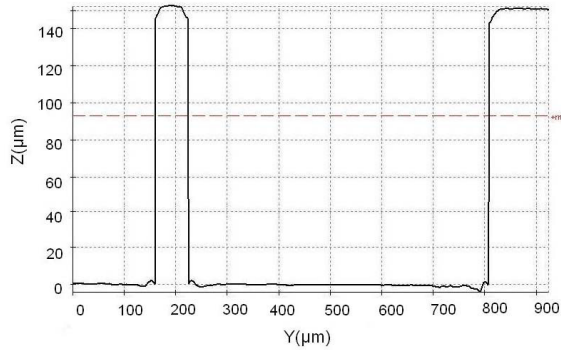
Figure 5.8: Cross-sectional view of the microfluidic structure. Microstructures of approx. 150µm height could be obtained by the multilayer process.

With the use of 3D-topography (see figure 5.9), it was possible to extract a more accurate representation of the uniformity of the SU-8 structures. The homogeneity of the structures could be verified at various locations within the microchannel.
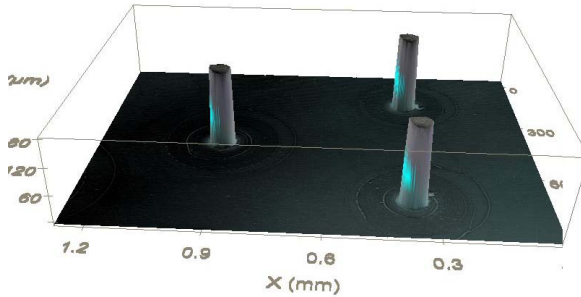
Figure 5.9: 3D-topography of a microchannel with integrated columns.

In accordance with the results, microstructures higher than 100µm could be achieved and thickness variation of SU-8 thick layer could be reduced to 10µm by using the multilayer process. The improvement of the uniformity of SU-8 film thicknesses leads to an optimal contact between SU-8 microstructures and silicon wafer, thus improving the bonding process. In this way, the possibility to produce sealed microfluidic channels increases in comparison to the standard process of SU-8 photoresist.

5.2.2 Silicon wafer processing

As mentioned earlier, the first mask defines the inlet and outlet of the microfluidic device. Basically, deep reactive ion etching (DRIE) process was used to fabricate the inlet and outlet orifices in silicon substrate. The process consists of several steps and the schematic representation is shown in figure 5.10. First, a thin aluminum layer was sputtered over the whole wafer that acts as stop-layer. Then, on the backside of the silicon wafer, positive resist was deposited and patterned by photolithography using the mask, in which inlets and outlets have been defined. Subsequently, silicon was etched to a depth of 380µm using the DRIE process to form inlet and outlet ports. After this, the etch stop-layer (aluminums) was removed using a wet etching process. The positive resist was also removed by means of solvent. Circular holes with a diameter of 1.5mm were then formed accurately and simultaneously in the silicon wafer. After removing the stop-layer and positive resist, the silicon wafer was oxidized through thermal oxidation process to get a thin and adherent layer. Next, on the same silicon substrate, a bonding layer was applied using SU-8 2 of about 10µm of thickness. At this point, this coated and unexposed silicon wafer and the glass wafer with the SU-8 microstructures were ready for bonding process to integrate the microfluidic device.
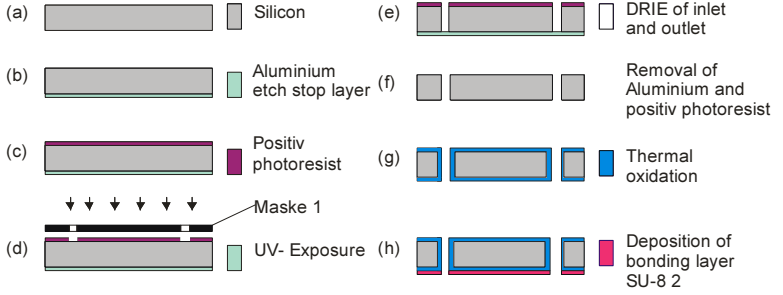
Figure 5.10: Schematic illustration of the fabrication process of the inlet and outlet. (a) Silicon wafer is used as carrier substrate. (b) Etch stop layer is deposited. (c) Positive resist is deposited on the back side of the silicon wafer. (d) Exposure of positive resist through the mask. (e) Etching of inlet and outlet by DRIE. (f) Remove positive resist and thin layer of aluminum. (g) Thermal oxidation is applied to increase adhesion properties. (h) Deposition of bonding layer (unexposed SU-8 2).

5.2.3 Bonding process

Bonding between glass and silicon substrate is well established by different bonding processes. The most common methods are anodic and silicon fusion bonding [Mad02]. However, these techniques have some disadvantages such as high temperature in the case of silicon fusion bonding and high voltage in the case of anodic bonding. In contrast to these bonding technologies, there is a simple method that uses polymers as intermediate bonding material. In this process, low temperatures and low pressures are required and bonding takes place by cross linking of an adhesive polymer layer. SU-8 being a polymer enables bonding at very low temperature as demonstrated in [JFG$^+$01, Tuo07, TF05]. In the current dissertation, bonding process parameters such as temperature and time were optimized to avoid channel filling. Within the optimized bonding process, a bonding layer with approximately 10μm of thickness was deposited on the silicon wafer. To achieve that, common coating process could not be used due to the presence of the perforations (inlets and outlets) on the silicon wafer. Then, the deposition of the adhesive layer was done by means of airbrush coating techniques. Afterwards, a prebake step was applied at $65°$C for two minutes to obtain sticky bonding surface and avoid that this adhesive layer flows toward the microchannels. The time above 2 min cures the SU-8 adhesive layer, meaning that it is not soft enough to achieve an appropriate bonding strength between the substrate materials. Next to that, wafers were inserted into the bonding chamber and brought into contact (see figure 5.11).
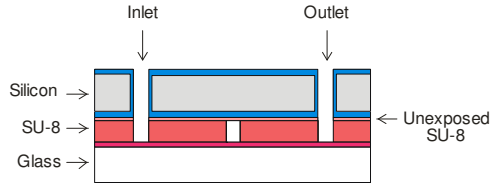
Figure 5.11: Wafer bonding process using unexposed SU-8 2 [GSK$^+$09].

By using the thin SU-8 layer, wafers were successfully bonded under vacuum conditions at a pressure of 500mbar and temperature of 60°C for 1h. Heating was realized in 3 steps in order to obtain a uniform heating ramp and thereby, reduces stress in SU-8 layers. Once the bonding procedure is finished, the exposed (microstructures) and non-exposed SU-8 layers (adhesive layer) were exposed through the glass wafer by UV light during 40 sec. Figure 5.12 shows a picture of one of the bonded wafers. Bond interface could be directly observed through the glass wafer identifying the status of sealed and unbounded areas. The resulting bond was strong enough, so that devices did not detach during the dicing process.
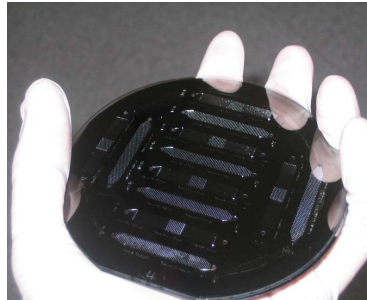
Figure 5.12: Bonded glass and silicon wafer by means of SU-8 photoresist.

5.3 Fabrication in polymers

As defined in Chapter 3, the photoresist SU-8 has been identified as suitable material to form the microstructures because of its excellent properties enabling the binding of specific biomolecules directly on its surface. Regarding to the substrate material, PMMA GS was chosen due to the low-cost manufacturing, transparency, low background fluorescence and mechanical resistance. In this section, PMMA GS and the epoxy polymers SU-8 2 and SU-8 3050 were

then used to fabricate microfluidic devices. PMMA GS material provided by Josef Weiss Plastic GmbH [Jos10] is only available with a thickness of 2mm having a variation of ± 0.3mm. PMMA GS sheet was then cut into 100mm diameter substrate to be processed in the cleanroom facilities. Prior to SU-8 processing, PMMA GS substrates must be properly treated for improving the adhesion between SU-8 and PMMA GS substrate. To achieve that, PMMA GS substrates were cleaned in a ultrasonic bath and further treated in an oxygen plasma. All fabrication steps are shown and described in more detail in the following subsections.

5.3.1 Surface treatment

As mentioned previously, before SU-8 was deposited to PMMA GS substrate, it must be cleaned to remove any contamination material from the surface. First, PMMA GS wafers were immersed for 30 min in an ultrasonic bath with sodium dodecyl sulphate (SDS), which should dissolve the organic components and does not affect the surface composition of PMMA GS. Then, PMMA GS substrates were cleaned again with deionized water and heated at 75°C for at least 60 min. Due to the low surface energy of the PMMA GS, an additional treatment step on its surface was required to improve adhesion properties with SU-8 [HBO03]. In order to evaluate cleaning performance and wettability of PMMA GS surface, contact angle method has been used. This method consists of the measurement of the angle (θ) formed between a drop of liquid and a surface. When a drop of water is placed on a surface, the drop will either bead up or spread out depending on the wettability of the surface. The contact angle is then the angle formed between the edge of the drop and the surface as shown in figure 5.13.
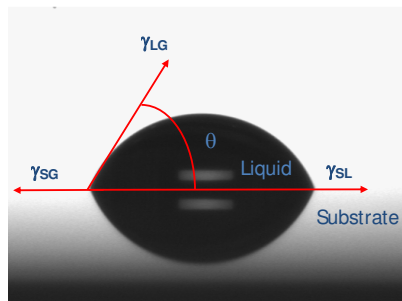
Figure 5.13: A small volume of water (4μL) placed onto an untreated PMMA GS surface forms a droplet with a contact angle of 71.38°.

The shape of the drop is determined by three forces on interfacial tension as given in figure 5.13: first force is caused by the surface tension between the solid and the gas (γ_{SG}), second force is caused by the solid liquid surface tension (γ_{SL}) and the third force is due to the surface tension between the liquid an gas phases (γ_{LG}). Thus, the contact angle provides information on the interaction energy between the surface and liquid and it can be determined by Young's equation [BS10] which is given as:

$$\gamma_{LG} \cos \theta = \gamma_{SG} - \gamma_{SL} \tag{5.1}$$

Untreated PMMA GS surface exhibited a contact angle of $71.38°$ demonstrating low hydrophilic tendencies and therefore poor adhesion to SU-8. To increase the surface energy of PMMA GS wafers, they were treated with oxygen plasma generated in a microwave plasma PS400 oven (PVA Tepla AG, 2.45GHz). This procedure generates wettable surfaces and consequently, improves the adhesion of PMMA GS with SU-8. Contact angle method was used again to characterize treated surface. To identify the effective plasma procedure, the contact angle with water on PMMA GS was measured at different plasma parameters. The evolution of the surface energy was observed for samples treated by oxygen plasma with 50W, 150W, 250W and 500W for several minutes (from 0.5 to 10 min). The results are shown in the following figure.
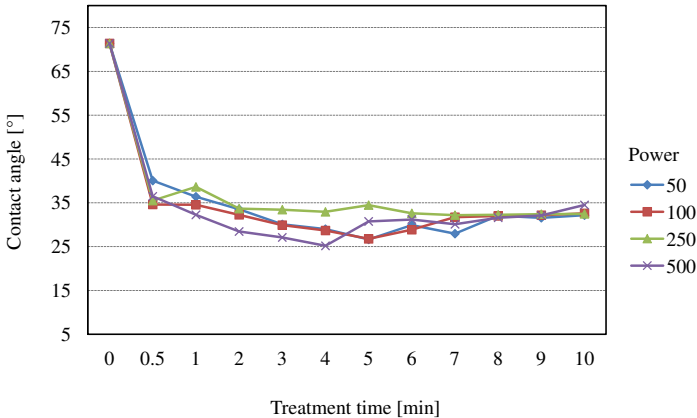
Figure 5.14: Water contact angle on PMMA GS at different plasma treatment conditions [GSF+12].

Optimal plasma parameters were selected according to the resulting contact angles of water on PMMA GS. Contact angles of less than $30°$ could be achieved

by plasma power of 500W. Significant decrease in contact angle was observed in the first 5 min at different plasma power values used in this study. Higher treatment time leads to only a slight further decrease of the angle. From the results, minimum contact angles ($28.45°$, $27.1°$ and $25.18°$) were obtained under oxygen plasma treatment between 2, 3 and 4 min at 500W respectively. In order to reduce the process time as much as possible and avoid that plasma treatment affects the surface topography of the substrate [WDZ+07, SVABC03], PMMA GS has been treated with oxygen plasma only for 2 min, at 500W. After plasma treatment, PMMA GS was coated with SU-8. The adhesion properties were then verified by using the standard method of adhesion by tape test showing good results. SU-8 thin film could be not detached from PMMA GS surface as required.

(a)   (b)
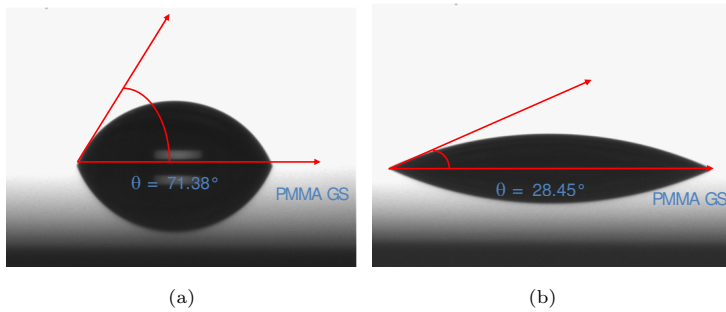
Figure 5.15: A small volume of water ($4\mu L$) place onto a PMMA GS surface (a) Contact angle of an untreated PMMA GS surface. (b) Contact angle on PMMA GS surface after plasma treatment at 500W for 2 min.

The contact angle on PMMA GS surface after plasma treatment was measured during 18 days for monitoring hydrophobicity recovery rate at clean room conditions. Contact angle increases considerably from $25°$ to approximately $45°$ after one day. Contact angle continues increasing slowly from the second day till the end of the established period in this experiment as illustrated in figure 5.16.

The contact angle measurement of PMMA GS surface during several days proved that the contact angle increases with storage at clean room conditions. The hydrophilic PMMA GS surface can be rendered hydrophobic, so that wettability decreases and thus diminishing adhesion quality between SU-8 and PMMA GS surface. For this reason, SU-8 processing should be performed immediately after plasma treatment to ensure strong bonding adhesion between the substrate and coating material.
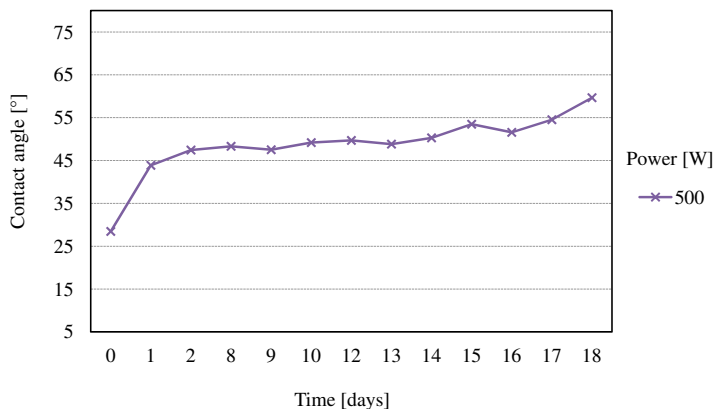
Figure 5.16: Aging of plasma treated PMMA GS substrate.

5.3.2 PMMA GS wafer processing
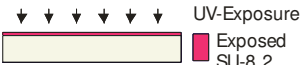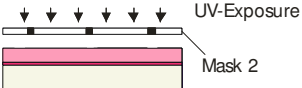
The fabrication process by means of SU-8 and PMMA GS wafers are generally based on of a photolithography process. Two PMMA GS substrates have been prepared for this purpose: on the top wafer are generated the microfluidic channel structures, which were fabricated by similar fabrication procedure as indicated in subsection 5.2.1. The second or bottom substrate was used to define the inlet and outlet of each microfluidic device. Inlet and outlet ports were easily formed by drilling avoiding additional and expensive fabrication process.

After cleaning procedure and directly after plasma treatment, SU-8 processing takes places. Processing of the top wafer starts with the deposition of a layer of SU-8 2, which improves the adhesion between SU-8 microstructures and the substrate. SU-8 2 was coated on PMMA GS wafer for 30 sec at 3000 rpm and followed by a prebake process. In contrast to glass substrate, in which prebake was performed on a hot plate, PMMA GS has been heated at relative low temperature (between 75 and 80°C) using a convection oven. PMMA GS substrates placed on a hot plate exhibited significant deformations on the surface, which may affect the bonding processing.

After SU-8 2 was cotaed on PMMA GS, it was heated in a convection oven for 20 min. Prebake was followed by UV light for 30 sec and postbake for 10 min for performing crosslinking. After that, two layers of SU-8 3050 were deposited on PMMA GS substrate at 1000 rpm for 30 sec.

The deposition of two layers was realized with the aim to improve the homogeneity of thick SU-8 layer as demonstrated in subsection 5.2.1. Fabrication process by using PMMA GS wafers and SU-8 are summarized in tables 5.1 and 5.2.

Table 5.1: The fabrication of SU-8 microstructures on PMMA GS substrate (top wafer).

Illustration of process step	Description
PMMA GS	Cleaning procedure was performed using SDS that removes any contamination. Cleaned wafer must be also treated in oxygen plasma to improve adhesion with SU-8.
SU-8 2	Deposition of a thin layer of SU-8 2 (approximately 3μm).
UV-Exposure / Exposed SU-8 2	The wafer was completely exposed. This layer improves the adhesion between SU-8 structures and PMMA GS substrate.
First layer of SU-8 3050	SU-8 3050 was coated on the PMMA GS substrated, followed by a soft bake process for 20 min using a convection oven. This step is performed to eliminate solvent components.
Second layer of SU-8 3050	A second layer of SU-8 3050 was applied on the same PMMA GS wafer. A baking process was performed again using a convection oven for 2h.
UV-Exposure / Mask 2	Coated SU-8 layers were exposed through the mask, in which the microstructures are designed.
Exposed SU-8 3050	Non-exposed SU-8 areas were removed by SU-8 developer and thus, creating the microstructures.

Table 5.2: The fabrication of inlet and outlet ports on PMMA GS substrate (bottom wafer).
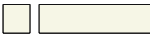
Illustration of process step	Description
PMMA GS	Cleaning procedure using sodium dodecyl sulphate (SDS) for removing any contamination.
Fluid connections via drilling	Inlet and outlet ports were defined on a second PMMA wafer.
Plasma Treatment	PMMA GS surface must be treated in plasma to improve adhesion properties with SU-8.
Deposition of bonding layer SU-8 2	A thin layer of SU-8 2 (10μm) was deposited by means of airbrush coating techniques on the second PMMA GS wafer .

Table 5.2 shows the fabrication process for the bottom wafer, on which inlet and outlet ports were defined. Due to the mechanical properties of PMMA GS, these ports with 1.5mm in diameter have been easily made by drilling. Next to that, bottom wafer was cleaned using SDS and also treated in oxygen plasma to improve adhesion properties with SU-8 (see subsection 5.3.1).

5.3.3 Bonding process

After processing, PMMA GS were ready for bonding process. PMMA GS wafers were placed in contact and aligned as given in figure 5.17. Bonding process has been performed under vacuum condition on a classic wafer bonding system. Wafers were bonded at a temperature of 65°C during 90 min and pressure of 500mbar.

Once bonding process is completed, adhesive layer was exposed through the bottom or top PMMA GS wafer during 40 sec and a post bake process was done at 75°C within 20 min in a convection oven. After the bonding process, resulting PMMA GS wafer having a total thickness of approximately 4.2mm were then cut according to the dimension of each microfluidic device.
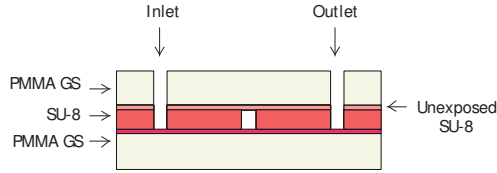
Figure 5.17: PMMA GS wafer bonding process using unexposed SU-8 2.

5.3.4 Results

The main problem usually appeared in the fabrication process was the non-uniformity of the SU-8 layers. Due to the thickness variation, some structures were not entirely in close contact during bonding process, resulting in voids of various sizes. Consequently microchannels were not sealed, which is crucial in microfluidic systems for practical applications. This problem could be reduced by applying SU-8 multilayer technology. By this multilayer technique, the relative uniformity of SU-8 films could be obtained. Figure 5.18 illustrates a cross section of a microchannel. Microchannels were successfully fabricated with dimensions of around 150μm in height, 500μm in width and wall width is 100μm. These microfluidic channel designs have been realized on a surface of 40 x 10mm^2 with inlet and outlet ports, which have a diameter of 1.5mm.
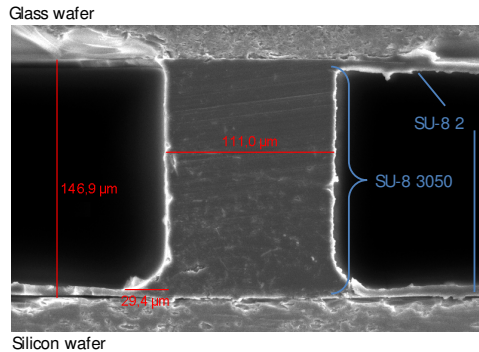
Figure 5.18: SEM showing a cross section through sealed SU-8 channels [GSK$^+$09].

Figure 5.19 shows a picture of one of several fabricated microfluidic devices using SU-8, silicon and glass wafers and fabricated microfluidic systems by using SU-8 and PMMA is shown in figure 5.20. Leak and pressure test of the sealed microchannels were performed by filling the bonded microfluidic devices with DI water. To achieve that, fabricated microfluidic devices were

interfaced through a Teflon holder, which includes two 1/4-inch side ports. These ports were connected through male barbed adaptors, acquired from Omnifit [Omn10]. After establishing connections, fluids could be pumped with standard fittings and driven by pressure through a pressure controller. During tests, air bubbles were generated into the microchannels because of the SU-8 hydrophobic surfaces. Therefore, rinsing inner sides of the fluidic chip with propanol is recommended to facilitate easier wetting between fluids and SU-8 surfaces. Afterwards, microfluidic devices were tested with DI water. It was easily pumped away from channels, showing excellent results.
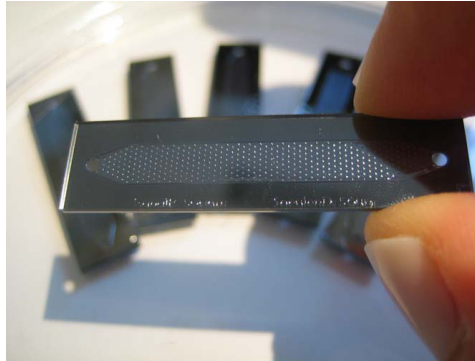
Figure 5.19: Picture showing a microfluidic device fabricated by using silicon, glass and SU-8 with dimensions of x $40x10$mm [GSK$^+$09].
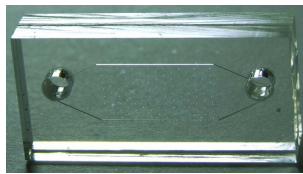
Figure 5.20: Picture showing a microfluidic device fabricated by using PMMA GS and SU-8 with dimensions of $20x10$mm.

Although the fabrication of SU-8 microstructures was optimized as maximum as possible by using the multilayer deposition method, their homogeneity must still be improved. The fabrication procedure could be again defined in which a dry film photoresist substitutes SU-8 3050. This product is called TMMF and it is chemically very close to SU-8 being biocompatible and showed a thickness variation of only $\pm1\mu$m [SVH$^+$07, MZH$^+$09]. The inhomogeneous distribution

of SU-8 3050 could be improved by using TMMF dry film. TMMF was acquired from Tokyo Ohka Kogyio (TOK) in 2008, but unfortunately it was no longer available. For this reason, further experiments by using this dry film could not be performed in the scope of this thesis.

Currently, another Dry Film is available promising similar properties as TMMF and therefore, it might also be suitable to be used for the fabrication of microstructures and also for the immobilization of biomolecules. This material is known as PerMx$^{\text{TM}}$3050 and can be acquired from micro resist technology [mic10a]. As well as TMMF, PerMx$^{\text{TM}}$3050 is an epoxy based negative photoresist and has also similar characteristics as SU-8. This dry film is suited for structuring at high aspect ratio with vertical sidewalls, high resolution and homogenous resist thickness. Additionally, this dry resist could be used for wafer bonding process making it an attractive alternative to replace SU-8. Although the fabrication of microstructures by using this dry film was not applied in this thesis because of limitation of time, it surely merits further work.

Chapter 6

Characterization of Fabricated Microfluidic Devices

The characterization of microfluidic devices was realized by means of a confocal laser scanning microscope (LSM) in conjunction with a precision balance and a pressure controller. Basically, the flow behavior and biomolecule interaction within different fluidic structures were experimentally verified. In this chapter, experimental results are presented and analyzed according to the predictions obtained from the simulations results given in Chapter 4. In accordance with the specifications of the optical detector developed by Optotek, the sample can locally be illuminated by a laser, which has a focus with a diameter between 1mm to 4mm. Hence, additional microfluidic devices having circular reaction surfaces were fabricated and tested regarding enrichment efficiency. From these results, an optimal microfluidic device was identified and suggested to be used in the NANODETECT prototype.

6.1 Flow characterization

A measurement setup as represented in figure 6.1 was implemented to characterize the flow throughout the microfluidic chips. This measurement setup is conformed of a pressure controller (DP510), a precision balance provided by Sartorius, a PC with LabView software package, microfluidic devices with a channel height of 150μm because they showed the best uniform and constant velocity magnitude along the channels (see section 4.4) and their respective fluidic connections. Therefore, a holder was designed and manufactured by using Teflon, which is chemically inert, non-toxic and non-absorbent material. This holder has two 1/4-inch side ports enabling the connection of the in- and outlet of the microfluidic device with standard fittings of fluidic tubing, in this case 1/4-inch male barbed adaptors. Another function of the holder is to keep the microfluidic devices in place during measurements and ensuring

the realignment of the measurement equipment. After connecting the ports by male barbed adaptors, a pressure was applied through the inlet up to 80mbar. The pressure difference was generated by means of the pressure controller at 5mbar intervals. It was controlled using the corresponding LabVieW software.

In microchannels, air bubbles often appeared during the flow characterization. Once air bubbles were formed in filled microchannels, it is difficult to remove them from the sample. This problem could experimentally be observed during several measurements. Air bubbles must be avoided when flow characterization is performed; otherwise air bubbles alter the pressure within the microchannel, thus generating wrong results.
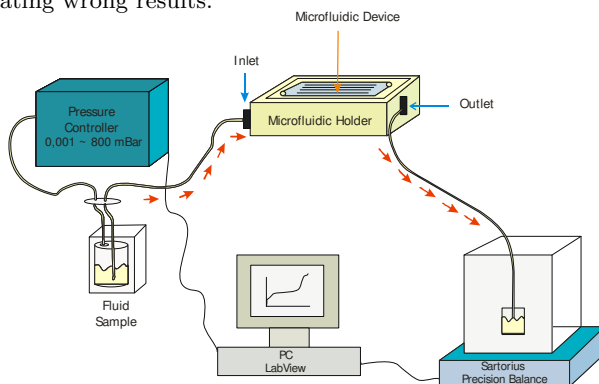
Figure 6.1: Schematic measurement setup to carry out the flow characterization of the fabricated microfluidic devices. The red arrows indicate the direction of the fluid. Fluid sample flows from the vessel containing the fluid sample into the microfluidic device to the reservoir placed on the precision balance. This measurement system has been implemented at IMSAS with the purpose of identifying the flow resistance of proposed microfluidic structures.

In order to avoid the formation of air bubbles along the microfluidic structures, microfluidic devices were rinsed with isopropanol. Isopropanol increases the wettability of the inside surface of microfluidic devices with the sample. When the microfluidic devices were rinsed with isopropanol, the formation of air bubbles was drastically reduced, thus ensuring the contact of the fluid to all inner surfaces of the microfluidic system.

After rinsing the microchannels with isopropanol, raw milk was driven through the microfluidic structures by the pressure drop. The volume of raw milk that flowed along the microchannels was then accumulated in a defined time. The

weight of the reservoir with raw milk was measured by a precision electronic balance and monitored in a defined time by a LabVieW software. From these measurements, the flow rate could be calculated and in the same way, the flow resistance was determined being the relationship between the fluid flow rate and pressure applied on the inlet of the microfluidic chip. Figure 6.2 shows the pressure drop across the microfluidic structures versus the flow velocity. The pressure difference increases almost linearly with the flow velocity as expected according to the Hagen-Poiseuille equation expressed in pressure drop (see equations 2.8 and 2.9).
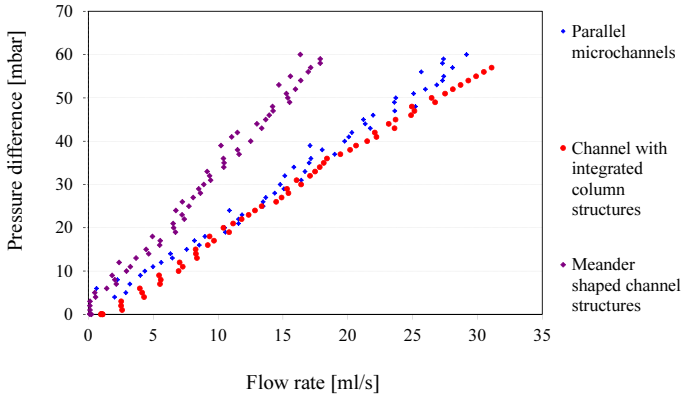
Figure 6.2: Influence of the flow velocity on pressure drop within different microchannel geometries. The relationship between the pressure difference and flow rate represents the flow resistance. The flow resistance of proposed geometric designs are compared in this figure.

The flow resistance of the microfluidic device with parallel microchannels is almost identical to the microfluidic system with integrated columns as shown in the figure above. The small difference between the two channel configurations is mainly attributed to the channel length. On the other hand, the flow resistance of microfluidic devices with meander shaped channel is high indicating a greater pressure loss.

According to the quantitative results given in figure 6.2, microfluidic devices with integrated columns and parallel microchannels show low flow resistances. At low flow resistance in microfluidic devices indicating high flow rates. Similar results were obtained by the simulations (see 4.4.1). High flow rates might be an enormous advantage, because fluid samples can be analyzed in a relatively short time.

Based on these results, the microchannel with integrated columns and parallel microchannels might be optimal geometries for the current application. However, additional experimental tests must be performed to confirm this assumption. These experiments are presented in the following sections.

6.2 Verfication of protein binding

As mentioned in section 6.1, low flow resistance guarantees high sample circulating rate, thus performing the analysis of fluid samples in short times. However, low flow resistance can also be a disadvantage regarding the binding of biomolecules. When flow rate increases, shear forces also raised. As a result, the stability of immobilized biomolecules might negatively be affected, thus leading to poor functionality and low sensitivity.

According to [MSJ+06] and as demonstrated in Chapter 3, the covalent binding is a stable and efficient way for attaching antibodies to SU-8 because of the strong attractive forces existing between the biomolecules and epoxy groups of the SU-8 surface. Covalent binding is one of the strongest chemical bonding and therefore, it is not affected by shear rates generated by fluids. However, the stability of immobilized antibodies must be evaluated under fluid flow conditions because the antibody-antigen binding is a hydrogen bond, which belongs to the group of weak chemical bonding.

In order to evaluate the stability of immobilized antibodies, the effect of antibody density (relative adsorption) was examined at different flow rates. These experiments were performed by ttz/BIBIS. First, microfluidic devices were charged with specific antibodies at 0.4mL/ min and then incubated for 2h at room temperature. Unbound substances were washed away using a buffer to avoid data errors.

Once the microfluidic devices were coated with the antibodies, enzymetracer composed of antigens and horseradish peroxidase labeled antibodies (HRP) was injected into the microfluidic device at three different flow rates and the signal generated by enzymetracer binding was recorded. The flow rate was increased from 0.4mL/ min up to 4.2mL/ min and the binding signal was measured. The results shown in figure 6.3 revealed that antibody adsorption was not affected by different flow rates. It shows the strong and stable linkage between the antibodies and epoxy groups of the SU-8 surface under tested flow conditions.
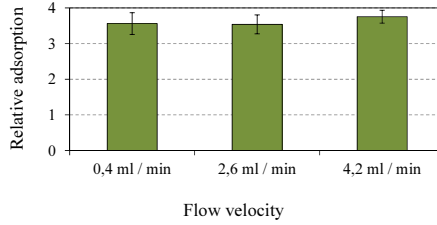
Figure 6.3: Antibody immobilization as function of different flow rates in microfluidic devices. The binding signal is given as the relative adsorption as function of different flow rates. The data presented are the average of three independent experiments, each performed in triplicate.

6.3 Measurement using luminescent particles

In Chapter 4, proposed microstructures were simulated to analyze how the shape of the channel can influence the flow velocity profile. From the simulation results, the channel with integrated column structures was selected as the optimal design because of the particular fluid flow velocity profile, low flow resistance and increased surface. In order to evaluate the immobilization performance, flow visualization was used as a qualitative measure of immobilization performance using a confocal laser scanning microscope.

For this analysis, microfluidic devices with parallel straight channels, meander shaped channel structures and with structured columns with a channel height of 150μm were fabricated because of their uniform and constant velocity magnitude in comparison with the other channel heights evaluated in this dissertation (see section 4.4). The measurement setup with utilized components are shown in figure 6.4.

The LSM is established as a valuable instrument for obtaining non-invasive and high resolution images. To visualize the interaction of very small particles along the microfluidic structures, distilled water was mixed with FITC particles (Fluoresceinisothiocyanate, marked latex particles) having a diameter of 977nm. Then, the resulting fluid flow (0.05mg/mL FITC nanoparticles in distilled water) was induced via pressure driven flow throughout the microfluidic chip. The portable micro pump mp6 was utilized for this purpose (see section 7.3). According to the characteristic curve of this micro pump , the inlet flow rate was increased to 5mL/min reaching its maximum value. This value was obtained by applying a voltage of 250V at 100Hz to the pump controller [Bar10].
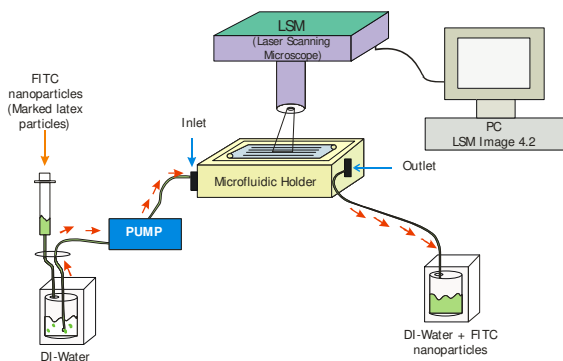
Figure 6.4: Schematic measurement system using FITC particles with a diameter of 977nm. The red arrows indicate the fluid direction. The trajectory of FITC along the microchannel was observed by using laser scanning microscope. The series of images captured during the flow visualization were then analyzed using the LSM Image 4.2 Viewer software. This measurement system was implemented at the Jacobs University Bremen.

After required equipment states were defined and fluid connections were made, the fluid flow was pumped and fluorescence development was simultaneously visualized and photographed through LSM. The probes were observed on three different channels with corresponding excitations and emissions lights.

1. Nano particles FITC dependent green fluorescence was excited using a 488nm laser and detected through a long-pass filter LP 505nm.

2. DI water dependent red fluorescence was excited using a 543nm laser and visualized using a long-pass filter LP 560nm.

3. SU-8 structures dependent blue fluorescence was excited with a 633nm laser and detected through a long-pass filter LP 650nm.

Figure 6.5 shows the particle distribution within the microfluidic devices with parallel shaped channels, meander shaped channels and with structured columns, which have a channel height of 150μm. During the measurement of the fluorescent signal, circulatory paths or flow vortices did not take place. A homogeneous distribution of nanoparticles was observed as expected from simulation results by using microfluidic devices with a channel height of 150μm (see section 4.4). In spite of this uniform flow profile and respectively particle distribution, the interaction between marked nanoparticles and SU-8 walls was not observed in all microfluidic devices; thus reducing the possibility of particle adhesion. According to the experiments using marked particles, the amount of immobilized particles was markedly low within microfluidic devices with

parallel and meander shaped channels. In contrast to that, a large amount of immobilized particles was observed within the channel with integrated columns as shown in figure 6.5. The particle adhesion observed within microfluidic devices with structured columns was attributed to the particular flow profile generated by the staggered arrangement of the structured columns. In this case, the flow velocity decreases considerably when approaching the column surface. Although laminar flow is also present in this microfluidic device, the direction of marked particles was strongly influenced by the presence of the structured columns. The advantageous trajectory and the resulting immobilization of the particles are then associated to the stagnation point. Some particles flowed between the columns, whereas particles flowing in direction to the column surface were caught by the stagnation zone. Because of the very low velocities encountered in this region, marked nanoparticles could not change the flow direction and thus, they had sufficient time to bind covalently to the column surface. The nanoparticles moving between the columns continued flowing until approaching the next column surface. The visual observation of marked nanoparticles within the channel with integrated columns demonstrated that a large amount of FITC particles could be adhered in the column region. Stagnation point took place in the vicinity of the structured columns being an optimal mechanism for increasing cell adhesion. In accordance with the experimental results presented in this section, the microfluidic device with integrated columns is the best device for the current application.

(a) (b) (c)
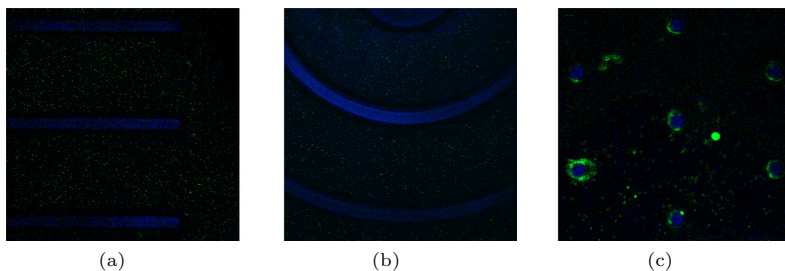
Figure 6.5: LSM micrographs of FITC flowing within the microfluidic devices. The probes were visualized on three channels with corresponding excitations and emissions: FITC (488 nm, LP 505 nm), green color; fluid (543 nm, LP 560 nm), red color; SU-8 structures (633 nm, LP 650 nm), blue color. The images were analyzed using the LSM Image 4.2 Viewer software. The images were taken after approximately 450 sec. After this time, any significant change was observed. Distribution of FITC particles within microfluidic devices with a channel height of 150μm (a) parallel shaped channels (b) meander shaped channels (c) structured columns.

6.4 Characterization of further developed microfluidic devices

In accordance to the final specification of the optical detector, the laser has a circular focus area. The laser light is passing through a pinhole, which can be selected from 1mm to 4mm. The focus area is static and cannot be used to scan wider areas. Hence, it was decided to redesign the basic layout of the microfluidic chip. Additional microfluidic devices have been designed, simulated and built to find an optimal solution to use the measurement area of the optical detection system. In this section, the different devices are presented and further their enrichment efficiency and simulation results are presented. These results are also compared with first measurements performed by using the optical detection system.

6.4.1 Redesigned microfluidic devices

According to the results presented in the previous sections, the microfluidic device with integrated column structures was selected as the optimal design for efficient cell adhesion (see also Chapter 4). Based on that, it was decided to simulate and built different types of devices with integrated columns. Two parameters were changed for the redesign: the channel width in the main section of the channel and the placement and respectively number of the columns. The columns were placed only within the area, which is focused by the laser. Hence, the desired effect is generating, but not having columns outside the focus, on which the particles could be immobilized before entering to the circular focus area. The distance between the columns remains $500\mu m$ as within the first designed microfluidic devices with integrated columns.

Figure 6.6 shows a schematic representation of the microfluidic channel, which has a circular focus area. As shown in this picture, microcolumns are placed in the center of this channel with a surface area of 4mm of diameter. Figure 6.6 (a) shows a top view of the microfluidic channel and figure 6.6 (b) illustrates the side view with the laser excitation spot diameter. Polymeric materials, such as PMMA GS and SU-8 were again selected for the new generation of microfluidic devices (see figure 6.7) in order to serve the aim of having more convenient microfluidic devices when it comes to mass production for the application. The additional microfluidic devices were produced on a surface of 14 x 8mm^2 for further experiments. The position of the in- and outlet were fixed, the channel width in the main section was varied with a constant increase-decrease from the in- and outlet to the middle. These microfluidic chips were fabricated by using the method explained in section 5.3.

(a) (b)
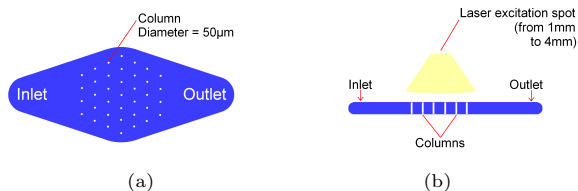
Figure 6.6: Schematic representation of a microfludic device with integrated column structures (a) Top view of a microfluidic device. The structured columns are located in the middle of the microfluidic device with a surface area of 4mm of diameter (b) Side view of the microfluidic device, which is illuminated by the laser light passing through a pinhole. The diameter of the pinhole can be selected from 1mm to 4mm.

Figure 6.7: Fabricated PMMA GS / SU-8 microfluidic devices with dimensions of 14 x 8 x 4.2mm (length, width, height).

6.4.2 Velocity flow profile simulation

As debated in previous chapters, the local and overall velocity profile of a microfluidic device influences considerably the distribution of the biomolecules. Likewise, the enrichment efficiency was affected by the flow velocity profile as demonstrated in the previous section of this chapter. Therefore the selection criteria for the redesigned layouts is an even flow-rate through the channel, hence a uniformity in global velocity, which is overlain by the desired local non-uniformity (stagnation points) due to the columns. Since the channel width of the new layouts is also changing in the main area of the devices, the global velocity also changes with flow direction, but is aimed to be even in every cross section of the channel width. The velocity profile of each new layout was simulated using the software Comsol Multiphysics 4.1. Milk was selected as fluid medium using a flow rate of 2mL/min as used in the experimental stage (see section 6.4.3). All simulations results are represented by colors. Low flow velocities are represented by blue to yellow color, while high velocities are represented by red color (for detailed description, see section 4.4).

Figure 6.8 (a) shows the simulation results within the microfluidic device with 1mm of diameter. Non-symmetric flow fluid velocity could be recognized, which might influence negatively the interaction of the nanoparticles along the microfluidic device. Consequently, low cell adhesion is expected. In comparison with the previous fluidic system, the flow velocity profile within the microfluidic device with 2mm of diameter is relatively homogeneous within the main area as shown in figure 6.8 (b). This homogeneity might enable an uniform distribution of bioparticles in the observed area and therefore, efficient cell adhesion is expected. However, in a small line close to the side walls a faster stream develops, which creates a bypass effect of the area of the columns-area.
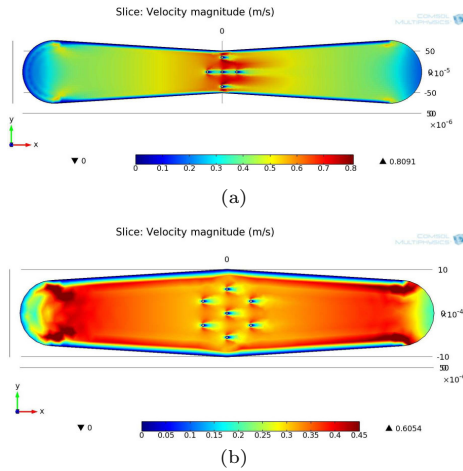
Figure 6.8: Velocity magnitude contours within a microfluidic device with (a) 1mm and (b) 2mm of diameter as area for binding reaction.

In the microfluidic chip with 3mm of diameter, a smooth global velocity profile can be observed (see figure 6.9 (a)). Only in the middle of the channel it can be seen, that the velocity between channel wall and the outer columns is slightly slower than between the columns. Hence, the fluid is directed through the columns region and no bypass exists. Therefore, a good cell adhesion is expected. In contrast to the previous fluidic systems, the flow velocity profile of the microfluidic chip with 4mm of diameter changes sharply in the middle of the channel. The flow velocity becomes significantly less in the upper and downer edge of the channel as shown in 6.9 (b) causing a non-homogeneous cell distribution. Nevertheless, cell adhesion is expected due to the amount of columns and the fact that all of the fluid will pass the columns-area. .
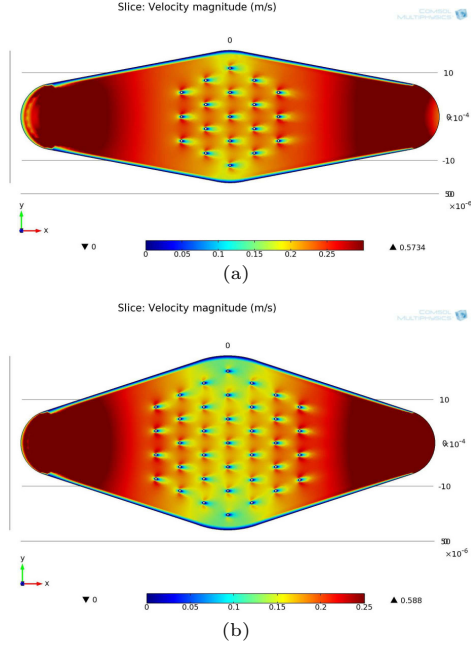
Figure 6.9: Velocity magnitude contours within a microfluidic device with (a) 3mm and (b) 4mm of diameter as area for binding reaction.

Simulation results demonstrate that the adaption of the width microfluidic channel according to the diameter of the laser focus area influences the homogeneity of the global flow velocity profile. The best flow uniformity was observed within the microfluidic device with sensing area of 3mm followed by 2mm. Hence, these are expected to enable the best interaction between the biomolecules and bioactivated bottom, ceiling and wall of the microfluidic channel. For further optimization of the velocity profile especially for the unsatisfactory designs, further adaption of the distance between the columns or a inconstant in-/decrease of channel width would be needed in order to avoid bypasses or areas with less flow-through. Additional alternative designs were not considered in the scope of this dissertation.

The expected distribution efficiency and resulting cell adhesion have been verified by enrichment experiments by using labeled phycoerythrin (PE). The quantitative and qualitative results are given in the following subsection.

6.4.3 Enrichment efficiency

For the detection unit, binding efficiency is necessary in order to increase fluorescence signal and thus sensitive detection. By increasing the surface reaction in the microfluidic device, sensitivity increases. However, the observation of larger areas in the microfluidic device increases also the measured background fluorescence of the PMMA and SU-8, which reduces the signal-to-noise ratio. In order to verify the most efficient sensing diameter, enrichment efficiency in each fluidic chip was tested as explained previously. The required experiments to evaluate the enrichment efficiency were performed by ttz/BIBIS. First, anti-PE antibodies were immobilized within the microfluidic structure, followed by the pumping of raw milk containing PE through the microfluidic device. The enrichment was then performed inserting a PE-raw milk solution (0.1mg/mL PE in raw milk) through the microfluidic device at 2mL/min, followed by a washing step. This procedure has been performed three times for each microfluidic device. After performing the assay within the microfluidic system, it was observed under the fluorescence microscope (Axiovision, Zeiss) at 546nm, 50-times magnification and 5 sec exposure time. In order to evaluate the most efficient microfluidic device for cell adhesion, several pictures were taken from the middle of each system and compared among each other. The qualitative results are shown in figure 6.10.

(a)

(b)

(c)

(d)
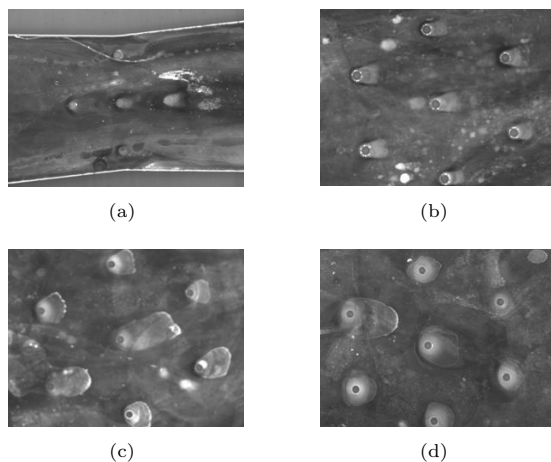
Figure 6.10: Pictures of PE-enrichment of raw milk within the center of bioactivated fluidic devices with diameters of (a) 1mm (b) 2mm (c) 3mm (d) 4mm. 50-times magnification, 5 sec exposure time at 546nm.

From visualized results, the microfluidic system with a diameter of 3mm diameter seemed to be best suited for the enrichment followed by the 2mm diameter. These results agree with simulation results. Nevertheless, a quantitative measurement must be performed to verify visual and simulation results. To achieve that, microfluidic systems coated with labeled PE were also measured by the optical detection system. In this measurement setup, microfluidic devices were illuminated using a laser excitation spot of 1mm. The smallest size of laser excitation spot was selected, so that only the column region of each chip is measured and not the wall of the channel, which shows the highest background fluorescence intensity. The microfluidic devices were placed inside the detector manually and every device was measured at least three times. The results are depicted in figure 6.11. Individual points (black solid squares) represent spacious homogeneity of the measured sample. The red empty circles represent the average. Measurements of the local excitation of the center of the microfluidic devices using the optical detection system indicated that devices with 3mm are the best suited fluidic chip for PE enrichment. Comparable results were also obtained in own experiments and simulation results.
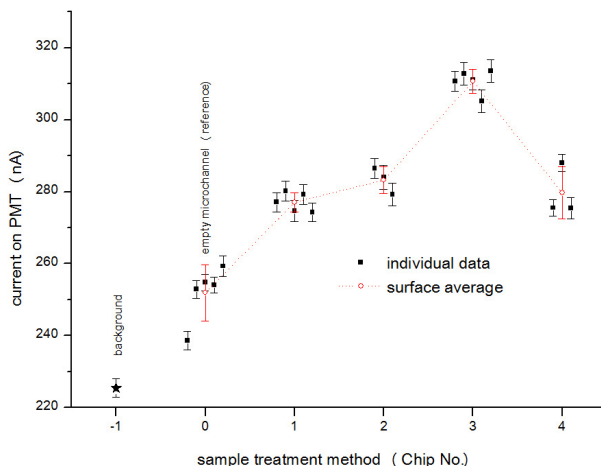
Figure 6.11: Measurements of emitted fluorescence by PE within microfluidic devices with 1mm, 2mm, 3mm and 4mm of diameter. Laser excitation spot of 1mm in diameter was used. Enrichment was performed by using PE mixed in raw milk (0.1mg/mL PE in raw milk). Measurements were performed by using a laser excitation spot of 1mm to ensure that the column region is only illuminated and not the channel wall. Measurements were performed at Optotek.

6.5 Results and discussion

As observed in all simulation results, the flow velocity around each column is lower than in the rest of the microfluidic channel. This velocity profile, which has a stagnation point, leads to an efficient enrichment around the column structures as already demonstrated in experimental results. However, homogeneity in fluid velocity also influences the efficiency in PE-enrichment. By uniform flow velocity profiles, homogeneous distribution of labeled PE throughout the microfluidic channel was expected. From four different microfluidic devices, uniform velocity profiles were observed in the chips with 3mm and 2mm of diameter. Pictures of PE-enrichment of bioactivated channels also indicated that the microfluidic system with 3mm is the most suited for PE enrichment due to the global homogeneity in the measurement area and also high local signal intensity. An external quantitative measurement confirmed that the microfluidic chip with 3mm of sensitive area is the best system for the enrichment of large amount of PE. It must be noted that the same volume of PE-labeled was used in all microfluidic devices for direct comparison.

Since the surface area showed significant influence on the PE binding, the diameter of the pinhole of the laser beam has to be also selected. Normally, larger pinhole diameters are recommended in biological applications in order to ensure a sufficient signal-to-noise ratio in the final confocal image. Previous measurements made by the optical detection system were performed using a laser excitation spot of 1mm to ensure that the column region is only illuminated and not the wall of the channel. As mentioned in section 6.4, the diameter of the pinhole, through which the laser light passes, ranged from to 1mm to 4mm. According to the current simulation and experimental results including measurements using the optical detection system, microfluidic devices with a diameter of 3mm are the most efficient for the enrichment of specific proteins. Hence, pinholes of 3mm of diameter could be used to increase sensitivity. However, wall of the channel could be also illuminated increasing background fluorescence. For this reason, a pinhole with a diameter of 2mm was selected to be implemented in the optical detection system to avoid channel wall illumination and thereby, increase sensitivity.

Chapter 7

Integration and Characterization of the NANODETECT Prototype

In this thesis, Lab-on-a-Chip in combination with the sensitive and specific immunoassay has been used for the development of a prototype to monitor raw milk without requiring sophisticated instruments. After the integration and subsequent optimization of the prototype, several measurements have been carried out to detect different concentrations of contamination or undesired particles encountered in raw milk. The performance of the prototype has been tested in order to verify its functionality and accuracy. This chapter describes the work performed in the course of this thesis to assemble and integrate all components of the NANODETECT prototype and its characterization by using real samples.

7.1 Design considerations of the prototype

The design of the NANODETECT prototype involved five important stages: design and fabrication of the microfluidic devices, development of the immunoassay process within the microfluidic channels, definition and construction of the optical detection system, visualization of data results and respective assembly of the components. After an extensive research study of each stage, planning, performing experiments and a subsequent verifications of results, the first prototype was designed and constructed.

This dissertation includes two prototype designs, both based on the immunoassay protocols described in Appendix E.1. The difference between both designs lies mainly on the fluid connection. In the first design, pumps were connected in parallel, while in the second design, pumps were connected in serie. After performing several experiments, a serial operation was selected for the final design, due by the fact that the dead volume of the fluid path is considerably

smaller than in a parallel connection. However, both designs are presented in this chapter as suggestions for future research. The first and second prototype were designed based on the following considerations.

7.1.1 Bioactivation

According to the contamination or specific particle to be detected, the microchannels of the microfluidic devices must be treated biologically prior they are placed into the prototype. This bioactivation refers to a surface functionalization in order to ensure strong and specific covalent binding of antibodies within the microfluidic device. This functionalization consists in covering the surfaces of the microchannels with corresponding proteins, antibodies and blocking system as explained in subsection 2.2.1. This bioactivation must be performed under standard laboratory conditions. Once the inner surfaces of the microfluidic device are bioactivated, they could be placed in the prototype, in the respective microfluidic system holder to start the measurements.

7.1.2 Temperature

The mixture of raw milk with labeled antibodies (R-PE or Alexa) should be maintained at an ideal temperature. According to additional experiments realized by ttz, 20°C is the ideal temperature for performing the immunoassays. Detection experiments at different temperatures should be performed to find out in which way the temperature could affect the antibody-antigen reaction. However it has not been performed in the scope of this thesis. For the current prototype, room temperature has been considered and it has been monitored by means of a standard temperature sensor. The inside temperature should not increase more than 37°C. Over this temperature, the mixture of milk and R-PE antibodies might be affected.

7.1.3 Immunoassays

At the beginning of this thesis, specific compounds in raw milk were established to be detected by the NANODETECT prototype. These specific contaminations include low concentration of pathogenic microorganisms, such as listeria, mycotoxins, drug residues and fraud. During the development of this thesis, some problems regarding the listeria detection unit were encountered. Appropriate antibodies could not be found, thus limiting the detection of listeria.

For this reason, the NANODETECT prototype has been designed for the detection of three biological assays: mycotoxin *(aflatoxin AM1)*, fraud *(goat milk mixed with cow milk)* and drug *(gentamicin)*, which can be encountered in raw milk.

7.1.4 General detection principle

The detection principle is based on the competitive and non-competitive heterogeneous immunoassays. The immunoassay principle and selected biological detection systems for the NANODETECT prototype have been explained in more detail in subsections 2.2.

Aflatoxin detection unit

The detection unit of aflatoxin M1 is based on a direct competition assay format, in which the fluorescence signal is inversely proportional to the amount of contamination encountered in the milk sample. The procedure to detect concentrations of aflatoxin M1 is shown in the following figure.
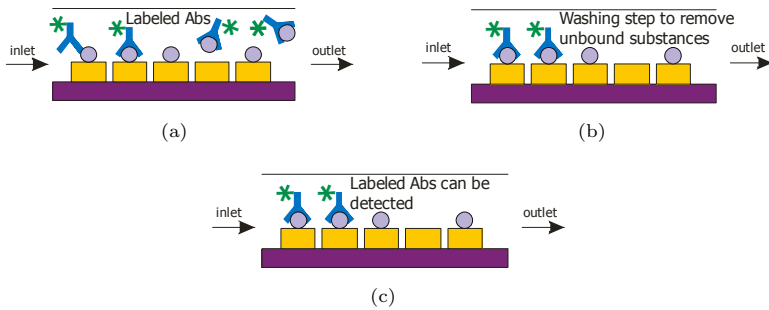
Figure 7.1: Detection procedure of aflatoxin M1 in raw milk.

a The contaminated milk is mixed with corresponding labeled antibodies. The resulting mixture is then pumped through the microfluidic chip. Free labeled antibodies (Ab) bind to coated aflatoxin M1 antigens in absence of antigens in the milk sample.

b Unbound substances such as fatty particles or unspecified proteins encountered in raw milk are washed away using a buffer.

c Once the microfluidic device is free from undetermined particles, the fluorescence signal emitted by labeled proteins (PE) can be measured by means of the optical detection system.

Drug detection unit

An indirect competition assay format has been used for the drug detection unit. The fluorescence signal is inversely proportional to the amount of contamination as well as in the aflatoxin M1 assay. The procedure of drug residues in raw milk is listed as follows:

a The contaminated milk is mixed with primary antibodies. The resulting mixture is pumped through the microfluidic chip. Primary antibodies bind to corresponding drug antigens. Unlabeled (primary) antibodies bind to coated antigen in absence of antigens in the milk sample.

b Unbound substances are washed away by using a buffer.

c Labeled (secondary) antibodies diluted in PBS are pumped into the chip. The protein binding should take place between primary and secondary labeled antibodies.

d The washing step takes place again. Once the microfluidic device is free from undetermined particles, the fluorescence signal emitted by labeled (secondary) antibodies can be measured by means of the optical detection system.
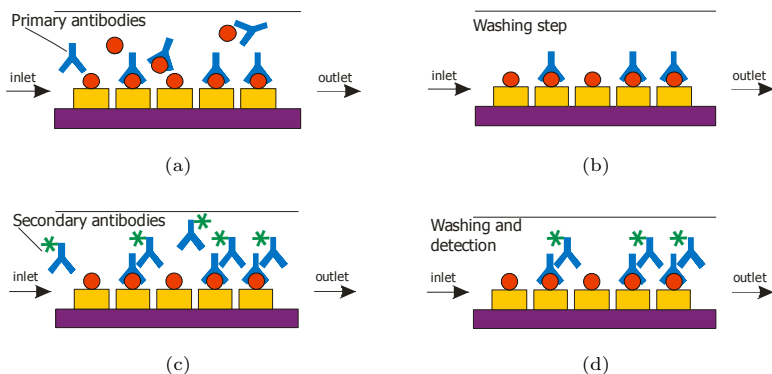
Figure 7.2: Detection procedure of drug residues in raw milk.

Fraud detection unit

The fraud detection unit is based on a sandwich immunoassay format. In comparison to last detection units, the fluorescence signal is proportional to the amount of compounds encountered in the milk sample. The procedure to detect concentrations of fraud in raw milk is shown in the following list and also depicted in figure 7.3.
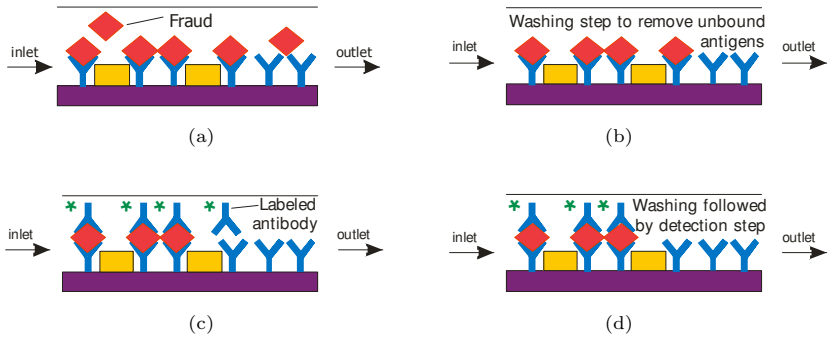
Figure 7.3: Detection procedure of fraud in raw milk.

a The contaminated milk is pumped through the microfluidic chip. Antigens bind to the catching antibodies and thereby are enriched.

b Unbound substances such as fatty particles or unspecified proteins encountered in raw milk are washed away using a buffer or water.

c Labeled antibodies are diluted in PBS and then introduced into the microfluidic system. The protein binding between labeled antibodies and corresponding antigens take place.

d The rest of unbound substances or unspecified antigens encountered in raw milk are washed away using a buffer. Once the microfluidic device is free from undetermined particles, the fluorescence signal emitted by labeled antibodies can be measured.

7.2 Detection principle in the prototype (first design)

The functionality of the biological assays has been tested at laboratory scales to detect quantitatively the presence of specific components in raw milk (aflatoxin M1, cow milk in goat milk and gentamicin residues). Immunoassay protocols have been optimized and the actual version can be found in Appendix E.1.

Procedure for the detection of aflatoxin M1 in the prototype

According to the established protocol, aflatoxin M1 unit requires two reservoirs in the prototype, which store the raw milk mixed with labeled antibodies and the washing buffer. Two pumps are used for sample transport from the reservoir to the microfluidic device and then to waste reservoir. A 3-way connector is also required to connect the tubes in parallel and thus address the fluid volumes (the raw milk and washing buffer) through the microfluidic device. This connector has been designed and fabricated using Teflon, which is a non-absorbent and chemically inert material. Two valves are also necessary to avoid back flow or wrong direction of the fluid flow. The schematic representation of this assay unit is illustrated in figure 7.4.
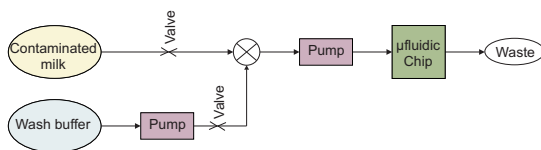
Figure 7.4: Schematic diagram of aflatoxin M1 assay unit according to established protocols.

Procedure for the detection of fraud and drug residues in the prototype

As depicted in figure 7.5, fraud and drug assays require three reservoirs respectively for storing contaminated raw milk, labeled antibodies (Dye) and the washing buffer. In this case, four pumps are used for sample transport from the reservoir to the microfluidic device and waste reservoirs. As well as in the previous assay, 3-way Teflon connectors are necessary for connecting the tubes in parallel and thus conducting the fluid volume towards the microfluidic device. In addition to that, four valves must be installed to prevent back flow.
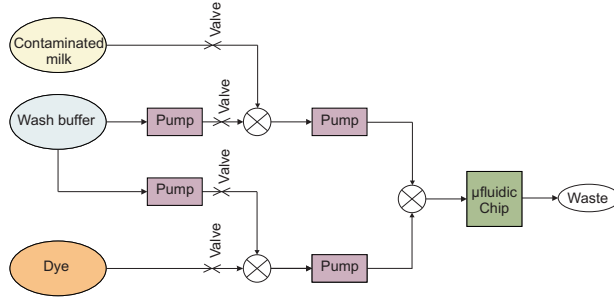
Figure 7.5: Schematic diagram of fraud assay unit according to established protocol.
.

7.2.1 Basic prototype operation (first design)

As described before, the prototype consists basically of an optical sensor, bioactivated microfluidic devices and an interface to visualize the data results. Besides the fabrication of the microfluidic devices (hereafter, μC1, μC2, μC4), the construction of a functional prototype includes the selection and installation of corresponding peripheral devices, such as fluidic connections, eight pumps (P1 to P8), eight valves (pinch valves) and a microfluidic holder (hereafter, μC holder). In addition to that, a temperature sensor (Tem1) is required to monitor the temperature inside the prototype and thereby, ensure the performance of the measurements only at room temperature. A servo motor (SM1) is also required, which is able to move the microfluidic holder and thus places the microfluidic device in front of the optical sensor. This servo motor moves the microfluidic holder from the reference point (hereafter, Ref.) to the microfluidic chamber to be measured. The final position of the servo motor depends on the assay to be detected: μC1 for aflatoxin M1 assay, μC2 for fraud assay and μC4 for drug Assay. The functionality of these peripheral devices has been defined in six different phases as shown in table 7.1. Additionally, figure 7.6 shows a schematic representation of the prototype (first design) illustrating all components and how they are connected. The connection of the peripheral devices is based on the procedures for the detection of the three assays, which have been explained and illustrated in figures 7.4 and 7.5 respectively. As shown in figure 7.6 the prototype is also composed of an extern touch screen Panel - PC as graphical user interface (GUI), with which the user can control the detailed setup such as access to the features and applications of the system. 3D drawings and a photo of the first design of the NANODETECT prototype are given in Appendix C.1.

Table 7.1: Basic prototype operation (first design).

	Phase definition	Basic procedure
1	Reference measurement	The background fluorescence of each microfluidic chip is measured. After measuring the background fluorescence of all microfluidic devices, the servo motor returns the microfluidic holder to the start position being the reference point (Ref.)
2	Immobilization phase 1	Milk+fraud and milk+drug are pumped simultaneously by P2 and P4 to the microfluidic device $\mu C2$ and $\mu C4$ respectively. The pinch valve 02 is activated closing the tubes (T60a, T60b, T60c and T60d) to ensure that the washing puffer (PBST) does not flow in direction to the microfluidic chip during the immobilization phase.
	Immobilization phase 2	Milk+alfatoxin M1 is pumped by P1 to microfluidic devices $\mu C1$. The pinch valve 02 continues being active.
3	Washing phase 1 (Fraud+Drug)	PBST is pumped by P6 and P8 for washing rest of milk+fraud and milk+drug respectively. The pinch valve 01 is activated closing the tubes (T11, T21, T31 and T41) to avoid that PBST flows in direction to the milk reservoir.
	Washing phase 2 (Aflatoxin)	The pinch valve 01 continues being active. PBST is pumped by P7 for washing the rest of milk+aflatoxin M1 .
4	Immobilization phase 3	The pinch valve 02 is activated. Fraud-dye is pumped by P3 to $\mu C2$.
5	Washing phase 3 (Fraud-dye)	The pinch valve 01 is activated. PBST is pumped by P5 for washing rest of fraud-dye reagents.
6	Detection phase	The fluorescence generated by labeled antibodies within the microstructures can be measured by the optical sensor. Data measurements are digitalized, sent to the display and finally visualized by the user.
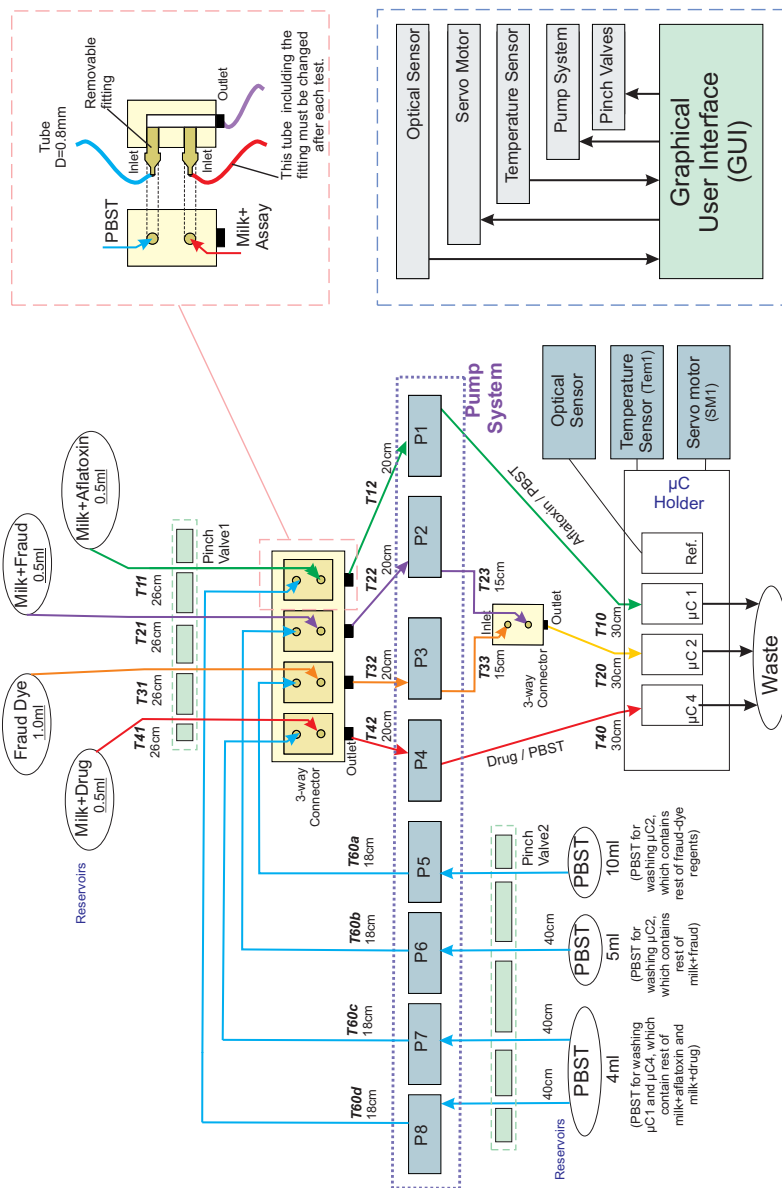
Figure 7.6: Schematic representation of the NANODETECT prototype (first design)

7.3 Peripheral devices

The main purpose of this thesis was to produce a working unit that is cost-effective, suitable for easy use and able to verify correct operation detecting contamination particles in raw milk. The, the first prototype was designed primarily adopting standard components and adapting them as illustrated in the schematic representation (see figure 7.6). The components of the prototype and the function are described in following subsections.

7.3.1 Fluidic connections

The fluidic connection was designed in such a way that users can avoid direct contact with solution mixtures and respective toxic compounds utilized for the bioactivation. The fluidic connection or chip holder must be fabricated using non-biocompatible material, which prevent subsequent adhesion of biomolecules on its surface. The fluid holder has been designed and fabricated using Teflon material, which was selected as suitable material to connect the microfluidic devices because it is non-toxic, chemically inert and non-absorbent material.

For the prototype, the chip holder contains four chambers: three chambers for the assays and one chamber as reference measurement. The exterior surface of the holder must be flat to provide a stable and smooth interface to the optical sensor. Hence, microfluidic devices connected by means of the fluidic holder could be placed in front of the optical sensor as close as possible to enhance measurement sensitivity. Schematic representation of the fluidic connection is shown in figure 7.7.
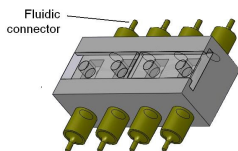
Figure 7.7: Microfluidic holder with four chambers. The holder has a removable cover for easy access to inspect and clean when it is required.

Another aspect that should be taken into consideration is the background fluorescence of the chip holder. The cover and Teflon holder exhibit high levels of fluorescence, which influences strongly the measurement of the fluorescence signal emitted by the bioparticles. For this reason, a perforation through the cover, as well as through the Teflon holder was necessary to ensure that the laser

beam exposes only the surface of the microfluidic chip. The main requirement of the perforation of the Teflon holder was the shape. This perforation must be cone shaped guaranteeing that the laser beam does not collide with the perforation walls. Another advantage of the chip holder is the cover. This cover could be opened easily by moving it parallel to the Teflon holder enabling the easy access to the microfluidic devices in a practicable way. The bottom view of the new Teflon holder design and respective cone shaped perforations are shown in figure 7.8.

(a)   (b)
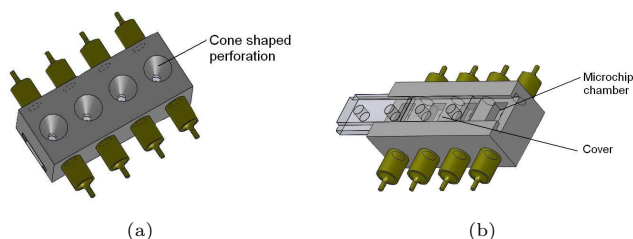
Figure 7.8: The microfluidic holder with four chambers. Each chamber has a dimension of 14 x 8 x 4.2mm (length x width x deep). The Teflon holder has a dimension of 30 x 27 x 22mm. (a) The bottom view of the new Teflon holder showing cone shaped holes. (c) The microchip holder has a removable cover enabling the easy access to the chips for easy adjustment or change for a new set of chips.

7.3.2 Translation mechanism

Depending on the assay to be measured, the microfluidic chip must be positioned accurately in front of the optical detector (i.e. laser beam). To achieve that, a gear-drive translation mechanism was designed and constructed according to the Teflon holder dimensions. The servo motor was then able to move the holder to right or left direction, which was easily controlled by varying the average of the voltage amplitude and operation time. The translation mechanism must be able to place the Teflon holder and adjust the microchannel in front of the laser beam having a maximum tolerance of 0.5mm. Otherwise, the laser beam would exposure SU-8 walls emitting high fluorescence intensities compared with labeled proteins. The translation mechanism to be implemented in the prototype is depicted in figure 7.9. According to the design of the translation mechanism, the Teflon holder could be pulled out from the housing in a feasible manner, so that the microfluidic devices could be easily removed and changed to a new set of fluidic systems.
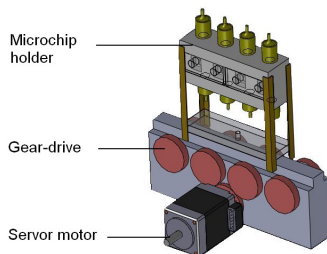
Figure 7.9: Schematic representation of the translation mechanism driven by a servo motor.

7.3.3 Pump system

In several biological and medical settings, liquids are transported through a tube with a flow rate controlled by peristaltic pumps. These pumps work by pressure and displacement, in which a rotor with several rollers compresses the tube forcing the liquid through the pump and pushing it out. The main advantage of using these pumps is that the fluids do not come in contact with the mechanical parts of the peristaltic pumps. This makes peristaltic pumps ideal for transferring chemically aggressive solutions, high-purity fluids as well as contaminated fluids as in the prototype, in which contaminated raw milk must be pumped. Although peristaltic pumps are useful in medical and biological applications, the extremely high cost (each peristaltic pump costs €1000, according to a quotation sent by Thermo Scientific) and relatively big dimensions make peristaltic pumps an impracticable option for the integration of the NANODETECT prototype. Conversely, micropumps can be an attractive alternative to standard peristaltic pumps due to their size, weight, low energy demand and low cost acquisition. Micropumps are being so far offered by companies such as ThinXXs, Star Micronics, Debiotech and Bartels Mikrotechnik for demanding applications as for example in the life science. For the pump system in the prototype, the micropump mp6 acquired by Bartels Mikrotechnik has been selected, which offers the possibility of an intrinsic flow control. This allows flexible adjustment in accordance to the prototype requirements.

The micropump mp6 is based on the working principle of piezoelectric diaphragm in combination with passive check valves. The pump consists of a pump chamber, an actuation diaphragm, an inlet and outlet valve. A piezo ceramic installed on the actuation diaphragm membrane is deformed when voltage is applied. As consequence of this deformation, the fluid is sucked into

the pump chamber generated by the upward movement of the diaphragm and it is followed by a downward movement, which displaces the fluid out of the pump chamber. The check valves define the flow direction. This functional principle can be observed in figure 7.10.
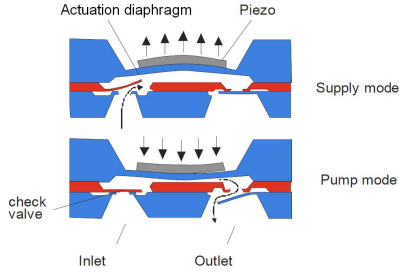
Figure 7.10: Piezo driven micropump with passive check valves [Ric08].

The micropump mp6 offers a flow performance of 6mL/min and can be controlled by adjustment of parameters such as amplitude voltage and frequency. Micropumps have been fabricated using plastic materials allowing cost effectiveness and use as disposable units. The material, which comes in contact with the fluid, is the material polyphenylene sulphone (PPSU). Bartels Mikrotechnik also offers the mp6-OEM module, which allows flexible adjustment of flow performance in accordance with the application requirements [Mag11] [Bar10]. This controller drives the mp6 performance in an integrated circuit generating up to 235V peak voltages from an external control voltage between 0.3 and 1.3V. Figure 7.11 shows a picture of the micropump mp6 with dimensions of 30 x 15 x 3.8mm. The pump controller is also depicted in this figure. For the pump system of the prototype, up to eight mp6 micropumps and corresponding mp6-OEM controller were necessary.
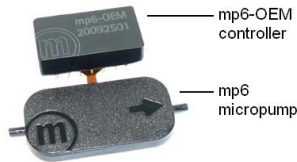
Figure 7.11: Picture of the micropump mp6 and corresponding mp6-OEM module.

7.3.4 Valve system

Since the system requires small flow rates with accurate control, a solenoid pinch valve has been selected to control the flow through the tubes. For the prototype, a pinch valve acquired by Bio-Chem Fluidics has been selected offering simultaneous operation up to 8 tubes at relative low cost (€100). Furthermore, only the inside of the tubing has contact to the fluid preventing the contamination to the mechanical parts of the valve.

The pinch valve controls the fluid flow opening and closing a mechanical system, which quenches the tubings. Through these tubings flow milk, wash buffer and required reagents. A solenoid valve is an electromechanical valve, which is controlled by an electric current. The solenoid converts electrical energy into mechanical energy. When the solenoid is energized, the valve plunger is retracted opening or closing the tubings. In contrast to that, when the solenoid is deactivated, the spring pushes the plunger back to the start position and thereby returning the tubings to the original position [Cop10]. The components of a solenoid valve and corresponding photo are depicted in figure 7.12.

(a)   (b)
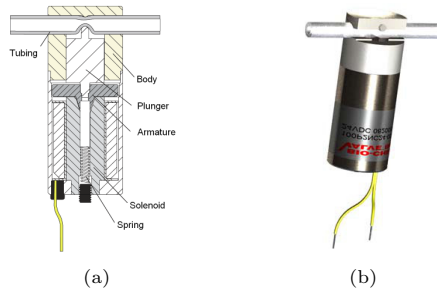
Figure 7.12: Selected pinch valve to be implemented in the prototype [Cop10]. (a) The main parts of a solenoid valve. (b) Photo of a pinch valve.

7.3.5 Graphical User Interface

A grahphical user interface (GUI) has been also implemented in the NAN-ODETECT prototype, which provides an user-friendly operation. The GUI acquired by taskit GmbH is based on a touch screen panel with dimensions of 104 x 112mm. The Panel-Card using Linux as operating system offers several interfaces to support a variaty of peripheral devices. Basically, this panel offers universal serial bus ports (USB), local area network (LAN), universal

asynchronous receiver transmitter ports (UART), general purpose input output (GPIO) and serial peripheral interface ports (SPI). UART ports have been used in the NANODETECT prototype to interface the optical detection system including the laser and the photo multiplier tube. SPI has been used to interface a Digital Analog (DA) Converter with eight outputs (AD5628, acquired by Analog Devices). Analog voltage supplied by this DA Converter has been used for controlling the performance of the pump system. GPIO ports have been used to control the valve system and translation mechanism that refers to the servo motor. USB port was used for transferring the measuring date, while LAN port was used to perform software updates or connect to the internet. The power supply was obtained by an AC/DC adapter with a DC output voltage of 12V.

7.3.6 Optical detection system

The optical detector unit implemented in the NANODETECT prototype is composed basically of an excitation laser light source, detector, filters and translational optics. Figure 7.13 shows the schematic representation of the experiment setup for reflectivity measurement and corresponding photo of the optical detector designed and developed by Optotek [opt10]. A laser diode with peak emission wavelength 532nm (Hitachi HL6344G, Thorlabs) delivering an output optical power up to 5mW in a single mode, linearly polarized beam, was used as an illumination source. The laser beam is passed through a circular aperture with 2mm of diameter in accordance with the results obtained in section 6.4.

After illuminating the sample, i.e. the microfluidic device, the light source was then detected. The detection was performed by means of a photomultiplier tube that provides high photocathode quantum efficiency having direct effects on the detection efficiency. The PMT acquired by Hamamatsu (H6780-02) was coupled to a Hamamatsu C8908 unit, which has an RS232 interface to transfer measured values to a PC. In this optical configuration, the integration of an additional photodiode was required for measuring the reference laser beam and thus detect laser fluctuations. To achieve that, the output optical power was monitored by using an integrated photodiode and controlled with a laser diode controller (LDC500, Thorlabs). Additionally, two bandpass emission filters were used to suppress scattered and reflected excitation light. Optical filters were used in the optical detection system to reflect the light at 90° enabling the illumination of the samples by using a collimated light beam. Optical filters (dichroic filters) have been also installed in the interconnecting tubes.

The fluorescent signal from the microfluidic device (test sample, see figure 7.13 (a)) passed through the emission filter blocking reflected laser output, so that signal from enhanced green fluorescent protein may be detected. The scanning parameters, as well as data acquisition were controlled with a software developed also by Optotek.

(a)

(b)
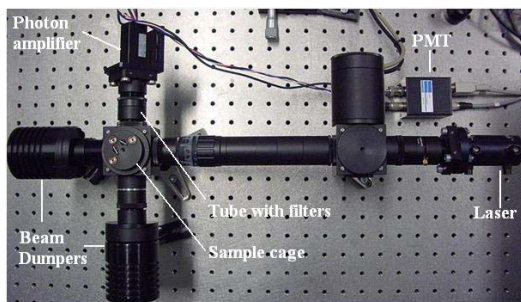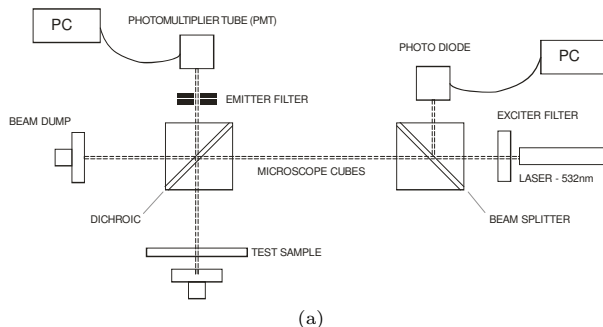
Figure 7.13: Optical detection system developed by Optotek (a) Schematic representation of the experiment setup for reflectivity measurement (b) Picture of the detection system to be implemented in the NANODETECT prototype.

Since the stability of the laser operation was an essential parameter to provide required sensitivity and selectivity, a post processing step was included in the optical detector. By using simple data post processing, laser fluctuations and respective variations in the PMT signal were detected and compensated in real time. Undesired signals fluctuations were measured and corrected to a defined value being a practicable solution to apply in the NANODETECT prototype. The post processing of signals obtained by the PMT and photodiode are described in Appendix D.1.

7.3.7 Temperature sensor

In the prototype, temperature must be considered. A temperature up to $37°C$ might not take place, otherwise proteins and reagents within the microfluidic devices can be adversely be affected. For this reason, a temperature sensor near from the microfluidic holder must be installed in order to monitor the temperature during the measurements. The temperature sensor ADT7301 acquired by Analog Devices has been selected that offers a flexible serial interface allowing an easy connection to the SPI port of the Panel-Card (see subsection 7.3.5).

7.3.8 Additional components

Additional components such as tubes and reservoirs have been also incorporated in the NANODETECT prototype. The selection of these components lied mainly on their material, which exhibit non-absorbing properties. Polypropylene (PP) material is the most appropriate material that satisfies demanding requirements, since it is highly chemical resistance and it can also be acquired at low cost. Furthermore, PP shows hydrophocitiy and poor antifouling characteristics, which prevents protein absorption.

Reservoirs with a capacity of 1.5mL of volume and tubes with an inside diameter of 0.8mm (PharMedÎ Ismaprene) were acquired by Fisher Scientific GmbH and medChrom respectively.

7.4 Optimization of the NANODETECT prototype

After assembling the first prototype design, several measurements were carried out using real samples. Because the initial results were not promising, a step-by-step evaluation has been performed to determine the necessary improvements. Based on the experience made by using the original design, the prototype has been optimized and the most relevant improvements are summarized in this section.

Accuracy

A DC servo motor was selected in the translation mechanism for the variable displacement of the fluidic holder and thus, automatically adjusting of the microfluidic chips. Although the servo motor could be easily controlled by

varying the voltage amplitude and it was a low cost solution, the servo motor showed low accuracy in the moving mechanism limiting its use in the prototype. The servo motor was not able to adjust the microchannel in front of the laser beam with tolerances less than 0.5mm.

As consequence, SU-8 walls were exposed emitting high fluorescence intensities and thus, overlapping signal emitted by labeled proteins. Since a high precision and accuracy in positioning were the most significant parameters of the translation mechanism, the servo motor has been replaced by a drive stepper motor acquired by Standa Lithuana (ref. 8MT160-300). This stepper motor consists basically of a linear stage and a RS232 controller, which offers high accurate positioning with extremely tight tolerances (in micro range).

Elimination of air bubbles within the microfluidic devices

Air bubbles were observed within the microfluidic device during primary measurements by using the prototype. Air bubbles interfere with a proper fluid flow and also with the passage of the beam of light altering the results. Some methods have been selected and implemented in the prototype to reduce the formation of these undesired air bubbles along the microfluidic system. To avoid air bubbles, the following methods were used:

1. Bubble traps provided by Trace Analytics were implemented in the prototype. They were selected because of their material composition such as PEEK and PTFE being inert and chemical resistant. These bubble traps were also chosen because they ensure no dead volume, thus avoiding the accumulation of milk residues or PBST inside of the bubble trap.

2. When microfluidic devices are replaced by new ones for performing next measurements, unavoidable air enters into the fluidic connector forming air bubbles into the microfluidic channel. The risk of air bubbles formation can be minimized by filling the chips with water prior to application.

Microfluidic device without structured columns

Based on the experience made with the original prototype, a difficulty has been observed concerning the use of the microfluidic chip with structured columns. This microfluidic system has been selected because of the many advantages over the other proposed microfluidic structures. By using this microfluidic system with structured columns, clogging channels was ruled out

and the enrichment of a large amount of specific antigens took place due to the presence of the stagnation flow around the columns. As demonstrated experimentally in previous chapters, the presence of these columns provide discrete sites for immobilization of cognitive agents such as proteins, antibodies and antigens. The flow velocity around the column was weaker than in the rest of the microfluidic system, which led to an efficient enrichment in this zone (see Chapters 4 and 6). In spite of the several advantages by using this microfluidic system, one difficulty appeared during the washing step in the NANODETECT prototype. By applying the washing step, unspecified compounds could be removed from the microfluidic device. However, unspecific particles after the washing phase have been observed behind the columns as illustrated in figure 7.14.
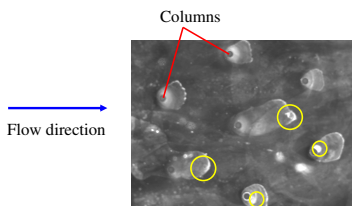
Figure 7.14: Picture of the microfluidic device after washing step. Yellow circle represent some residues, which could not washed off after enrichment.

The flow velocity behind each column was very low, so that the antigen enrichment and unspecific immobilization also occurred behind the columns as observed in this figure. Since the fluid in the prototype can be only pumped in one direction because of selected micro pumps (see section 7.3.3), the area behind the columns cannot properly washed off. Based on these results, the columns within the microfluidic device must be omitted for next measurements.

The elimination of the columns might provide an efficient washing step through the whole microchannel and also reduce the volume of SU-8, thus minimizing the background fluorescence of the microfluidic device. Nevertheless, the design of microfluidic systems with integrated column structures must be considered for future work because of the advantages in comparison to single channels (see section 4.3.2). In addition to that, the presence of altered flow patterns and stagnation point within microfluidic devices with integrated columns ensure an uniform distribution of the fluid as well as a large enrichment of proteins i.e. antibody-antigen as demonstrated in sections 4.2.3, 6.3 and 6.4.3. The elimination the columns might provide an efficient washing step through the whole microchannel and also reduce the volume of SU-8, thus minimizing the

background fluorescence of the microfluidic device. Nevertheless, the design of microfluidic systems with integrated column structures must be considered for future work because of the advantages in comparison to single channels (see section 4.3.2). In addition to that, the presence of altered flow patterns and stagnation point within microfluidic devices with integrated columns ensure an uniform distribution of the fluid as well as a large enrichment of proteins i.e. antibody-antigen as demonstrated in sections 4.2.3, 6.3 and 6.4.3.

Additional washing steps by using water

In order to determine the concentration level within the microchannel, two measurements were carried out under the same condition. The first measurement represents the background fluorescence of the microfluidic device and the second measurement corresponds to the fluorescence emitted by the microfluidic system after pumping all reagents including raw milk with the antigens, PBST and labeled antibodies. The difference between these measurements represents the concentration level within the microchannel. Figure 7.15 shows the background fluorescence of three different microfluidic devices, which were measured by using the prototype. It must be noted that these fluidic chips were previously bioactivated, meaning that specific antibodies and BSA were immobilized in the inner surface of the microchannels. PBST was also pumped to remove unbound particles encountered into the channel. The first measurements showed that background fluorescence varies from one microfluidic device to another and this significant difference was not expected. As established in Chapter 3, polymer microfluidic devices possess autofluorescence due to the properties of PMMA GS and SU-8. Nevertheless, this autofluorescence should not vary significantly, because the microfluidic devices have been fabricated under the same conditions and because thin SU-8 layers has been used.
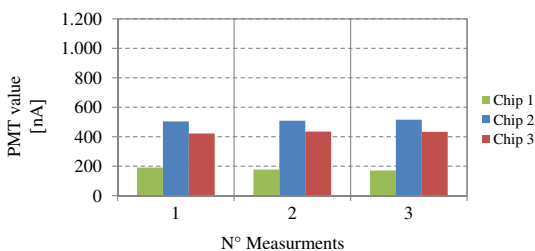
Figure 7.15: The background fluorescence of three different microfluidic chips. The measurement has been repeated three times to verify the results.

In order to prove that the microfluidic devices have similar autofluorescence intensities, an additional washing procedure has been included to the whole process. In addition to PBST, distilled water has also been pumped through the microfluidic chips to remove the rest of unbounded particles. After pumping water, microfluidic devices were measured again. The emitted fluorescence signals are shown in figure 7.16.
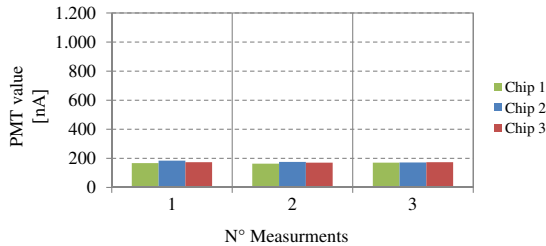
Figure 7.16: The background fluorescence after applying an additional washing step. After several attempts, optimal parameters were found out: distilled water must be pumped during 5 min at 0.05mL/ min

The variation of background fluorescence was attributed only to the different autofluorescence of each microfluidic system. However, additional experiments showed that this variation of background fluorescence was not caused by the microfluidic systems of same quality, but rather it was caused by the rest of BSA (blocking solution) and/or of PBST used for washing, which were still in the microfluidic device. Based on these measurements, two phases have been added to the original prototype operation as seen previously in table 7.1. Two new phases for water-washing have been added into the state machine of the embedded software of the prototype. These phases might guarantee that the microfluidic devices are free from undesired particles left by the washing phase using PBST. Another advantage in including these "water phases" is that the microfluidic systems are filled completely with water preventing the formation of air bubbles and thus, ensuring accurate measurements made under the same conditions.

Fluidic connection

One difficulty observed in the prototype was the non-efficient transfer of volume sample into the microfluidic device caused by the dead volume in the fluidic connections. The dead volume refers to the volume contributed by the tubing

connecting the reservoirs to the microfluidic devices including the tubing connectors, volume added by fittings and pump chamber. In order to determine the dead volume, initial volume and final volumes of each assay unit have been experimentally measured. Table 7.2 shows the dead volume in each assay unit, which differs because of the flow rate and number of tubing connectors.

Table 7.2: The dead volume according to the assay unit. The dead volume was measured experimentally from the reservoirs to the tubes that are connected to the inlet of the microfluidic devices (see tubes T40, T20 and T10 from figure 7.6.)

Pump	Assay	Flow velocity [mL/min]	Initial volume [mL]	Final volume [mL]
P1	Aflatoxin	0.026	0.5	0.250
P2	Fraud	0.026	0.5	0.185
P3	Fraud-dye	0.066	1.0	0.750
P4	Drug	0.026	0.5	0.250

As shown in table 7.2, the dead volume ranges between 0.25 and 0.315mL, which is the sum of volumes contributed by different fluidic connections. The dead volume increases considerably in fraud-dye followed by fraud unit. This is mainly caused by the tubing connector or 3-way connector as depicted previously in figure 7.6. The use of this connector was suggested to connect raw milk and wash buffer in parallel as seen in section 7.2. By using this parallel connection, the operation of the prototype would be simple and require no operator during the measurement. In this case, reservoirs must filled up once only with raw milk and reagents. Since the measurement is completed or since a new measurement must be initiated, reservoirs must filled up again. The first design of the prototype would be easy to get working. However, the amount of multiple connectors must be reduced in order to minimize the dead volume as maximum possible. In order to reduce the dead volume and thus improve the efficiency of the prototype, the fluidic connection has been modified as depicted in figure 7.17. This modification consists of eliminating all 3-way connectors of the original design, which leads to high dead volumes.
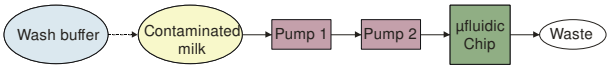
Figure 7.17: Schematic diagram of the modified fluidic connection. Liquid samples are pumped in serie into the microfluidic device.

In this way, all reagents flow to the microfluidic device using a serial continuous flow as depicted in figure 7.17. The dead volume could be reduced to approximately $45\mu L$ per fluid path. As shown in this figure, two pumps connected in serie were required for each assay unit. This serie connection by using two different pumps is because contaminated milk and washing buffer must be pumped at different flow velocities. Another significant advantage of this fluidic configuration is that it does not require the use of valves. Using the micropumps mp6 acquired by Bartels, fluid samples can only turn in one direction and reverse direction is mechanically prevented by the check valves of the micropump (see section 7.3.3). Thus, back flow can be avoided without requiring additional valves.

7.5 Detection principle in the optimized prototype (second design)

As shown previously in figure 7.17, all fluid samples including raw milk and PBST can be pumped in serie. The first micropump was set at low flow velocities (0.05mL/min) to pump raw milk, while the second micropump at relative high velocities (0.5mL/min) to pump the washing buffer and water. The procedure for the detection of each assay is briefly described below. Final immunoassay protocols can be found in more detail in Appendix E.1.

Alatoxin M1 assays

1. The microfluidic chip is pumped with water to remove the rest of particles left from PBST or BSA.

2. Raw milk containing aflatoxin M1 and labeled antibody solution are pumped by the first pump through the microfluidic chip.

3. Once raw milk with aflatoxin M1 is pumped, the user must change manually the vessel to a second vessel containing the washing puffer (PBST). The first pump stops pumping, whereas the second pump starts working.

4. The microfluidic chip is pumped with water again to prevent the formation of salt crystals from PBST.

5. At this point, the fluorescence generated within the microstructures by labeled antibodies can be measured by means of the optical sensor.

Fraud and drug assays

1. Microfluidic chips are pumped simultaneously with water to remove particles rest left from PBST or BSA.

2. Raw milk containing fraud or drug residues (+ unlabeled antibodies) are pumped through the microfluidic device by the first pump.

3. When the vessel or reservoir containing mixed milk is empty, the user must change manually this vessel to the reservoir containing the washing puffer (PBST). At this moment, the first pump stops pumping while the second pump starts pumping.

4. Labeled antibodies dissolved in PBST are introduced in the microfluidic chip. Vessels must also be changed by the user. The second pump stops pumping, whereas the first pump starts working.

5. The non-bound labeled antibodies and milk residues are washed away through the microfluidic device. Vessels must again be changed by the user. The first pump stops pumping, whereas the second pump starts working.

6. Water is pumped again into the microfluidic device to prevent the formation of salt crystals from PBST.

7. Fluorescence generated within the microstructures by labeled antibodies can be measured by means of the optical sensor.

7.5.1 Basic prototype operation (second design)

The operation of the second prototype design takes place in eight different phases, in contrast to the first design that needed six phases. Additional washing steps have been included to the prototype operation as shown in table 7.3. The addition of these new phases is due by the fact that undesired particles were still observed after the already established washing steps. These unknown substances within the microchannels might be mainly originated from the BSA and also from PBST as demonstrated in section 7.4. For this reason, water must be pumped into the microfluidic devices before the measurement of background fluorescence (reference measurement) and fluorescence emitted by labeled molecules (detection phase) take place. These phases have been defined as "water phase" as shown in table 7.3. The prototype operation and corresponding component status are given in more detail in Appendix E.1

Table 7.3: Basic operation of the optimized prototype defined in eight phases. Two new phases (1 and 7 for water-washing) have been added to the prototype operation, which ensure an efficient removal of unwanted particles from BSA or PBST within the microfluidic device before measuring.

	Phase definition	Basic procedure
1	"Water phase"	Water is pumped through the microfluidic device to remove undesired particles originating from BSA or PBST.
2	Reference measurement	The background fluorescence of each microfluidic chip is measured. After measuring the fluorescence of all microfluidic devices, the stepper motor returns the microfluidic holder to the start position being the reference point.
3	Immobilization phase 1	Milk+alfatoxin, milk+fraud and milk+drug are pumped simultaneously by P1, P4 and P7.
4	Washing phase 1	PBST is pumped to remove the rest of milk and reagents. P4 (fraud) and P7 (drug) continue pumping the milk that is still in the fluid path at a flow rate of $0.05\,mL/\min$. Then, P5 (fraud-PBST) and P8 (drug-PBST) are activated to pump the rest of PBST, but at $0.5\,mL/\min$.
5	Immobilization phase 2	Milk+aAlfatoxin, fraud-dye and drug-dye are pumped simultaneously by P1, P4 and P7.
6	Washing phase 2	PBST is pumped to remove the rest of milk and reagents. P1 (aflatoxin M1), P4 (fraud) and P7 (drug) continue pumping the milk that is still in the fluid path at flow rates of $0.05\,mL/\min$. After that, P2 (aflatoxin M1-PBST), P5 (fraud-PBST) and P8 (drug-PBST) are activated to pump the rest of PBST, but at $0.5\,mL/\min$.
7	"Water phase"	Water is pumped again to ensure that the microfluidic device is free from PBST.
8	Detection phase	The fluorescence generated by labeled proteins within the microstructures can be measured by the optical sensor. Data measurements are then digitalized, sent to the display and finally visualized by the user.

The significant difference between both designs is the fluid connection and the addition of the water-washing phase. In the original design, all reagents were pumped by using a parallel connection, whereas in the present design the fluids were pumped by means of a serial connection. As a result, the number of pumps was reduced to six and pinch valves were not required. Figure 7.18 shows the schematic representation of the current prototype design.
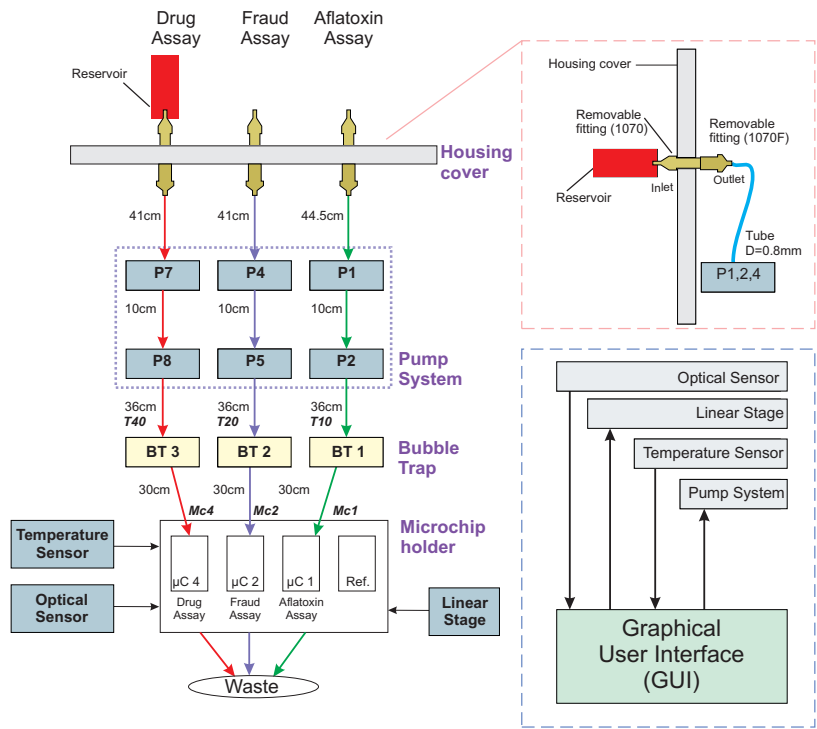
Figure 7.18: Schematic diagram of the modified fluidic system of the NANODETECT prototype. Liquid samples are pumped into the microfluidic device using a serial continuous flow.

7.5.2 Conceptual drawing of the integrated prototype

In order to improve design efficiency, a 3D drawing of the prototype including all components and respective dimensions has been created. This drawing was

made based on the basic prototype operation and schematic representation as seen previously in subsection 7.2.1. The preliminary 3D drawing shows how the components are connected giving a view on the prototype design. Because the main components developed during this thesis have been designed and fabricated separated (as the case of the optical sensor, which was developed and built by Optotek in Ljubljana, Slovenia) this 3D representation was required to define the correct position of each component in relation to the other components and whole system. The conceptual drawing of the integrated NANODETECT prototype is depicted in figure 7.19.
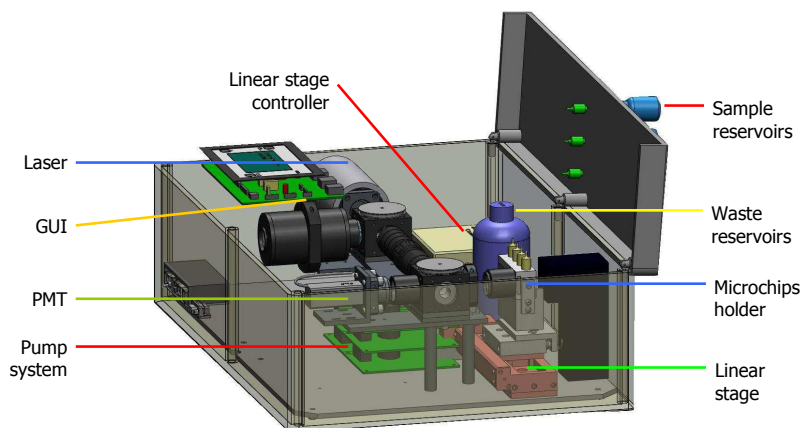
Figure 7.19: Drawing of the side view of the prototype (second design).

7.6 Assembly of the functional NANODETECT prototype

Basically, the prototype equipment consists of the optical detection system, pump system, temperature sensor, the microfluidic devices with the respective fluidic connections and the stepper motor, which were described previously. The prototype is also composed of an extern touch screen Panel - PC as graphical user interface (GUI), which provides the users or operators the visualizing of data results from the optical detector with an interactive interface. All peripheral devices of the prototype were housed in a robust and non-transparent ABS casing, which fulfils the most important requirement of light tightness. The reformed box is shown in figure 7.20.

Figure 7.20: Photo of the side view of prototype showing how the cover can be opened to change the already used microfluidic devices or carry out all necessary adjustments.

The main requisite for improving the measurement of very low fluorescence signals emitted by labeled proteins was to reduce the background fluorescence to a minimum level as possible. As already known, this background fluorescence might be produced by the microfluidic system and also by the microfluidic system holder. However, the unwanted background fluorescence might also be produced by light emitting electronic components such as the touch screen panel and respective interface connections. These connections include mainly LAN network used for software updates and internet communication. Any light sources from inside or outside of the prototype or box can interference significantly the measurement of the fluorescence. In order to avoid such emitting light, all electronic components were sealed inside the box. Additionally, the box was itself light sealed.

The housing was acquired by Fibox (code: ABS 5638 18 G-3FSH) and has dimensions of 558 x 378 x 180mm (length, width and height). The original box was modified to facilitate testing of raw milk under realistic in-place conditions. The cover can be opened easily by turning the wing screws for easy access. The operator can then change the microfluidic devices, fill up empty bottles or carry out the necessary adjustments by an uncomplicated way. In addition to that, the inside of the box was painted flat black to avoid any reflections of light that could interfere with the operation of the detector. The system power switch, USB, LAN network and RS232 connection were mounted externally for easy access for software update via RS232 or LAN and also for saving measurements via USB. Figures 7.21, 7.22 and 7.23 show different views of the complete prototype.
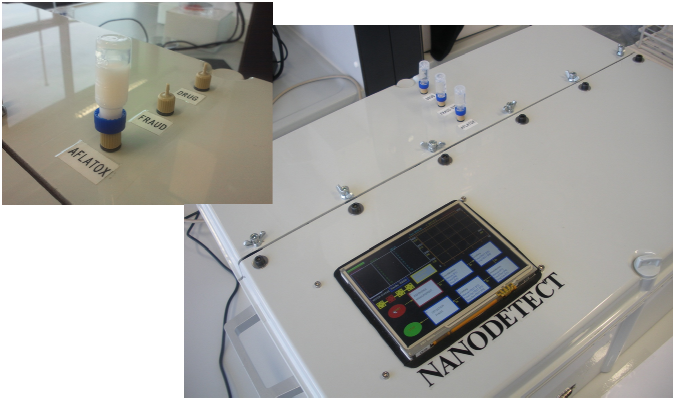
Figure 7.21: Photo of the top view of the prototype.
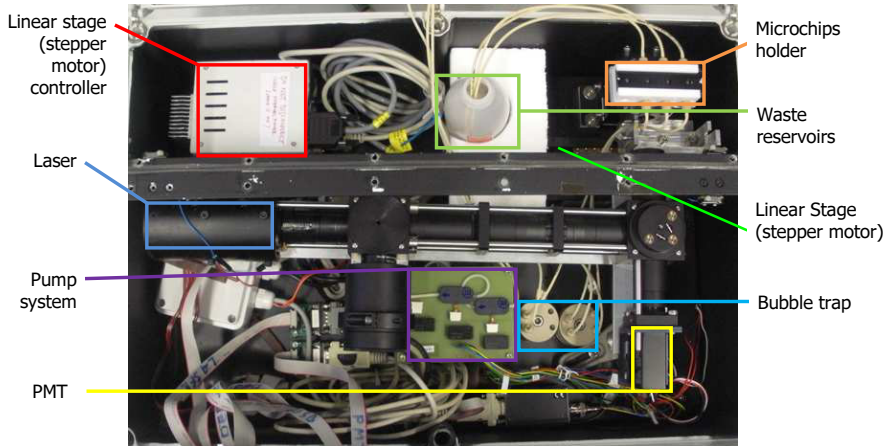
Figure 7.22: Photo of the inside view of the NANODETECT prototype.

In the GUI, an automated state machine was developed, which was created according to the prototype operation as described previously in table 7.3 or in Appendix A.1. The schematic representation of the state machine including the *main menu* and *submenu* is shown in figure 7.24.

Figure 7.23: Photo of the top view of the NANODETECT prototype.
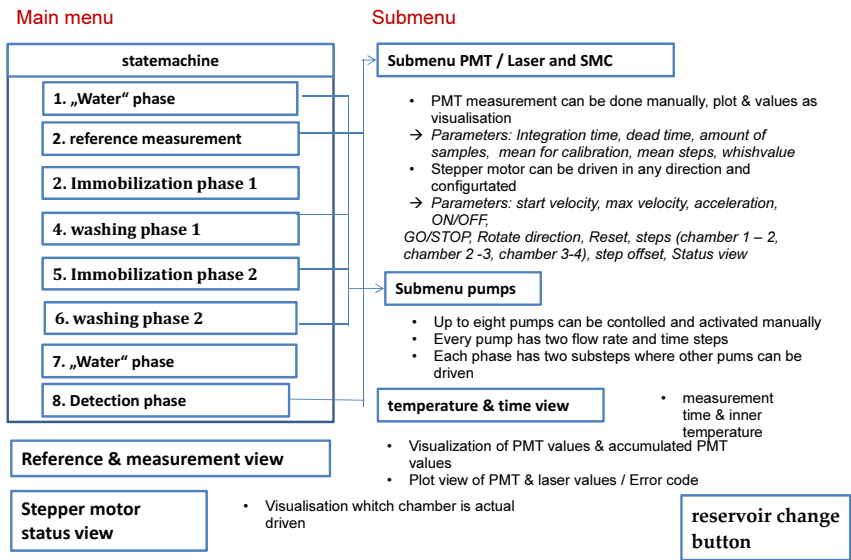
Figure 7.24: Schematic representation of the state machine of the GUI sorted in the *main menu* and *submenu*.

As shown in figure 7.24, the state machine consists of eight steps, which represent each phase of the prototype operation. The optical system, pumps and stepper motor work as defined in the state machine. All steps can be seen in the *main menu* of the GUI including the measurement time, inner temperature, the position of the stepper motor, as well as the measurement results.

Figure 7.25: Main menu of the GUI showing the state machine of the NANODETECT prototype.

In addition to that, each step can be selected separately, thus having access to the *submenu*. Figure 7.26 shows the submenu of the reference and detection phase, in which parameters of the optical sensor and stepper motor can be modified. Figure 7.27 shows the submenu of the immobilization, washing and water-washing phases, in which the parameter of the pump system can be established according to requirements of the users.
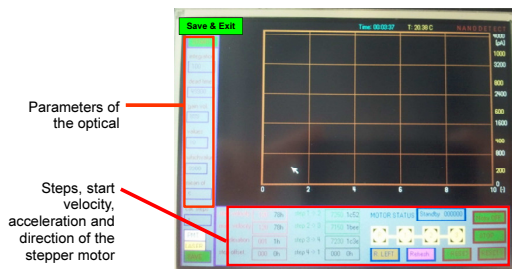
Figure 7.26: Submenu of the GUI showing the reference and detection phases.
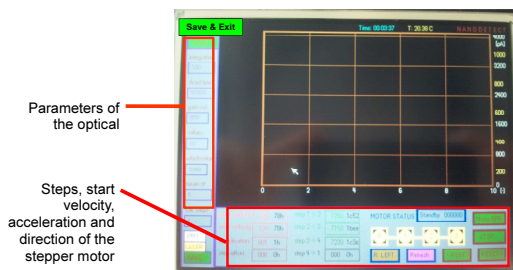
Figure 7.27: Submenu of the GUI showing the immobilization, washing and water-washing phases.

7.7 Characterization of the NANODETECT prototype

The performance of the NANODETECT depends primary on the spectral responsivity of the PMT, which is dependent upon the gain. Likewise, the PMT gain relies on the voltage applied between the anode and photocathode. In addition to that, PMT gain depends on the sequential amplification of the initial photoelectron by the dynodes as explained in section 2.6. This process guarantees an amplification of the signal up to 10^8, so giving an excellent low-light sensitivity. Since the signal to be measured is extremely low, high gain i.e. high voltage is necessary for the detection. However, high gain voltages contribute equally to the signal and to the noise. For this reason, the characterization of the prototype relies mainly on the measurement of labeled proteins in the microfluidic device, adjusting the gain of the PMT. This adjustment was performed by changing the gain voltage of the PMT, directly from the GUI of the prototype. In the NANODETECT prototype, an unique PMT voltage can be entered by using the GUI. Because aflatoxin M1 is the assay with the lowest signal compared to fraud and drug assays, the suitable PMT voltage has been experimentally selected for all assays according to the measurement results obtained from aflatoxin M1.

Different concentrations of aflatoxin M1, gentamicin and cow milk mixed in goat milk were measured by using the prototype. Before the measurement took place, all assays were prepared previously on the microfluidic devices using the method described in Appendix E.1. Basically, this method implies the immobilization of required reagents on the whole surface of the microfluidic device. In the case of the fraud assay (cow milk mixed in goat milk), anti K-casein antibodies were immobilized on the bottom, ceiling and walls of the microchannel surface of the microfluidic device. While in drug and aflatoxin

assays, gentamicin-BSA and aflatoxin M1-BSA conjugate were immobilized on all channel surfaces of the microfluidic device respectively. These methods have been explained in subsection 2.2.1. Several measurements were performed during the characterization of the prototype and the most relevant results are summarized in this section. It must be noted that required measurements for the characterization of the prototype in this thesis were realized on different days and that each measurement was performed on a different microfluidic chip. The reusability of the microfluidic devices did not take place in order to avoid wrong results.

7.7.1 Aflatoxin M1 detection

Once aflatoxin M1-BSA conjugated was immobilized on the microchannel surfaces, microfluidic devices were positioned into the microfluidic holder (Teflon block) of the NANODETECT prototype. Every fluid samples including raw milk, PBST and DI water were pumped in serie according to the prototype operation. At first, DI water was pumped through the microfluidic devices at 1.5mL/ min for 1 sec to push away the air bubble produced when the microfluidic device was introduced into the Teflon block. The risk of air bubble formation could be considerably reduced, when the microfluidic device was filled with DI water, prior it was placed into the Teflon block. After that, DI water was pumped again at 0.5mL/ min during 2 min to remove residues of BSA and PBST. Then, 3mL of milk+R-PE labeled anti AFM1 antibodies diluted in PBS were pumped through the microfluidic chip at 0.05mL/ min. Later, 4mL of PBST was pumped at 0.05mL/ min till the milk mixture, which was still in the tube, has passed the chip. An additional 2mL of PBST was pumped into the chip, but at 0.5mL/ min for 4 min. Next to that, DI water was injected through the microfluidic device at 0.5mL/ min for 7 min to remove undesired particles left by PBST. After performing all pumping steps, fluorescence generated within the microstructures by labeled proteins could be measured by means of the optical sensor at different PMT voltages.

Table 7.4 shows the measurements results of the aflatoxin M1 assay with PMT voltages of 899V and 800V. The intensity of the microfluidic system after performing all pumping steps was too high that overflow took place. Thus, PMT voltage must be reduced during these measurements. The reference measurement (prepared microfluidic chips filled with water) was measured with a PMT voltage of 899V, whereas the final measurement (microfluidic chips filled with water after performing all pumping steps) was measured with a gain voltage of 800V. Hence, the detection signal, being the difference between

the reference signal and emitted signal by the microfluidic chips after the pumping steps, showed negative values. The most important result obtained from this measurement setup was the obtained results with similar values, thus demonstrating the nearly homogeneity in background fluorescence of all microfluidic devices.

Table 7.4: Aflatoxin M1 assay with PMT voltages of 899V and 800V. The results are not comparable (NC), thus detection signal could not be calculated.

Chip NÂ°	Conc. [ppb]	Background fluorescence [nA]	Fluorescence after all pumping steps [nA]	Detection [nA]
1	0	1903.04	1186.20	NC
2	0	2164.56	1454.16	NC
3	0	2232.55	1153.37	NC

As mentioned previously, an unique PMT voltage can be entered by the GUI in the NANODETECT prototype. Since aflatoxin M1 is the assay with the lowest signal in comparison with fraud and drug assays, PMT voltage of 800V might be still too high for measuring fraud and drug assays. To avoid overflow in the output stage when measuring all assays, next experiments have been performed with PMT voltages of 600V and 700V. As mentioned before, each measurement was realized by using a different chip. Hence, the reference value and signal after all pumping steps are shown in figure 7.28 with the intention to observe the variation of the background fluorescence of each microfluidic device. This figure shows the reference measurement corresponding to the autofluorescence of each microfluidic chip. The results shown below demonstrate that the PMMA/SU-8 microfluidic devices have undoubtedly similar background fluorescence intensities as expected from the extensive analysis realized in this dissertation (see Chapter 3).
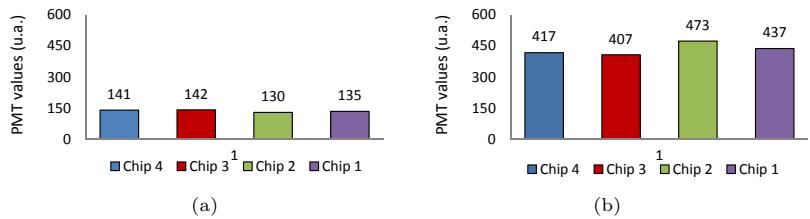
Figure 7.28: Reference measurements. Comparison of the autofluorescence of each microfluidic chip at different PMT voltages: (a) 600V (b) 700V.

Figure 7.29 shows the fluorescence intensity generated in the microfluidic device, after all fluid samples including DI water were pumped. The results shown below correspond to the sum of fluorescence signals emitted by labeled proteins and the background fluorescence of each chip.

(a)

(b)
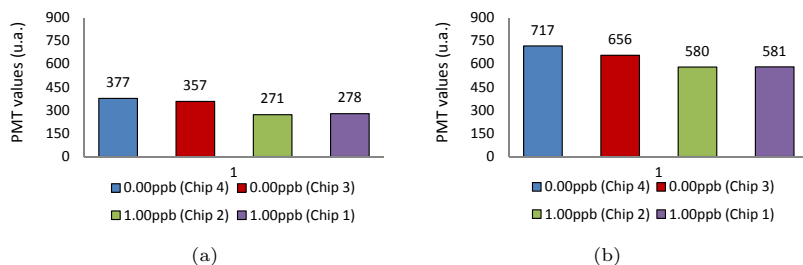
Figure 7.29: Comparison of the fluorescence emitted after the pumping step at different PMT voltages: (a) 600V (b) 700V.

For quantitative analysis, the fluorescence intensity of interest was obtained subtracting the background fluorescence from the fluorescence intensity after all pumping steps. The results are shown in figure 7.30. As seen in this figure, PMT values generated by 0ppb are higher than by 1ppb with both PMT voltages. Since aflatoxin M1 is based on a competitive assay, where the signal is inversely proportional to the amount of antigen in the sample, these results demonstrate the relative performance of the prototype. Although fluorescent signals differ slightly, both concentrations could be distinguished. Based on these results, PMT voltage was set at 700V for the next measurements, thus increasing the sensitivity.

(a)

(b)
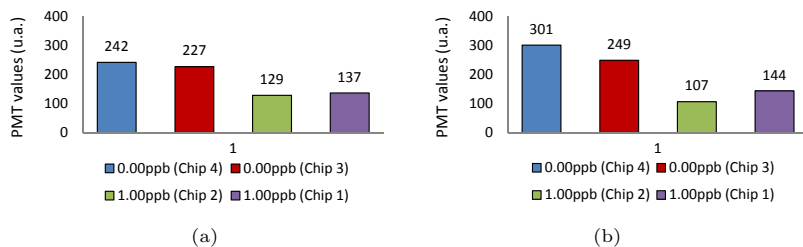
Figure 7.30: Detection signal. This signal represents the concentration of labeled proteins within the microfluidic device. Two different concentrations were measured of aflatoxin M1 by using PMT voltages: (a) 600V (b) 700V.

Additional measurements using the same procedure were performed to determine if lower concentrations than 1ppb can be detected. Figure 7.31 shows the results of a serie of experiments, in which the concentration of aflatoxin M1 was 0.05ppb. As observed in the figure below, both levels of concentration could be identified. However, the results were unfortunately not reproducible. This two point calibration was carried out for several days using different milk samples and the results showed a wide variation among PMT values of about $\geq 40\%$.
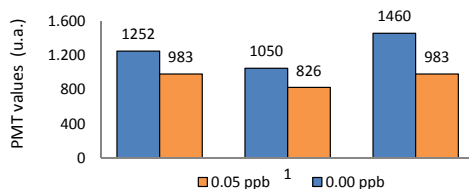
Figure 7.31: PMT values represents the concentration of labeled proteins within the microfluidic device. Each measurement was carried out on a different microfluidic chip. 0ppb and 0.05ppb of aflatoxin M1 were measured with a PMT voltage of 700V.

7.7.2 Drug residues detection

Before measurements started, prepared microfluidic devices with gentamicin-BSA conjugated were positioned into the respective chamber of the microfluidic holder. At that point, the prototype was able to begin the testing phase. The fluid samples were pumped in accordance to the sequence established in the protocol. First, DI water was pumped at 1.5mL/ min for 1 sec and then at 0.5mL/ min during 2 min to remove undesired particles from BSA and PBST. Next, 1.5mL of goat milk + anti gentamicin antibodies diluted in PBS were pumped into the chip at 0.05mL/ min.

For the washing step, 6mL of PBST was pumped at 0.05mL/ min for 20 min and then at 0.5mL/ min for 4 min. DI water was pumped again at 0.5mL/ min for 7 min to eliminate particles left by PBST. Later, 1.5mL of PE labeled goat-anti mouse antibodies diluted in PBS was pumped through the chip, followed by pumping PBST at the same conditions as before. In the final step, DI water was injected into the chip at 0.5mL/ min for 7 min to eliminate unspecific particles left by PBST. Then, the measurement of the fluorescence intensity emitted by labeled proteins took place. This procedure was repeated for each measurement and obtained results are shown in figure 7.32.

Figure 7.32: PMT values represents the concentration of labeled proteins within the microfluidic device. 0ppb and 100ppb of gentamicin were measured with a PMT voltage of 700V. Each measurement was carried out on different microfluidic chips. These results correspond to experiments performed on different days.

As well as in the aflatoxin M1, drug assay is based on a competitive assay, in which emitted fluorescence intensity is inversely proportional to the amount of antigens present in the sample. As shown in the figure above, a two point calibration was used to predict a concentration of 100ppb and 0ppb of gentamicin in goat milk. The fluorescence signals emitted by 100ppb were lower than by 0ppb as expected. However, the results were not reproducible. A variability of $\geq$ 60% with respect to the mean value was observed from measurements performed on different days.

7.7.3 Fraud detection

In this assay, microfluidic devices were first coated with anti K casein antibody and then were placed in the prototype. Once the measurement has started, every fluids were pumped into the chip in serie according to the prototype operation. In the first phase, DI water was pumped at 1.5mL/ min for 1 sec and then at 0.5mL/ min for 2 min, so ensuring the removal of any residues of BSA and PBST within the microfluidic chip. Subsequently, 1.5mL of goat milk + K-casein from cow milk diluted in PBS were introduced into the chip at 0.05mL/ min. This step was followed by pumping 4mL of PBST at 0.05mL/ min and then at 0.5mL/ min for 4 min. Next to that, 1.5mL of alexa 532 labeled anti K-casein diluted in PBS was pumped through the chip, followed by pumping PBST at the same conditions as before. Subsequently, DI water was pumped through the chip at 0.5mL/ min for 7 min and finally, fluorescence measurements took place. The results from several measurements performed on different days are shown in figure 7.33.

(a)

(b)

Figure 7.33: PMT values represents the concentration (0% and 2%) of cow milk in (a) goat powder milk (b) goat milk.

In comparison to aflatoxin M1 and drug assays, a sandwich immunoassay format was used in the fraud unit to detect the concentration of cow milk in goat milk sample. The intensity of light produced in a sandwich assay is proportional to the concentration of antigens present in the sample. Based on this principle, the experiment results shown in figure 7.33 agreed with expected fluorescence intensities. The fluorescence signal emitted by a sample with 2% of cow milk in goat milk was considerably higher than the signal generated by 0%. In spite of the variation of the results at the same concentration, there was a significant difference in signal intensity between both samples. In accordance with these results, a concentration of 2% and 0% of cow milk in goat milk could certainly be identified by comparing PMT values obtained from the NANODETECT prototype.

Additional experiments were performed to further investigate the potential of the fraud unit of the prototype. For these measurements, all experiments were performed on the same day to minimize variability. Four different concentrations of cow milk in goat milk were measured following the same procedure as explained at the beginning of this subsection. As shown in figure 7.34, the fluorescence intensity increased with increasing the concentration of cow milk in goat milk sample. Since fraud assay is a sandwich immunoassay format, these results correspond to expected fluorescence intensities.
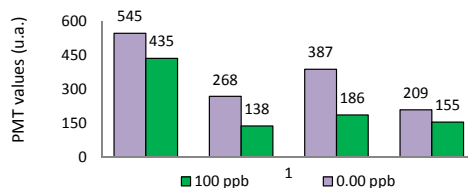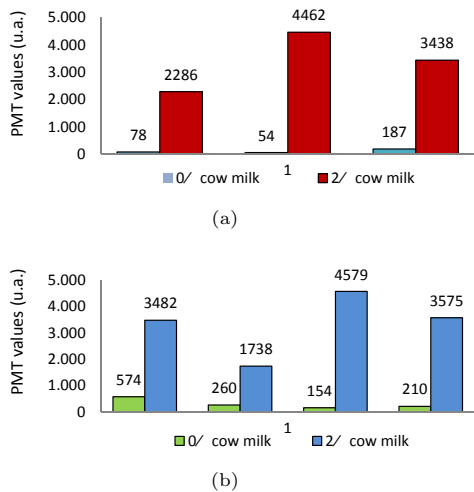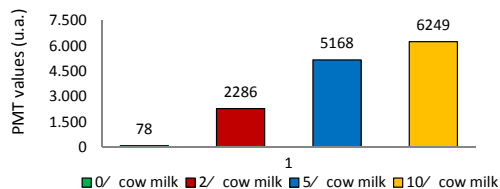
Figure 7.34: PMT values represents the concentration of labeled proteins within the microfluidic device. Each measurement was carried out on a different microfluidic chip and all measurements were performed on the same day. 0%, 2%, 5% and 10% of cow milk in goat milk samples were measured with a PMT voltage of 700V.

7.8 Results and discussion

This chapter focused on the design, assembly and optimization of the NAN-ODETECT prototype for monitoring raw milk samples. The performance of the prototype was characterized by using a two point calibration to identify the presence or absence of specific substances in raw milk such as aflatoxin M1, gentamicin and cow milk in goat milk samples.

By comparing the results of measurements performed on the same day, 0.05ppb of aflatoxin M1 and 100ppb of gentamicin could be slightly identified from blank samples i.e. 0ppb. While 2% of cow milk in goat milk could be efficiently identified from blank samples, due to the considerable difference in fluorescence intensities between both samples. Moreover, 2%, 5%, 10% of cow milk in goat milk could be clearly distinguished from blank samples. These experiments were repeated on different days in order to verify the results. The preliminary results of the fraud unit seem promising. Nevertheless, additional experiments are required to establish the reproducibility of these results. The non-reproducibility might be mainly attributed to fluctuating temperature into the prototype. The inside temperature of the prototype varied between 19°C and 27°C and thereby, the efficiency of the antibody-antigen reaction could be affected. The variation between measurements might be also caused by flow rate fluctuations. Although the micropumps were set to work at a defined flow rate (see Appendix B.1) during the delivery of raw milk to the microfluidic system, flow rate varied significantly. This variation was mainly associated to the interaction of fatty particles or unspecified proteins from milk in the pump chamber, which might cause problems such as abrasion, clogging and pressure dropping into the fluid path. These assumptions could not be experimentally confirmed in the scope of this dissertation.

The results were inconsistent when comparing the quantitative results between tests run on different days. Nevertheless, the qualitative analysis between tests run on the same day shows promising results, in which the absence and presence of unwanted substances in raw milk were identified by using the NANODETECT prototype.

Chapter 8

Summary and Outlook

In this thesis, a prototype was designed, developed and characterized to detect the empty condition as well as the maximum level allowed of specific components encountered in raw milk. The operation of the prototype is mainly based on the detection of antibody-antigen molecular recognition reaction within microfluidic devices by means of fluorescence spectroscopy. The development of the NANODETECT prototype has concerned various aspects of the complex investigation, which are summarized in the following paragraphs.

In the first part of this thesis, an extensive examination of materials, which can be used for the fabrication of microfluidic devices, was reported. Several materials were examined with respect to their structural characteristics, biocompatibility and also optical properties, such as homogeneity and minimal autofluorescence. After this examination, polymer materials such as PMMA GS and SU-8 were selected for this study on the basis of their suitability for microfluidic immunoassays. In the case of the substrate material, PMMA GS was selected because its uniformity and also low autofluorescence. Although SU-8 exhibits high autofluorescence in the required wavelength, the photoresist SU-8 was selected as the structural material because it provides excellent features for the fabrication of structures with high aspect ratio and because SU-8 can be used as adhesive material. In addition to that, SU-8 exhibits the best suitable chemical characteristics for protein immobilization. SU-8 surface ensures an efficient covalent antibody-antigen binding in comparison with other polymeric materials characterized in this thesis. According to selected materials, the manufacturing process of the microfluidic device was chosen. The complete process was described in detail including suggested changes in the procedure to minimize thickness variation of SU-8 in the coating process.

The next stage of development was focused on the analysis of flow behavior within microfluidic devices. The interaction between proteins and walls of the microchannel is essential to immobilize the biomolecules on SU-8 surfaces. Due to the existing laminar flow in microfluidic channels, the contact of a

large amount of proteins with the walls may be limited. This means that biomolecules flowing through laminar flows might be moved nearly parallel to each other avoiding the contact with the channel limiting their immobilization on SU-8 walls. However, this effect could be altered by manipulating the geometry of the microchannels. Different fluidic geometries were designed and fabricated to investigate the effect on the flow profile as well as on the trajectory of the bioparticles. The results presented in this thesis demonstrated that biomolecule adhesion profile changes according to the channel geometry. The flow profile in microfluidic immunoassays nearly plug-flow to ensure an homogenous distribution of antigens or antibodies across any cross-section of the microfluidic chip. In addition to that, it could also be demonstrated that the enrichment of specific antigens or antibodies can be increased considerably due to the presence of the stagnation flow around the structured columns within a microfluidic system. Based on simulation and experimental results, a proper channel geometry was selected and optimized for efficient biomolecule immobilization and minimal autofluorescence of the area to be measured.

As mentioned previously, the detection within the prototype was based on the measurement of fluorescence emitted in the microfluidic device. Depending on the immunoassay (sandwich or competitive inhibition format), emitted fluorescence represented the presence or absence of specific substances in raw milk. In the scope of this thesis, an optical sensor comprising basically a laser, photomultiplier tube and a photodiode with an integrated preamplifier has been used to detect the fluorescence emitted by labeled antigens or antibodies within microfluidic devices. Although photomultiplier tubes have commonly been used for very low light applications because of its high internal gain, their applicability in this thesis was limited. To detect any fluorescent signal, a sufficient amount of light generated by a laser was delivered onto the sample. When the fluorescent signal could not be detected, it was necessary to increase the PMT voltage. These factors were contradictory because the light emitted from the sample must be reduced to provide a point illumination similar to a confocal microscope, which avoids an out-of-focus signal. In turn, the light transmitted to the PMT must be increased to reduce the system noise. PMTs deliver gains up to 10^8 being optimal for very low light applications. However, as the PMT voltage increases, noise into the signal to be detected also increases limiting its use. In the NANODETECT prototype, noise was generated by a group of autofluorescence signals from sources, such as materials of the microfluidic system, fluid samples and even from the optical detector components. In order to increase the ratio of signal-to-noise, all background signals were reduced to a minimum possible. The surrounding light from the detector was

avoided by installing suitable sealing materials around the junction. Other light emitting electronics components were also sealed inside the prototype. Another unwanted fluorescence source from the optical detector was loose excitation laser rays that excite autofluorescence of inner detector walls. This problem was solved guiding the laser light accurately to the microfluidic device. Likewise, the fluorescence intensity emitted by the measured microfluidic device was guided precisely to the PMT. In addition to that, proper PMT voltage values were experimentally found out to provide a detectable signal avoiding overflow. Finally, the ratio of signal-to-noise could be increased considerably allowing the measurement of low fluorescence signals within microfluidic devices.

Another important contribution of this thesis was the design, assembly of the whole NANODETECT system and its subsequent characterization. The prototype operation was defined in accordance with the protocols for immunoassays, which are frequently used at conventional laboratories. Based on the prototype functionality, all necessary components, such as pumps, a linear stage, fluidic connections, microfluidic chips holder, among others were selected, and integrated into a working system. This integrated system, which constitutes the first prototype, was developed and built in the scope of this dissertation for the EU project NANODETECT funded by European Commission within the 7th framework program.

Several experiments were performed by using the NANODETECT prototype in order to evaluate its effectiveness for detecting undesired substances in raw milk. The empty condition and maximum level of aflatoxin M1 (0ppb and 0.05ppb), drug (0ppb and 100ppb of gentamicin) and fraud (0% and 2% of cow milk in goat milk) in raw milk were measured by using the prototype. In the case of aflatoxin M1 and drug, the difference of fluorescence intensity between both concentration levels was relatively small. However, measured concentration levels could be distinguished in both cases. Interestingly, the results of fraud assay provided the most sensitive detection compared to the other assays. The empty condition and maximum level of fraud could be easily identified because of the large difference of fluorescence intensity between these concentrations.

Additional experiments demonstrated that goat milk blended with cow milk in different concentrations (0%, 2%, 5% and 10% of cow milk in goat milk) could be also detected by means of the NANODETECT prototype. Further, it could be demonstrated that the prototype could be used for simultaneous analysis of several compounds. Measurements of aflatoxin M1, drug and fraud concentrations could be realized at the same time. The number of compounds

analyzed in the prototype can be increased even for four different compounds being an important advantage over conventional systems.

In general, the basic principle of immunoassay and fluorescence detection within microfluidic devices could be demonstrated in this thesis. Immunoassays in microfluidic devices allowed the high sensitivity of the assays for determining the presence or absence of undesired compounds in raw milk. However, some additional work is still required to produce a fully functional and transportable prototype. The hardware system including pumps, fluidic connections, optical detector and user friendliness should be optimized. In the case of the pump system, micropumps from Bartels might be not convenient for a future development because of its instability at very low flow rates and because the sample gets into contact with the pump material. Other negative aspect is associated with the sensibility of the optical sensor to small movements or vibrations. During several measurements, it could be observed that the performance of the optical system was strongly influenced even by smooth movements. After transporting, the optical sensor must be aligned to the microfluidic holder to ensure great precision and correct functionality. For this reason, the optical sensor implemented in the current prototype might not be suitable for a transportable system. An additional improvement is related to the temperature inside of the prototype. An integration of a cooling system is required in order to maintain the inside of the prototype at a constant temperature and thus prevent any influence on the immunoassay performance.

In this thesis, immunoassays within microfluidic devices were extensively examined and thereby, a significant progress was made. Different immunoassay formats were implemented within the microfluidic devices for detecting simultaneously diverse compounds encountered in raw milk samples. The presence and absence of unwanted substances in raw milk could be identified qualitatively by means of results of measurements performed on the same day.

The results obtained in the course of this dissertation show that the combination of immunoassays and Lab-on-a-Chip technology provides an innovative, powerful and user friendly alternative for the analysis of multiple analytes. With dedicated improvements, the NANODETECT prototype might be the first system to monitor up to four different compounds at the same time. The resulting technology might be transferable to innumerable applications, such as waste water treatment, drinking water, aquaculture and other areas of the food industry.

Appendix

A.1 NANODETECT Prototype Operation

#	Phase definition	Basic procedure	Fluid Volume / Flow rate	P1 Afla-toxin	P2 Afla-toxin PBST	P3 -	P4 Fraud Dye	P5 Fraud PBST	P6 -	P7 Drug Dye	P8 Drug PBST	Linear Stage	Optical sensor	Temp. sensor
1	Water Reference	Water is pumped by P2, P5 and P8. Microfluidic devices must be filled, before background measurement takes place.	PBST Volume: **3 ml** Flow rate: **0.5ml/min**			ON		ON				OFF	OFF	ON
2	Reference measurement	Background fluorescence of each chip will be measured	-	OFF	OFF	OFF	OFF	OFF	OFF	OFF	OFF	ON	ON	ON
3	Immobilization phase	Milk+Alfatoxin (reservoir 1, 1.5ml), milk+Fraud and milk+Drug are pumped simultaneously by **P1, P4** and **P7** respectively	Milk probe Volume: **1,5 ml** Flow rate: **0.05ml/min**	ON	OFF	OFF	ON	OFF	OFF	ON	OFF	OFF	OFF	ON
4	Washing	PBST is pumped for washing rest of the milk and reagents	PBST Volume: **3.5 ml** Flow rate: **0.5ml/min**											
4a		**P4** (Fraud) and **P7** (Drug) continue pumping the milk sample that is still in the tubing		OFF	OFF	OFF	ON	OFF	OFF	ON	OFF	OFF	OFF	ON
4b		**P5** (Fraud-PBST) and **P8** (Drug-PBST) are activated to pump the rest of PBST at higher flow rates		OFF	OFF	OFF	OFF	ON	OFF	OFF	ON	OFF	OFF	ON
5	Immobilization phase	Milk+Alfatoxin (reservoir 2, 1,5ml), Fraud-Dye and Drug Dye are pumped simultaneously by **P1, P4** and **P7** respectively	Milk probe, Dye Volume: **1,5 ml** Flow rate: **0.05ml/min**	ON	OFF	OFF	ON	OFF	OFF	ON	OFF	OFF	OFF	ON
6	Washing	PBST is pumped for washing rest of the milk and reagents	PBST Volume: **3.5 ml** Flow rate: **0.5ml/min**											
6a		**P1** (Aflatoxin), **P4** (Fraud) and **P7** (Drug) continue pumping the milk sample that is still in the tubing		ON	OFF	-	ON	OFF	-	ON	OFF	OFF	OFF	ON
6b		**P2** (Aflatoxin-PBST), **P5** (Fraud-PBST) and **P8** (Drug-PBST) are activated to pump the rest of PBST at higher flow rates		OFF	ON	-	OFF	ON	OFF	-	ON	OFF	OFF	ON
7	Water Washing	Microfluidic chips are pumped by **P2, P5** and **P8** with water to prevent the formation of salt crystals from PBST. Microfluidic devices must be filled, before detection phase takes place.	Water Volume: **3 ml** Flow rate: **0.5ml/min**											
7a		**P2** (Aflatoxin-PBST), **P5** (Fraud-PBST) and **P8** (Drug-PBST) are activated to pump the rest of PBST at higher flow rates		OFF	ON	OFF	OFF	ON	OFF	OFF	ON	OFF	OFF	ON
7b		**P2** (Aflatoxin-PBST), **P5** (Fraud-PBST) and **P8** (Drug-PBST) are activated to pump the rest of PBST at higher flow rates		OFF	OFF	ON	OFF	OFF	ON	OFF	OFF	OFF	OFF	ON
8	Detection	Final fluorescence (after incubation time) of each chip will be measured	-	OFF	OFF	-	OFF	OFF	-	OFF	OFF	ON	ON	ON

Figure B.1: NANODETECT protoype operation

B.1 Pump System

Figure C.1: Schematic representation of the connection between the micropump mp6 and mp6-OEM controller. The pump flow rate set by external components varying the amplitude and frequency [Bar10].

Pump	Reagent	Flow volume [ml]	Flow velocity [ml/min]	Amplitude 1 / Time 1 (reagent is close to the microfluidic chip)		Amplitude 2 / Time 2 (reagent flows through to the chip)	
Assay pumps							
P1 C1=120nF	Aflatoxin	1.5	0.05	$A_{1(P1)}$ = 540mV	$T_{1(P1)}$ = 1800sec	$A_{2(P1)}$ = 0	$T_{2(P1)} \approx$ 0
P4 C1=132nF	Fraud Fraud-Dye	1.5	0.05	$A_{1(P4)}$ = 500mV	$T_{1(P4)}$ = 1800sec	$A_{2(P4)}$ = 0	$T_{2(P4)} \approx$ 0
P7 C1=122nF	Drug Drug-Dye	1.5	0.05	$A_{1(P7)}$ = 490mV	$T_{1(P7)}$ = 1800sec	$A_{2(P7)}$ = 0	$T_{2(P7)} \approx$ 0
PBST pumps							
P2 C1=22nF	PBST Aflatoxin	3.5	0.5	$A_{1(P1)}$ = 1400mV	$T_{1(P1)}$ = 5sec	$A_{2(P1)}$ = 500mV	$T_{2(P1)} \approx$ 420sec
P5 C1=22nF	PBST Fraud	3.5	0.5	$A_{1(P4)}$ = 1400mV	$T_{1(P4)}$ = 5sec	$A_{2(P4)}$ = 500mV	$T_{2(P1)} \approx$ 420sec
P8 C1=14.7nF	PBST Drug	3.5	0.5	$A_{1(P7)}$ = 1350mV	$T_{1(P7)}$ = 5sec	$A_{2(P7)}$ = 490mV	$T_{2(P1)} \approx$ 420sec
Water pumps							
P3 (P2+P5) C1=22nF	„Water" phase1	3.0	0.5	$A_{1(P1)}$ = 1400mV	$T_{1(P1)}$ = 5sec	$A_{2(P1)}$ = 500mV	$T_{2(P1)} \approx$ 360sec
P6 (P8) C1=22nF	„Water" phase7	3.0	0.5	$A_{1(P1)}$ = 1350mV	$T_{1(P1)}$ = 5sec	$A_{2(P1)}$ = 490mV	$T_{2(P1)} \approx$ 360sec

Figure C.2: Pumpy system

C.1 First design of the NANODETECT prototype

The conceptual drawing of the first integrated NANODETECT prototype are depicted in following figures.
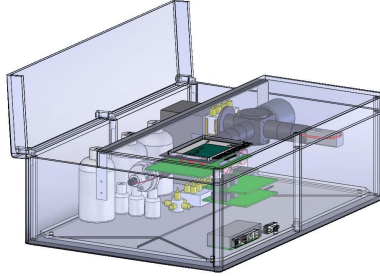
Figure D.1: Conceptual drawing of integrated NANODETECT prototype showing how the cover could be open by users to change microfluidic devices, fill up empty bottles or to carry out all necessary adjustments.
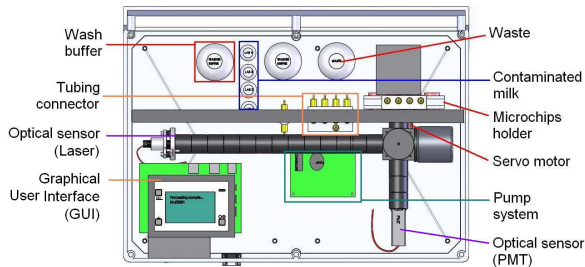
Figure D.2: Drawing of the top view of the prototype. This image represents required position of all components including the position between the optical sensor and microchip holder. As shown in this picutre, the mirochip holder must be placed in front of the optical sensor as close as possible to enhance measurement sensitivity.
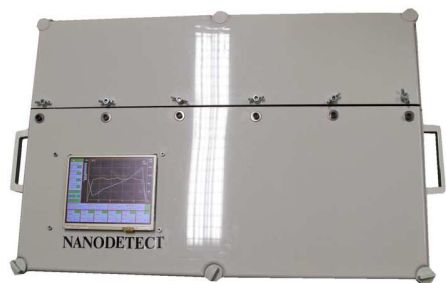
Figure D.3: Photo of the top view of the prototype (first design).
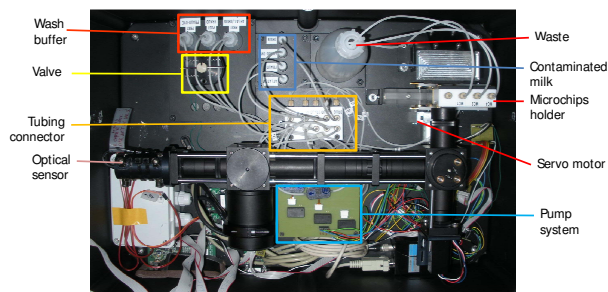
Figure D.4: Photo of the inside view of the prototype (first design).

D.1 Post Processing in the Optical System

PMT post processing

PMT signals had values from 0 to 4095 in arbitrary units (u.a.) representing measured fluorescent signals. The non-uniform signal was improved by two parameters such as *integration time* and *dead time* having units as $\frac{1}{100}$ m sec. The integration time specified the time, in which PMT read the fluorescent signal from the sample. When reading sequence was finished, PMT waited for an additional time specified in dead time. In this time, the detector was not active and gave no response to a second incident. During the measurement of the fluorescent signal, reading sequence was repeated with constant *integration time* and *dead time* for $10 - 15$ sec. In order to simply the process, the integration and dead time parameters were so selected that the sum of both values was always 0.5 sec. Another characteristic to be considered was the relationship between the integration time and PMT output, which had always a linear behavior [Cig11].

In order to get small fluctuations and thus obtain accurate measurement results, the integration and dead time parameters were properly set. The setting of the integration and dead time parameters was individually performed, because each sample presents different background fluorescence intensity. Consequently, every measurements were carried out in two stages. In the first stage, sample fluorescence was roughly evaluated using some default integration and dead time values, which must be low enough in order to avoid the damage of the PMT. However, integration and dead times values must be high enough to get measurable signals. Based on the default integration time and approximated first PMT output value, the new integration time value was computed and used in the second stage, in which real measurements were obtained. The following equations describe the whole measurement process, defining each of the variables and describing the effects and errors that might cause uncertainty in the final measurement. As mentioned previously, a linear dependence between integration time parameter and PMT output value as follows:

$$t_{int} = K \cdot I_{PMT} \tag{E.1}$$

being t_{int}, integration time value; I_{PMT}, PMT output signal and K, a constant. Using equation E.1, rough integration time values (t_{int1}) and PMT output average (I_{PMT1}) were obtained. Under the same conditions, the new integration time parameter t_{int2} was calculated assuming ideal condtions, in which PMT

output value (I_{PMT2}) should be 4095. According to these assumptions, new linear equations were established.

$$t_{int1} = K \cdot I_{PMT1} \quad and \quad t_{int2} = K \cdot I_{PMT2} \tag{E.2}$$

Using the last equation, it follows that:

$$K = \frac{t_{int1}}{I_{PMT1}} = \frac{t_{int2}}{I_{PMT2}} \tag{E.3}$$

and subsequently, corrected PMT output signal can be obtained as follows:

$$I_{PMT2} = I_{PMT1} \cdot \frac{t_{int2}}{t_{int1}} \tag{E.4}$$

Photodiode post processing

The excitation laser was an another important aspect in the design of the optical system, which influences significalty the measurement result. In order to obtain accure measurement results, the excitacion laser must be stabilized appliying a post processing method based on the measurement of laser intensity. The excitation laser intensity was measured by using a photodiode connected to a second RS232 port. The laser intensity value was between 0 and 1023 in arbritary units. This measurement was performed simultaneously to the fluorescense measurement, meaning that for every PMT output value, an excitation laser intesity value was also stored.

First, PMT output signals were corrected by exciting laser light intesity values to compensate laser fluctuation during the measurement and thus obtain direct comparability of PMT output values from different measured samples [Cig11]. Linear behavior between the laser intensity light and PMT output value was also assumed.

$$I_L = C \cdot I_{PMT} \tag{E.5}$$

where (I_L) is the excitation laser light intesity; (I_{PMT}) output values from the PMT and C a numerical constant. From the last equation,

$$I_{L1} = C \cdot I_{PMT1} \quad and \quad I_{L2} = C \cdot I_{PMT2} \tag{E.6}$$

being C,

$$C = \frac{I_{L1}}{I_{PMT1}} = \frac{I_{L2}}{I_{PMT2}} \qquad (E.7)$$

and afterward, corrected PMT output signal is obtained as indicated in following equation.

$$I_{L2} = I_{L1} \cdot \frac{I_{PMT2}}{I_{PMT1}} \qquad (E.8)$$

E.1 Immunoassay Protocols

Following information was taken from the Deliverable Report D06 of the NANODETECT project.
D06: Protocols for the different immunoassays.

NANODETECT

Project full title: Development of nanosensors for the detection of quality parameters along the food chain

Project Acronym: NANODETECT

Project No.: 211906

Instrument: Small Collaborative Project

Start Date: 1st September 2008
Duration: 36 Months

Deliverable Report
D06:   Protocols for the different immunoassays

Due date of deliverable:	08th October 2010
Submission date:	31st August 2010
File name:	NANODETECT_D06
Revision number:	
Save date:	
Document status:	Final[1]
Dissemination level:	CO[2]

---

[1] Document will be a draft until it was approved by the coordinator
[2] PU: Public, PP: Restricted to other programme participants (including the Commission Services), RE: Restricted to a group specified by the consortium (including the Commission Services), CO: Confidential, only for members of the consortium (including the Commission Services)

Role	Name	Organisation	Date	File suffix
Author	Andrea Mückl	TTZ	26/08/2010	AM
Co-Author	Caroline Hennigs	TTZ	26/08/2010	CH
	Willem Haasnoot	RIKILT	15/08/2010	WH
Task Leader	Caroline Hennigs	TTZ	26/08/2010	CH
WP leader	Caroline Hennigs	TTZ	26/08/2010	CH
Coordinator	Matthias Kück	TTZ	31/05/2010	MK

Table of Contents

1. Introduction

This deliverable provides the established protocols for quantitative detection of specific contaminants in raw milk.

Each assay was individually developed and optimized to fulfil the required detection limits. The assays are (currently) transferred to a microfluidic device and measured with an optical laser detection system.

For data processing and for calibration it is indispensable to perform the assay as standardized process. Therefore, the protocols are written to standardize laboratory methods and to ensure successful replication of results by others in the same laboratory.

The detailed protocols include a list of required equipment and instruments as well as information on safety items and the calculation of results, including statistical analysis for data interpretation.

Formulas may also be included for preparation of reagents and samples required for the work.

2. Task 2.1: Protocol for the pathogen detection unit (ttz)

-abandoned-

Since the assay does not fulfil required detection limits (8×10^3 instead of one cell in 25 g) and was not applied to the microfluidic device so far, the procedure is not presented here. According to European Commission, 3 of 4 devices have to work in the final offline NANODETECT system.

3. Task 2.2: Protocol for the mycotoxin detection unit (ttz)

-completed-

A direct binding inhibition assay was developed to detect aflatoxin M1 in untreated raw cow milk samples.

The fluorescence immunoassay (FIA) was successfully developed in the 96 well dishes and is currently transferred to the microfluidic device. Fluorescence microscopy revealed that immobilization of the antigen on SU-8 did not work sufficiently. However, this was successfully solved by increasing the hydrophilicity of the surface material. Due to this, optimizing the performance in the microfluidic device is delayed. Currently the results of this assay are evaluated with the optical laser detection system by Optotek.

The current detection limit in the microwell format is 0.08 ppb in 50 µl milk; however, in the microfluidic device the sensitivity can be further increased by applying a bigger sample volume which is planned for further optimization.

The assay principle is given in figure 3. R-phycoerythrin (R-PE) labelled anti-AFM1 antibody was pre-incubated with the free analyte. Remaining free R-PE antibody can bind to the immobilized antigen after application to the microwell.

Coating:	AFM$_1$–BSA hapten was immobilized on the MTP surface	
Blocking:	Free binding sites were blocked with 0.01 % BSA in PBS	
Washing:	Unbound BSA was washed away with TBS 0.05 % Tween® 20	
Sampling:	AFM$_1$ was added to 50 μl milk and blended with 50 μl R-PE labeled anti-AFM$_1$ antibody solution and added per well.	
Washing:	Free-AFM$_1$ bounded antibodies as well as R-PE was washed out with TBS 0.05 % Tween® 20	
Reading:	The remaining signal of solid-phase bounded antibodies in TBS 0.05 % Tween® 20 was measured at exc. 530 nm, em. 590 nm	

Figure 1: Principle of binding inhibition FIA for AFM1 detection: the assay involves six steps; the reaction requires 1 h.

Material

Chemicals

AFM$_1$-BSA (1 mg)	Art. No. A6412, Sigma-Aldrich GmbH, Munich
AFM$_1$ (5 µg)	Art. No. A6428, Sigma-Aldrich GmbH, Munich
BSA	Art. No. A3294, Sigma-Aldrich GmbH, Munich
Ceric(IV) ammonium nitrate	Art. No., Sigma-Aldrich GmbH, Munich
KCl	Art. No. P017.1, Carl Roth GmbH & Co KG, Karlsruhe
KH$_2$PO$_4$	Art. No. 104873, Merck KGaA, Darmstadt
NaCl	Art. No. 106404, Merck KGaA, Darmstadt
Tween 20	Art. No. A44112, Sigma-Aldrich GmbH, Munich
Tris	Art. No. 4855.1, Carl Roth GmbH & Co KG, Karlsruhe
Anti-AFM1 antibody*	BIOCULT, Leiden, the Netherlands
R-Phycoerythrin (R-PE)	Art No. PK-PF-RPE-05, PromoCell

*Labelled according to Hardy (1986) with R-PE.

<u>Laboratory equipment and consumables</u>

Axioskop 40 (AxioVision 4.6.3 Release Software)	Carl Zeiss, Jena
Glass slide **providing a dark underground**	Laboratory
PharmaMed Ismaprene 2-stop tubes (ID 1.52 mm)	Medchrom GmbH, Flörsheim-Dalsheim
Teflon-block	IMSAS, Bremen
Microfluidic chips (PMMA/SU-8)	IMSAS, Bremen
Microtiter plate (MTP) reader, Synergy HT, KC4 Version 3.0 with PowerReports™	BIO-TEK® Instruments GmbH, Bad Friedrichshall
Peristaltic pump, Minipuls Evolution	Gilson, Middleton USA
Rocking shaker S4 SkyLine	ELMI, Latvia
Aluminium foil	Local store

<u>Preparations</u>

SU-8 blocking buffer, pH 7.4	2 % (w/v) BSA in PBS
MTP blocking buffer, pH 7.4	0.01 % (w/v) BSA in PBS
PBS buffer, pH 7.4 (in 1 L dist. H_2O)	8 g NaCl
	0.2 g KCl
	1,44 g Na_2HPO_4
	0.24 g KH_2PO_4
TBST buffer, pH 7.5 (in 1 L dist. H_2O)	6.057 g Tris
	8.77 g NaCl
	500 µL Tween 20

Aflatoxin standards

- 5 µg AFM1 were dissolved in 500 µL Methanol (= stock solution, 10.000 ng/mL).
- Standard series were prepared in raw milk with concentrations ranging from 100 to 0.001 ng/mL

AFM$_1$-BSA coating

- 1 mg AFM1-BSA was dissolved in 1 mL PBS (= stock solution, 1 mg/mL)
- For a 4 mol AFM1 / mol BSA conjugate, 2 µg/mL coating solution was prepared in PBS.

R-PE anti-AFM1 IgG

- R-PE labelled antibody was applied in an end concentration of 10 µg/mL.
- A 20 µg/ml working solution was prepared in PBS and 1 : 2 blended with the AFM1 standard samples.
- Before application, the samples were vortexed and pre-incubated in the dark for 15 min.

SU-8 activation solution

- 10 % (w/v) ceric(IV) ammonium nitrate in 4 % (v/v) acidic acid

## Binding inhibition fluorescence immunoassay in the microwell format

Method

- 100 µL of AFM1–BSA conjugate were added to each. For blank values, 100 µL of MTP blocking buffer were applied.
- The plate was incubated at 37 °C for 1 h covered with aluminium foil.
- AFM1–BSA conjugate was removed with a pipette.
- 200 µL of MTP blocking buffer were applied with a multichannel pipette to each well and blocked for 1 h at 25 °C.
- Blocking buffer was removed and each well was washed twice with 200 µL TBST buffer using a multichannel pipette.
- Afterwards the plate was dried by turning it upside down on a paper towel.
- The samples were finally applied and incubated for 1 h on a rocking shaker (50 rpm, d = 8) in the dark.
- In the following step, the plate was washed 6 times as described above.
   Note: After adding the washing buffer, the plate was shaken 5 s by hand, and then the washing buffer was smoothly removed with the same pipette tips as used for adding. Pipetting off was started at the blank wells and continued to the next higher concentration. Tips were changed after each step.
- 200 µL TBST buffer was finally added to each well.
- The fluorescence signal was measured with the MTP-reader
   Programme KC4 was opened:

   WIZARD was selected in the browser and READING PARAMETERS opened
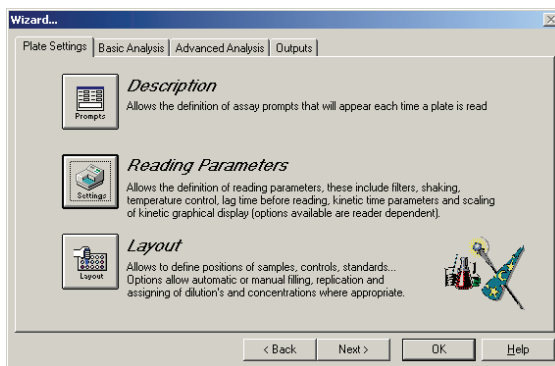
   FLUORESCENCE was check marked and excitation wavelength set to 530 nm and emission wavelength to 590 nm.
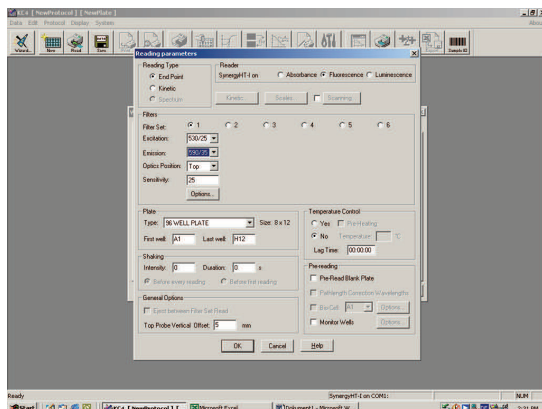
OPTIONS was pressed and "Automatic Sensitivity Adjustment" check marked. The HIGH WELLS field was check marked and the well in which the highest signal was expected, entered e.g. G1 (for 0 ppb AFM1 sample).
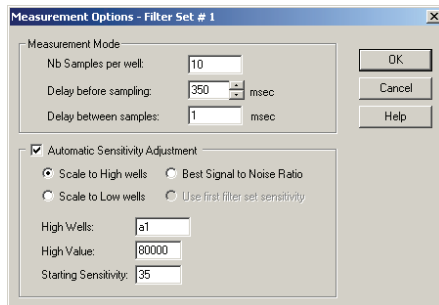
LAYOUT was selected and the wells for determination marked as following:

All WIZARD settings were confirmed and the READ-button in the browser pressed.

⇨ START READING and insert the plate was selected.

Evaluation (with Microsoft Excel)

- Arithmetic means and standard deviations (SD) as well as relative standard deviations (RSD) of each AFM1 concentration (triplet determinations) and for blank values were calculated (compare table 1)
- Blank values were subtracted and the data normalized to the highest signal obtained (analyte free sample).

Table 1: Example for data evaluation

AFM1 [ppb]	Mean μ	SD σ	RSD σ[*] [%]	Value	Value [%]
100	38778.500	644.174	1.661	851.500	2.085
10	52231.000	2409.820	4.614	14304.000	35.031
1	63473.500	2211.123	3.484	25546.500	62.564
0.1	71976.000	1934.644	2.688	34049.000	83.387
0.01	76728.500	3261.884	4.251	38801.500	95.026
0.001	78759.500	2174.353	2.761	40832.500	100.000
0	74683.000	2074.651	2.778	36756.000	90.017
Blank	37927.000	1185.111	3.125	0.000	0.000

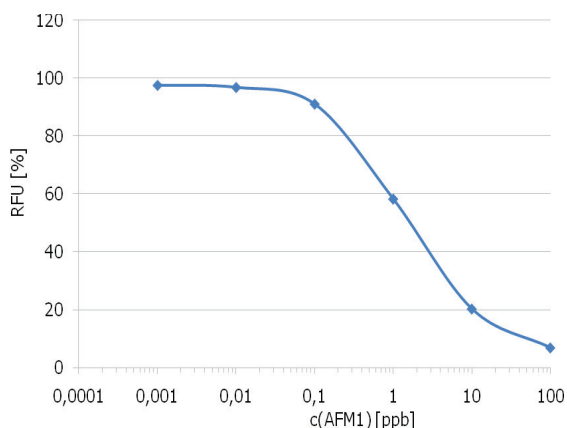- Graphics were plotted as shown in figure 4:

Figure 2: Dose-response curve in the microwell format

Figure 4 shows the assay performance in the microwell format. The detection limit was 0.08 ppb AFM1 in 50 µl milk.

Binding inhibition fluorescence immunoassay in the microfluidic device

Method

- Chips were put into a Petri dish and 10 µL of SU-8 activation solution were added with a pipette. Incubation was carried out for 1 h at RT.
- Chips were rinsed with distilled water and dried at 37 °C.
- AFM1–BSA conjugate was applied to the inlet of a chip (see fig. 5) and incubated at 4 °C over night. The Petri dish was saturated with water soaked tissues next to the chips to keep a hydrated atmosphere. For blind value ~ 10 µL of blocking buffer were applied to the chip.
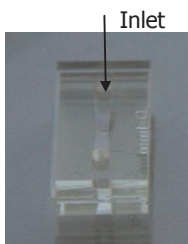
Figure 3: Chip with microchannel and inlet opening

- AFM1–BSA conjugate was carefully removed and the chips were filled with blocking buffer as done with coating solution and blocked for 2 h at room temperature.
- The blocking buffer was removed and each chip was put into the holder of the microfluidic device to accomplish the washing step (figure 5).
-
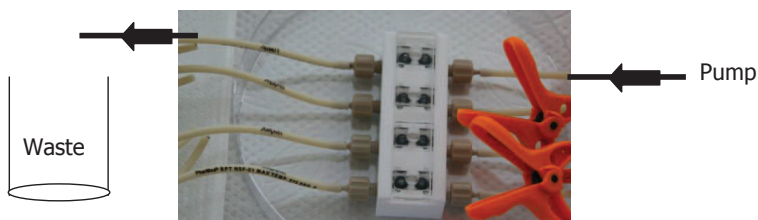
Figure 4: Experimental setup of a 4 channel microfluidic device containing 4 chips.

- Each chip was washed (with TBST) with 0.5 mL/min. (2 mL in total) in parallel progression.
- The chips were loaded with the samples (0.5 mL/min.) and incubate for 1 h at room temperature covered with aluminium foil to prevent the samples from light.
- The chips were washed as described above

- After the washing step, the chips were removed from the microfluidic device and dried with **slight** air pressure (see fig. 7)

Figure 5: Drying the chip with air pressure

- The assay performance was controlled with a fluorescence microscop
- The settings were 5x objective, green filter unit and object slide providing **a dark underground** (compare fig. 8).
- Image acquisition occurred with 15 s shutter speed.

Figure 6: Fluorescence image acquisition of a chip

Results and conclusion

The following figure 9 presents the fluorescence acquisition series with fluorescence microscopy from the inlet to the outlet of a non-contaminated chip. Fluorescence intensity was strong which was expected for the non-contaminated sample after surface activation. Therefore the assay principle was successfully transferred to the microfluidic device. Since we cannot quantify fluorescence intensity, chips with standard samples were sent to Optotek for quantitative laser detection. Results will be expected in month 26.
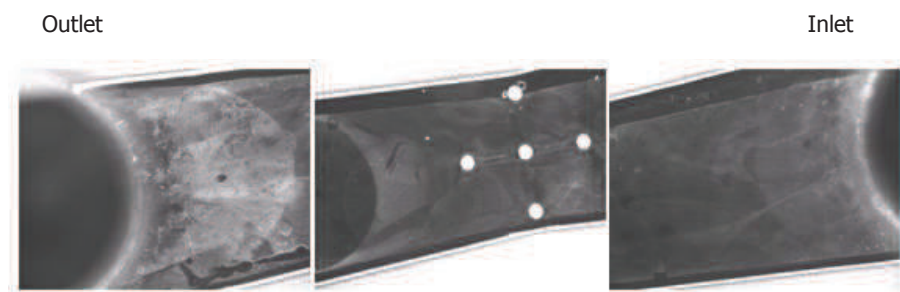
Outlet   Inlet

Figure 7: Fluorescence images of a chip from the inlet to the outlet of a non-contaminated sample

4. Task 2.3: Protocol for the drug residue detection unit (RIKILT)

-partly finished-

Sandwich immunoassay for the detection of drug residue

Protein-drug conjugates were prepared for coupling to the sensor surface and the monoclonal antibodies were labelled with the fluorophore R-phycoerythrin (PE) and/or Alexa. These reagents were tested for their quality and performance in buffer and milk in the Luminex system which uses protein-drug conjugates coated beads and the fluorescent labelled antibodies. These results will be used to transfer the application to the final prototype of the NANODETECT device.

RIKILT used the Luminex100 flow cytometer in combination with the Multi Analyte Profiling (xMAP) technology. This system is closest to the theoretical design of the NANODETECT system which is also based on fluorescence detection using the fluorescent protein R-phycoerythrin (PE). The xMAP technology uses small carboxylated polystyrene microspheres (5.6 µm beads), which are internally dyed with a red and an infrared fluorophore. By varying the ratio of the two fluorophores, up to 100 different color-coded bead sets can be distinguished, and each bead set

can be coupled to a different biological probe. In combination with flow cytometry, it is possible to simultaneously measure up to 100 different biomolecular interactions in a single well. The carboxylated bead surface allows simple chemical coupling of capture reagents such as antibodies or drug-protein conjugates. The binding of PE-labeled antibodies to the beads can be measured by the fluorescence intensities. In the following experiments, the relatively new magnetic beads of Luminex (MagPlex) were used, because they are easier to work with.

Material

The following primary antibodies were successfully applied:

(Dihydro)streptomycin (Mab F62)

Gentamicin (Pab 422)

Sulfonamides (Mutant M.3.4)

Protein-drug conjugates were prepared for coupling to the Luminex beads, and later on to the NANODETECT sensor surface.

Following secondary antibodies were used for detection:

Goat anti-mouse (GAM) labelled with R-PE

Goat anti-rat (GAR) labelled with R-PE

Streptavidin labelled with R-PE (SAPE)

Method

Protocol for drug residues:

40 µl sample + 10 µl Mab in 5x PBSAT

10 min incubation +

1000 beads in 10 µl (1x PBSAT)

30 min incubation and wash

+ 70 µl reporter 1x PBSAT)

15 min incubation and wash

+ 70 µl PBS

Measure 100 beads

Figure 8: Optimized protocol for the Luminex100 flow cytometer to prepare calibration curves of the drug residues in the inhibition immunoassay format using drug-protein coated magnetic beads and bound antibodies are detected with a second antibody labeled with PE. 5xPBSAT is 5x concentrated PBS buffer with the addition of BSA (0.5 %) and Tween-20 (0.05 %).

Results and conclusion

(Dihydro)streptomycin

The affinity purified and concentrated batch of Mab F62 could be used in a 64000 times dilution (320000 final dilution in the well) and the reporter antibody (goat anti-mouse (GAM)-PE) was diluted 700 times in combination with the protocol as described in Figure 9. Under these conditions, the calibration curves for streptomycin in buffer and diluted goats' milk are shown in Figure 11. The observed matrix effect resulted in a higher sensitivity in diluted milk compared with the curve in buffer. With this assay, streptomycin and dihydrostreptomycin can be detected at levels above 10 ng/ml in 10 times diluted milk which is sensitive enough to control at the Maximum Residue Limit (MRL) level of 200 µg/L in milk.

	Buffer	1/10x geit
IC50	59.63	27.95

Figure 9: Calibration curves of streptomycin in the Luminex100 flow cytometer in the inhibition immunoassay format using streptomycin-BSA coated magnetic beads in combination with Mab F62 (newest batch) and GAM labeled with PE for the detection. Calibration curves were prepared in buffer and in 10 times diluted goat's milk.

Gentamicin

With this Pab, gentamicin can be detected at the MRL using ten times diluted milk samples (figure 12).

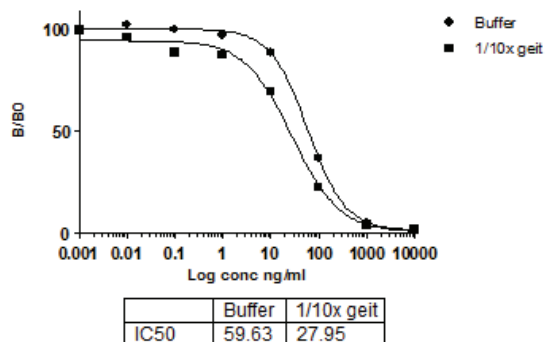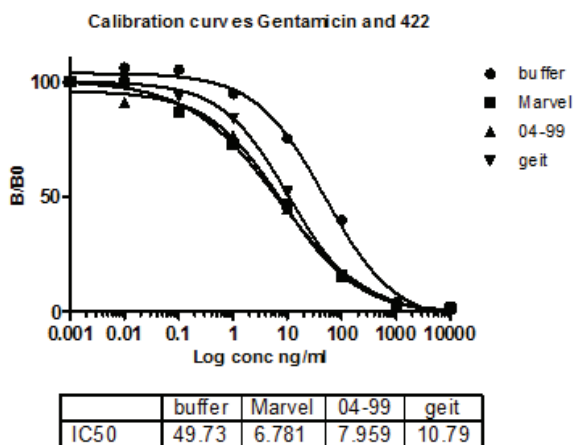|	buffer	Marvel	04-99	geit
IC50	49.73	6.781	7.959	10.79

Figure 10: Calibration curves of gentamicin in the Luminex100 flow cytometer in the inhibition assay format using gentamicin-BSA coated magnetic beads in combination with Pab 422 and GAR labeled with PE for the detection. Calibration curves were prepared in buffer and in 10 times diluted milk samples.

19

Sulfonamides

Mutant M.3.4 was used in combination with beads towards the sulfonamide derivative (TS), used as hapten, was coupled directly (without a protein). This mutant is biotinylated and streptavidin-PE (SAPE) was used as reporter. Results obtained with this mutant were shown in (Figure 13).

Figure 11: Calibration curves of sulfathiazole in the Luminex100 flow cytometer in the inhibition immunoassay format using the mutant (M.3.4) anti-sulfonamide antibodies and TS-coated magnetic beads and SAPE for the detection. Calibration curves were prepared in buffer and in 10 times diluted cows' milk.

The measurement ranges of the calibration curves for sulfathiazole in buffer ranged from 1 to 10 ng/ml for the mutated recombinant antibody (Figure 13). This sensitivity was reported before in a biosensor-based assay (Bienenmann-Ploum et al. (2005)). The calibration curves in 10 times diluted cows' milk showed improved sensitivities which still have to be evaluated.

For sulfamethoxazole, the measurement range of the calibration curve in buffer ranged from 1 to 100 ng/ml (Figure 14), which is comparable with the performance in the biosensor immunoassay (Bienenmann-Ploum, M. (2005)). Also here, the calibration curve in diluted milk showed an improved sensitivity.
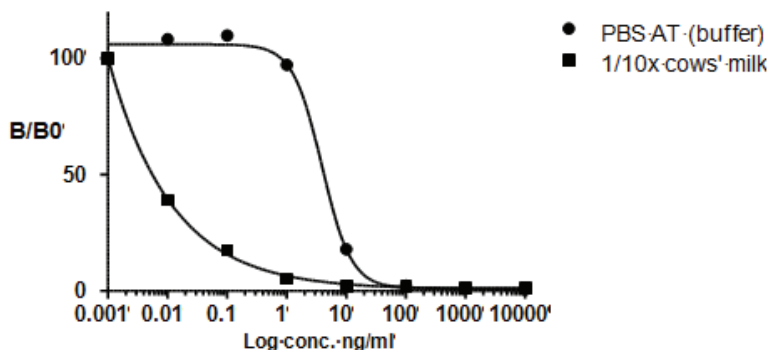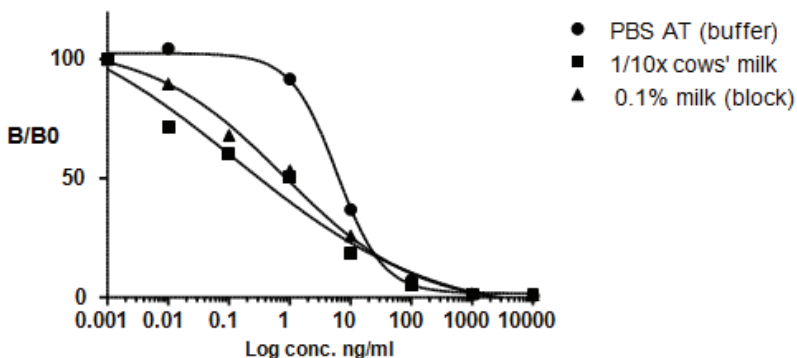
Figure 12: Calibration curves of sulfamethoxazole in the Luminex100 flow cytometer in the inhibition assay format using the mutant (M.3.4) multi-sulfonamide antibodies in combination with TS-coated magnetic beads and SAPE for the detection. Calibration curves were prepared in buffer, in 10 times diluted cows' milk and in a buffer containing 0.1 % cows' milk.

From the two model systems for drug residue detection ((dihydro)streptomycin, gentamicin and sulfonamides), three different immunoassays were demonstrated to work in the Luminex system under the conditions proposed and proved to be sensitive enough for the detection at or below the Maximum Residue Limits (MRL's) in milk. Experiments on SU-8 were not (yet) performed with the drug tests because the results cannot be quantified in the present detection system using microarray scanner. The assay will be transferred to the final prototype expected in month 26.

5. Task 2.4: Protocol for the fraud detection unit (RIKILT)

-completed-

Sandwich immunoassay with the NANODETECT microfluidic device

A quantitative sandwich immunoassay was developed to detect 2 % cow milk in goat milk:

Material

- PMMA-SU-8 (2 mm) fluidic devices   IMSAS, Bremen
- Peristaltic pump, Minipuls 3   Gilson, Middleton USA
- Ethanol
- Phosphate buffered saline (PBS)

21

- Phosphate buffered saline with 0.05 % Tween-20 (PBST)
- Monoclonal antibody 6A10/Alexa 532
- Samples
    1. 100 % cow's milk

    2. 50 % cow's milk

    3. 10 % cow's milk

    4. 2 % cow's milk

    5. 100 % goat's milk

Experimental setup
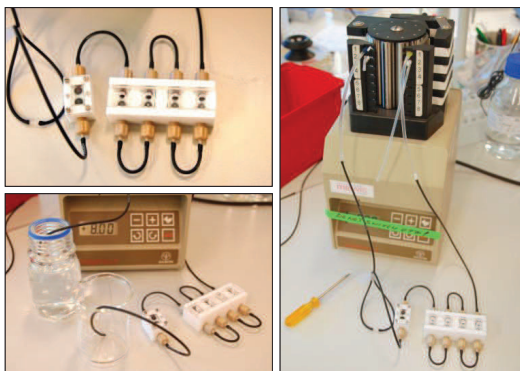
a: Serial connection
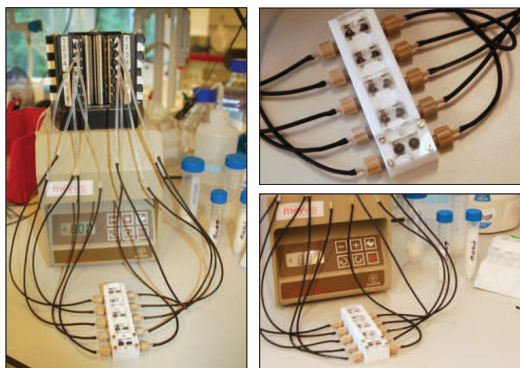
b: Parallel connection

Figure 13: The NANODETECT device with 5 slides used in RIKILT in serial (a) and parallel (b) connections.

Method

- The 2 mm fluidic devices from the remaining diameters (1 mm, 2 mm and 4 mm) were chosen.
- The slides were placed in the fluidic device (figure 1) and washed with ethanol in the serial setting (Figure 1a) for 10 minutes.
- The slides were then washed with water for 10 minutes in serial setting and after that another 10 minutes with PBS.
- 100 µl of Mab6A10 was added to 1900 µl of PBS and 1.7 ml was introduced into the serial fluidic device setting. Then the inlet and outlet were connected to make the serial system circular and the solution was pumped around overnight at room temperature.
- The serial setting was made parallel again and the device was washed and blocked using PBST-BSA for 60 minutes.
- The buffer was switched to PBST and the slides were washed for 10 minutes.
- With the connections in parallel, the different samples were introduced in each slide. The tubing was then made circular and the samples were pumped around for 2 hours.
- The samples were then drained from the slides and the system was washed in parallel with PBST still in parallel setting for 15 minutes.
- The system was made serial again and washed with PBS for 5 minutes.
- Mab4G10/Alexa 532 conjugate (20 µl) was added to 1980 µl of PBS. This was introduced in the system (1.7 ml) and pumped around for 1 hour.
- The non-bound label was drained from the slides and the system was washed in parallel setting with PBST in serial setting for 15 minutes.
- The system was washed with PBS for 10 minutes.
- The system was washed with double distilled water for 10 minutes.
- The slides were taken out of the device and the remaining double distilled water was removed from the slides with pressured air. The slides were ready for measurement and send to Optotek.

Results and conclusion

Slides were sent to Optotek and the measurement results are shown in Figure 2.
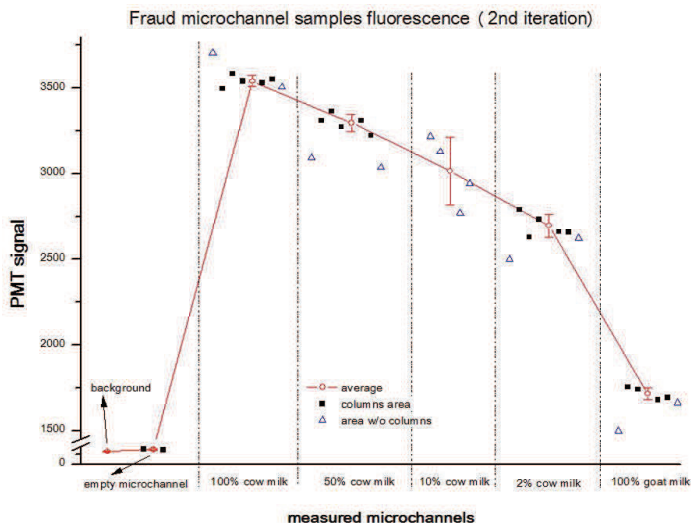
Figure 14: Dose-response curve of the fraud unit as obtained at Optotek.

Apart from the 10/90 % point, the individual cow/goat milk concentrations points are well defined and comfortably detected. "White spot", however, can cause problems and preventing it happening would improve the results even further.

We can confidently detect 2 % or more cow milk in goat milk (figure 2), that's why the measurement can be considered successful.

References

Bienenmann-Ploum, M., Korpimäki, T., Haasnoot, W., Kohen, F. (2005) Comparison of multi-sulfonamide biosensor immunoassays Analytica Chimica Acta, 529, 115-122

Hardy, RR (1986) Purification and coupling of fluorescent proteins for use in flow cytometry, Handbook of Experimental Immunology, 4th ed. DM Weir, LA Herzenberg, C Blackwell, and LA Herzenberg, editors. Blackwell Scientific Publications, Boston, 31.1-31.12

Bibliography

[AJJ+09]   Ye Ai, Sang W. Joo, Yingtao Jiang, Xiangchun Xuan, and Shizhi Qian. Pressure-driven transport of particles through a converging-diverging microchannel. *Journal of Biomicrofluidics*, 3(1), 2009.

[ASI+06]   Takahiro Arakawa, Yoshitaka Shirasaki, Toshimitsu Izumi, Tokihiko Aoki, Hirokazu Sugino, Takashi Funatsu, and Shuichi Shoji. High-speed particles and biomolecules sorting microsystem using thermosensitive hydrogel. *Measurement Science and Technology*, 17(12):3141, 2006.

[Bar10]   Bartels Mikrotechnik GmbH - Emil-Figge-Str. 76a - D-44227 Dortmund, www.bartels-mikrotechnik.de/. *Bartels Mikrotechnik GmbH*, July 2010.

[BCP+98]   Gianpiero Boatto, Riccardo Cerri, Amedeo Pau, Michele Palomba, Giorgio Pintore, and Maria Giovanna Denti. Monitoring of benzylpenicillin in ovine milk by hplc. *Journal of Pharmaceutical and Biomedical Analysis*, 17(4-5):733–738, August 1998.

[Bec11]   Beckman Coulter, www.beckmancoulter.com. *Milk fat size distribution by laser difraction*, Jan 2011.

[BHH05]   Adam Bange, H. Brian Halsall, and William R. Heineman. Microfluidic immunosensor systems. *Biosensors and Bioelectronics*, 20(12):2488 – 2503, 2005. 20th Anniversary of Biosensors and Bioelectronics.

[BKJ+08]   Gabriela Blagoi, Stephan Keller, Alicia Johansson, Anja Boisen, and Martin Dufva. Functionalization of su-8 photoresist surfaces with igg proteins. *Applied Surface Science*, 255(5, Part 2):2896 – 2902, 2008.

[BL02]   Holger Becker and Laurie E. Locascio. Polymer microfluidic devices. *Talanta*, 56(2):267 – 287, 2002.

[BS10]   Jean Berthier and Pascal Silberzan. *Microfluidics for Biotechnology.* December 2010.

Bibliography

[BY97]   James P. Brody and Paul Yager. Diffusion-based extraction in a microfabricated device. *Sensors and Actuators A: Physical*, 58(1):13 – 18, 1997. Micromechanics Sections of Sensors and Actuators.

[BYGA96]   J.P. Brody, P. Yager, R.E. Goldstein, and R.H. Austin. Biotechnology at low reynolds numbers, December 1996.

[CCC⁺04]   Ren-Kun Chen, Li-Wen Chang, Ya-Yun Chung, Ming-Hsung Lee, and Yong-Chien Ling. Quantification of cow milk adulteration in goat milk using high-performance liquid chromatography with electrospray ionization mass spectrometry. *Rapid Communications in Mass Spectrometry*, 18(10):1167–1171, 2004.

[CCLL08]   Xing Chen, Da Fu Cui, Chang Chun Liu, and Hui Li. Microfluidic chip for blood cell separation and collection based on crossflow filtration. *Sensors and Actuators B: Chemical*, 130(1):216 – 221, 2008. Proceedings of the Eleventh International Meeting on Chemical Sensors IMCS-11 - IMCS 2006, IMCS 11.

[CCS⁺02]   Jimmy D. Cox, Mark S. Curry, Stephen K. Skirboll, Paul L Gourley, and Darryl Y. Sasaki. Surface passivation of a microfluidic device to glial cell adhesion: a comparison of hydrophobic and hydrophilic sam coatings. *Biomaterials*, 23(3):929 – 935, 2002.

[Cig11]   Anze Cigoj. Nanodetect fluorescence detector, measurement and post processing. Technical report, NANODETECT project. OPTOTEK d. o. o., Laser and optical technology, Febraury 2011.

[Cop10]   Copyright © 2011 BioChem Fluidics. *Solenoid Operated Pinch Valves Brochure*, September 2010.

[Dow10]   Dow Corning Corporation, ©2000 - 2010, www.dowcorning.com/. *Dow Corning*, October 2010.

[dSdO01]   Mauris N. de Silva, Ravi desai, and David J. Odde. Micropatterning of animal cells on pdms substrates in the presence of serum without use of adhesion inhibitors, 2004-09-01.

[DSM09a]   A. Deepu, V. Sai, and S. Mukherji. Simple surface modification techniques for immobilization of biomolecules on su-8. *Journal of Materials Science: Materials in Medicine*, 20:25–28, 2009. 10.1007/s10856-008-3471-9.

[DSM+09b]   WLODKOWIC Donald, FALEY Shannon, ZAGNONI Michele, WIKSWO& John P., and COOPER Jonathan M. Microfluidic single-cell array cytometry for the analysis of tumor apoptosis, 2009. Anglais.

[DTV08]   Salil P. Desai, Brian M. Taff, and Joel Voldman. A photopatternable silicone for biological applications. *Langmuir*, 24(2):575–581, 2008. PMID: 18081333.

[eH99]   Mohamed Gad el Hak. The fluid mechanics of microdevices—the freeman scholar lecture. *Journal of Fluids Engineering*, 121(1):5–33, 1999.

[Evo10]   Evonik Industries AG, corporate.evonik.de. *Evonik Industries AG*, October 2010.

[Fis04]   Susanne Blüml; Sven Fischer. *Handbuch der Fülltechnik: Grundlagen und Praxis für das Abfüllen flüssiger Produkte.* 2004.

[Fra04]   Sami Franssila. *Introduction to Microfabrication*. Wiley; 1 edition, 1 edition, 2004.

[Fra10]   Fraunhofer IFAM, Copyright © by Fraunhofer Gesellschaft, www.ifam.fraunhofer.de. *Fraunhofer IFAM*, October 2010.

[FVSD01]   A. Freitag, D. Vogel, R. Scholz, and T.R. Dietrich. Microfluidic devices made of glass. *Journal of the Association for Laboratory Automation*, 6(4):45–49, September 2001.

[GB95]   H. Gourama and B. Bullerman. Aspergillus flavus and aspergillus parasiticus : aflatoxigenic fungi of concern in foods and feeds : a review. *International Association for Food Protection*, 58(12), 1995. Anglais.

[GH06]   S. A. Guelcher and J. O. Hollinger. *An Introduction to Biomaterials.* Taylor & Francis Group, LLC, 2006.

[GKA+09]   James V. Green, Tatiana Kniazeva, Mehdi Abedi, Darshan S. Sokhey, Mohammad E. Taslim, and Shashi K. Murthy. Effect of channel geometry on cell adhesion in microfluidic devices. *Lab Chip*, 9(5):677–685, 2009.

[Gmb]   ATTO-TEC GmbH. Quenching method. E-mail received from the company ATTO-TEC GmbH. September 2009.

[GSC+09]   Claudia Garcia, Anna Lena Schomacker, Anze Cigoj, Andrej

Vrecko, Carsten Harms, and Walter Lang. Polymer vitralit® uc6772 used as support material to detect low levels of protein concentration. In *MMB2011 Conference 2011 Lucerne (Switzerland). 6th International Conference on Microtechnologies in Medicine and Biology. MMB 2011 Proceedings pp. 54-55, 4-6 May 2011*, May 2009.

[GSF+12]   Claudia Garcia, Kai Syrnik, Anja Feyen, Anna Lena Schomacker, Carsten Harms, and Walter Lang. Fabrication of disposable microfluidic devices for monitoring fluid samples. In *MSB 2012, 27th International Symposium on MicroScale Bioseparations and Analyses, Geneva (Switzerland), 12-15 February 2012. Eingereicht am 21. Oktober 2011, Angenommen am 23. November 2011.*, Feb 2012.

[GSK+09]   Claudia Garcia, Anna Lena Schomacker, Ingo Klarholz, Carsten Harms, and Walter Lang. Fabrication of microfluidic devices using su-8 for detection and analysis of viruses. In *SENSOR + TEST Conference 2009 Nürnberg (Germany). 14th International Conference on Sensors,. Technologies, Electronics and Applications. SENSOR 2009. Proceedings Sensor Vol. 1 pp.193-197, 26-28 May 2009*, May 2009.

[GSSM11]   Aakash Golia, Pankaj Kumar Sahu, Ashis Kumar Sen, and P Muthukumar. Investigations of a micro-mixer with and without indentations along the mixing channel. *Proceedings of the ASME 2011 International Mechanical Engineering Congress & Exposition IMECE2011*, (1), 2011.

[GVS10]   Claudia Garcia, Andrej Vrecko, and Anna Lena Schomacker. Milestone report m3.2 assessment of the chemical, physical, biological and technical needs. Technical report, NANODETECT project. OPTOTEK d. o. o., Laser and optical technology, 2010.

[HAM]   HAMAMATSU PHOTONICS K.K., Electron Tube Division, 314-5, Shimokanzo, Iwata City, Shizuoka Pref. 438-0193, Japan. *Photodiode Technical Information*.

[HAM07]   HAMAMATSU PHOTONICS K.K., Electron Tube Division. *Photomultiplier Tube. Basics and Applications*, third edtion (edition 3a) edition, 2007.

[HBO03]   Dirk Hegemann, Herwig Brunner, and Christian Oehr. Plasma treatment of polymers for surface and adhesion improvement.

Nuclear Instruments and Methods in Physics Research Section B: Beam Interactions with Materials and Atoms, 208:281 – 286, 2003. Ionizing Radiation and Polymers.

[HEX09]   HEXION TM, Speciatily Chemicals. *Data sheet Epoxy Resin 1002F*, 2009.

[HGL07]   Guoqing Hu, Yali Gao, and Dongqing Li. Modeling micropatterned antigen-antibody binding kinetics in a microfluidic chip. *Biosensors and Bioelectronics*, 22(7):1403 – 1409, 2007.

[Hil06]   Ulrich Hilleringmann.   *Mikrosystemtechnik. Prozessschritte, Technologies, Anwendungen*. Teubner, 1 edition, 2006.

[HKH⁺01]   Anson Hatch, Andrew Evan Kamholz, Kenneth R. Hawkins, Matthew S. Munson, Eric A. Schilling, Bernhard H. Weigl, and Paul Yager. A rapid diffusion immunoassay in a t-sensor. *Nat Biotech*, 19(5):461–465, May 2001.

[HMD⁺07]   G.C. Hill, R. Melamud, F.E. Declercq, A.A. Davenport, I.H. Chan, P.G. Hartwell, and B.L. Pruitt. Su-8 mems fabry-perot pressure sensor. *Sensors and Actuators A: Physical*, 138(1):52 – 62, 2007.

[HY03]   Kenneth R. Hawkins and Paul Yager. Nonlinear decrease of background fluorescence in polymer thin-films - a survey of materials and how they can complicate fluorescence detection in [small mu]tas. *Lab Chip*, 3(4):248–252, 2003.

[JFG⁺01]   Rebecca J Jackman, Tamara M Floyd, Reza Ghodssi, Martin A Schmidt, and Klavs F Jensen. Microfluidic systems with on-line uv detection fabricated in photodefinable epoxy. *Journal of Micromechanics and Microengineering*, 11(3):263, 2001.

[JOI01]   JOINT FAO/WHO FOOD STANDARDS PROGRAMME, CODEX ALIMENTARIUS COMMISSION, Twenty-fourth Session, Geneva, Switzerland, 2-7 July 2001, www.codexalimentarius.net.   *Codex alimentarius commission*, July 2001.

[Jos10]   Josef Weiss Plastic GmbH, copyright ©1997-2010, www.plexiweiss.de.   *Josef Weiss Plastic GmbH*, October 2010.

[JPRM07]   Manoj Joshi, Richard Pinto, V. Ramgopal Rao, and Soumyo

Mukherji. Silanization and antibody immobilization on su-8. *Applied Surface Science*, 253(6):3127 – 3132, 2007.

[Kir87]   Klaus Kirchner. *Chemical reactions in plastics processing.* Hanser, 1987.

[Kra05]   Egon Krause. *Fluid mechanics: with problems and solutions, and an aerodynamic laboratory.* Springer, 2005.

[Kue07]   Wolfgang Kuemmel. *Technische Stroemungsmechanik: Theorie und Praxis ; mit 36 Tabellen, 93 Praxishinweisen und 57 durchgerechneten Beispielen.* Teubner Lehrbuch. Teubner, Wiesbaden, 3., ueberarb. und erg. aufl. edition, 2007. XII, 346 S. : Ill., zahlr. graph. Darst.

[LC06]   Yong-Chien Ling and Richard K. Chang. Multiple-anode pmt makes possible the detection, discrimination, enrichment, and deposition of bioareosols on-the-fly. *Center for Laser Diagnostic, Department of Applied Physics, Yale University*, 2006.

[LJRW04]   Jessamine Ng Lee, Xingyu Jiang, Declan Ryan, and George M. Whitesides. Compatibility of mammalian cells on surfaces of poly(dimethylsiloxane). *Langmuir*, 20(26):11684–11691, 2004.

[LLCC02]   Che-Hsin Lin, Gwo-Bin Lee, Bao-Wen Chang, and Guan-Liang Chang. A new fabrication process for ultra-thick microfluidic microstructures utilizing su-8 photoresist. *Journal of Micromechanics and Microengineering*, 12(5):590, 2002.

[LSC01]   Peter B. Luppa, Lori J. Sokoll, and Daniel W. Chan. Immunosensors–principles and applications to clinical chemistry. *Clinica Chimica Acta*, 314(1-2):1 – 26, 2001.

[LTK05]   G. Liu, Y. Tian, and Y. Kan. Fabrication of high-aspect-ratio microstructures using su8 photoresist. *Microsystem Technologies*, 11:343–346, 2005. 10.1007/s00542-004-0452-x.

[MAB$^+$03] M.P. Molina, R.L. Althaus, S. Balasch, A. Torres, C. Peris, and N. Fernandez. Evaluation of screening test for detection of antimicrobial residues in ewe milk. *Journal of Dairy Science*, 86(6):1947 – 1952, 2003.

[Mad02]   M. J. Madou. *Fundamentals of microfabrication: the science of miniaturization.* CRC Press, Boca Raton, FL, 2 edition, March 2002.

[Mag11]   The Magazine for the Global Micro Manufacturing Technology Community, www.micromanu.com. *Micromanu*, May 2011.

[Men07]   W Menz. *Microsystem Technology*. December 2007.

[MF03]   W. E. Moerner and David P. Fromm. Methods of single-molecule fluorescence spectroscopy and microscopy, 2003.

[MFLA$^+$00] Cesar Mateo, Gloria Fernandez-Lorente, Olga Abian, Roberto Fernandez-Lafuente, and Jose M. Guisan. Multifunctional epoxy supports: A new tool to improve the covalent immobilization of proteins. the promotion of physical adsorptions of proteins on the supports before their covalent linkage. *Biomacromolecules*, 1(4):739–745, 2000. PMID: 11710205.

[MGP$^+$07] C. Mateo, V. Grazu, BC. Pessela, T. Montes, JM. Palomo, R. Torres, F. López-Gallego, R. Fernández-Lafuente, and JM. Guisan. Advances in the design of new epoxy supports for enzyme immobilization-stabilization. *7th International Conference on Protein Stabilization*, (4), 2007. PMID: 11710205.

[mic10a]   micro resist technology GmgH, Copyright©2003, www.microresist.de/. *micro resist technology*, Feb 2010.

[Mic10b]   MicroChem Corp., Copyright©2009, www.microchem.com/. *MicroChem Corporation*, July 2010.

[Mil10]   Miller Stephenson, Copyright © 2008, www.miller-stephenson.com. *Miller Stephenson*, October 2010.

[MML$^+$03] G. Medoro, N. Manaresi, A. Leonardi, L. Altomare, M. Tartagni, and R. Guerrieri. A lab-on-a-chip for cell detection and manipulation. *Sensors Journal, IEEE DOI - 10.1109/JSEN.2003.814648*, 3(3):317–325, 2003.

[MMS$^+$08] Laura Mercolini, Roberto Mandrioli, Bruno Saladini, Matteo Conti, Cesare Baccini, and Maria Augusta Raggi. Quantitative analysis of cocaine in human hair by hplc with fluorescence detection. *Journal of Pharmaceutical and Biomedical Analysis*, 48(2):456–461, September 2008.

[MNAA$^+$97] Randy M. McCormick, Robert J. Nelson, M. Goretty Alonso-Amigo, Dominic J. Benvegnu, and Herbert H. Hooper.

Microchannel electrophoretic separations of dna in injection-molded plastic substrates. *Analytical Chemistry*, 69(14):2626–2630, 1997.

[MR04]   Hans-Joachim Mueller and Thomas Roeder. *Der Experimentator: Microarrays.* Elsevier, Spektrum Akad. Verl., 2004.

[MSJ+06]   Rodolphe Marie, Silvan Schmid, Alicia Johansson, Louise Ejsing, Maria Nordström, Daniel Häfliger, Claus BV Christensen, Anja Boisen, and Martin Dufva. Immobilisation of dna to polymerised su-8 photoresist. *Biosensors and Bioelectronics*, 21(7):1327 – 1332, 2006.

[MTFL+03]   Cesar Mateo, Rodrigo Torres, Gloria Fernandez-Lorente, Claudia Ortiz, Manuel Fuentes, Aurelio Hidalgo, Fernando Lopez-Gallego, Olga Abian, Jose M. Palomo, Lorena Betancor, Benevides C. C. Pessela, Jose M. Guisan, and Roberto Fernandez-Lafuente. Epoxy-amino groups: A new tool for improved immobilization of proteins by the epoxy method. *Biomacromolecules*, 4(3):772–777, 2003. PMID: 12741797.

[MZH+09]   V. R. S. S. Mokkapati, L. Zhang, R. Hanfoug, J. Mollinger, J. Bastemeijer, and A. Bossche. Fabrication and testing of a tmmf s2030 based micro fluidic device for single cell analysis. pages 86–89, 2009.

[NBW06]   Yoonkey Nam, Darren W. Branch, and Bruce C. Wheeler. Epoxy-silane linking of biomolecules is simple and effective for patterning neuronal cultures. *Biosensors and Bioelectronics*, 22(5):589 – 597, 2006.

[NW05]   Nam-Trung Nguyen and Zhigang Wu. Micromixer review. *Journal of Micromechanics and Microengineering*, 15(2):R1, 2005.

[OJA05]   S.P. Oliver, B.M. Jayarao, and R.A. Almeida. Foodborne pathogens in milk and the dairy farm environment: Food safety and public health implications. *FOODBORNE PATHOGENS AND DISEASE*, 2(1):216 – 221, 2005. Proceedings of the Eleventh International Meeting on Chemical Sensors IMCS-11 - IMCS 2006, IMCS 11.

[Omn10]   Omnifit, Copyright © 2011 DIBA INDUSTRIES, www.omnifit.com/. *Omnifit*, October 2010.

[opt10]   *OPTOTEK d. o. o., Laser and optical technology.* www.optotek-medical.com, July 2010.

[Pan09]   Panacol-Elosol GmbH, Oberursel, Germany. *Data sheet Vitralit UC6772*, 2009.

[Pan10]   Panacol-Elosol GmbH, www.panacol.de/. *Panacol*, October 2010.

[PC01]   Yong-Le Pan and Richard K. Chang. Multiple-anode pmt behaves like many detectors in one. *LaserFocusWorld*, 2001.

[PHBF03]   Mark C Peterman, Philip Huie, D M Bloom, and Harvey A Fishman. Building thick photoresist structures from the bottom up. *Journal of Micromechanics and Microengineering*, 13(3):380, 2003.

[PMGS05]   Sophie L. Peterson, Anthony McDonald, Paul L. Gourley, and Darryl Y. Sasaki. Poly(dimethylsiloxane) thin films as biocompatible coatings for microfluidic devices: Cell culture and flow studies with glial cells. *J. Biomed. Mater. Res.*, 72A(1):10–18, 2005.

[PNL+05]   Aigars Piruska, Irena Nikcevic, Se Hwan Lee, Chong Ahn, William R. Heineman, Patrick A. Limbach, and Carl J. Seliskar. The autofluorescence of plastic materials and chips measured under laser irradiation. *Lab Chip*, 5(12):1348–1354, 2005.

[PTA+10]   M. Portaccio, D. Di Tuoro, F. Arduini, M. Lepore, D.G. Mita, N. Diano, L. Mita, and D. Moscone. A thionine-modified carbon paste amperometric biosensor for catechol and bisphenol a determination. *Biosensors and Bioelectronics*, 25(9):2003 – 2008, 2010.

[PWS+07]   Jeng-Hao Pai, Yuli Wang, Gina To'A Salazar, Christopher E. Sims, Mark Bachman, G. P. Li, and Nancy L. Allbritton. Photoresist with low fluorescence for bioanalytical applications. *Analytical Chemistry*, 79(22):8774–8780, 2007.

[PWS+09]   Jeng-Hao Pai, Yuli WANG, Christopher E. SIMS, Nancy BACHMAN, Markand ALLBRITTON, and Guann-Pyng LI. Use of photosensitized epon epoxy resin 1002f for mems and biomems applications, number: Wo/2009/015361, 2009.

[Ric08]   M. Richter. Micropumps from the lab to the fab. *International Conference on New Actuators .11, 2008, Bremen. International*

Exhibition on Smart Actuators and Drive Systems. 5, 2008, Bremen., 2008.

[rik10]   *RIKILT-Institute of Food Safety.* www.rikilt.wur.nl/UK, July 2010.

[RL01]   Robert F. Ritchie and Thomas B. Ledue. The immunoassay handbook, 2nd ed. david wild, ed. new york, ny: Nature publishing group, 2001, 906 pp., hardcover, isbn 0-333-72306-6. *Clin Chem*, 47(10):1876, 2001.

[RMT$^+$05] J.C. Ribeiro, G. Minas, P. Turmezei, R.F. Wolffenbuttel, and J.H. Correia. A su-8 fluidic microsystem for biological fluids analysis. *Sensors and Actuators A: Physical*, 123-124:77 – 81, 2005. Eurosensors XVIII 2004 - The 18th European conference on Solid-State Transducers.

[Ros92]   F.W. D. Rost. *Fluorescence Microscopy. Vol. I.* Press Syndicate of the University of Cambridge, 1992.

[Ros95]   F.W. D. Rost. *Fluorescence Microscopy. Vol. II.* Press Syndicate of the University of Cambridge, 1995.

[RZF07]   Federica Rusmini, Zhiyuan Zhong, and Jan Feijen. Protein immobilization strategies for protein biochips. *Biomacromolecules*, 8(6):1775–1789, 2007.

[SA09]   Yaduvir Singh and Swarajya Agnihotri. *Semiconductors Devices.* I.K. International Publishing House Pvt. Ltd. S-25, Green Park Extension Uphaar Cinema Market New Delhi 110 016 (India), 2009.

[SHG$^+$03] F.Y. Shih, B.R. Harkness, G.B. Gardner, J.S. Alger, M.R. Cummings, J.L. Princing, H. Meynen, H.A. Nguyen, and W.W. Flack. Photopatternable silicone compositions for electronics packaging applications. In *Electronic Packaging Technology Proceedings, 2003. ICEPT 2003. Fifth International Conference on DOI - 10.1109/EPTC.2003.1298749*, pages 316–320, 2003.

[Sig10]   Sigma-Aldrich Co., Copyrights © 2010, www.sigmaaldrich.com. *Sigma Aldrich*, October 2010.

[SK06]   Yi Sun and Yien C. Kwok. Polymeric microfluidic system for dna analysis. *Analytica Chimica Acta*, 556(1):80 – 96, 2006. Young Analytical Faculty in Asia.

[Spu97]   J. H.: Spurk. *Stroemungslehre. Einfuehrung in die Theorie der Stroemungen.*, volume 77. WILEY-VCH Verlag, 1997.

[Sta79]   Bernard Stanford Massey. *Mechanics of fluids.* van Nostrand Reinhold, New York, 4. ed edition, 1979. 21, 543 S.

[Str06]   A. Brent Strong. *Plastics: materials and processing.* Pearson Prentice Hall, 3. ed. edition, c 2006

[SU06]   Arjun P. Sudarsan and Victor M. Ugaz. Multivortex micromixing. *Proceedings of the National Academy of Sciences*, 103(19):7228–7233, 2006.

[SVABC03]   Anke Sanz-Velasco, Petra Amirfeiz, Stefan Bengtsson, and Cindy Colinge. Room temperature wafer bonding using oxygen plasma treatment in reactive ion etchers with and without inductively coupled plasma. *Journal of The Electrochemical Society*, 150(2):G155–G162, 2003.

[SVH$^+$07]   U. Stoehr, P. Vulto, P. Hoppe, G. Urban, and H. Reinecke. Laminierbarer, hochauflösender permanentphotolack für mems-anwendungen. In *MikroSystemTechnik KONGRESS 2007, Dresden (Deutschland), 10-17 Oktober 2007*, Oct 2007.

[T. 08]   Greg T. Hermanson. *Bioconjugate techniques.* Elsevier Acad. Press, Amsterdam [u.a.], 2. ed. edition, 2008.

[TF05]   Santeri Tuomikoski and Sami Franssila. Free-standing su-8 microfluidic chips by adhesive bonding and release etching. *Sensors and Actuators A: Physical*, 120(2):408 – 415, 2005.

[thi10]   thinXXS Microthechnology AG, thinXXS Microtechnology AG ist zertifiziert nach DIN EN ISO 9001 und DIN EN ISO 13485, www.thinxxs.de. *thinXXS Microthechnology AG*, October 2010.

[TL02]   Jr-Hung Tsai and Liwei Lin. Active microfluidic mixer and gas bubble filter driven by thermal bubble micropump. *Sensors and Actuators A: Physical*, 97-98:665 – 671, 2002.

[TP82]   Josef Tsau and John W. Poole. Stoichiometric analysis by chromatographie techniques i. analysis of some antioxidants and penicillins by hplc methods. *International Journal of Pharmaceutics*, 12(2-3):185–197, October 1982.

[ttz10]   *Technology-Transfer-Zentrum.* www.ttz-bremerhaven.de, July 2010.

[Tuo07]   S. Tuomikoski.   *FABRICATION OF SU-8 MICROSTRUC-*
             TURES FOR SU-8 ANALYTICAL MICROFLUIDIC APPLI-
             CATIONS.   Doktorarbeit, Department of Electrical and Com-
             munications Engineering Micro and Nanosciences Laboratory,
             Helsinki University of Technology, February, 2007.

[UCZ+93]   Shunichi Usami, Hsuan-Hsu Chen, Yihua Zhao, Shu Chien, and
             Richard Skalak. Design and construction of a linear shear stress
             flow chamber. *Annals of Biomedical Engineering*, 21:77–83, 1993.
             10.1007/BF02368167.

[Voi10]   Anja Voigt.   Complex micro-optical systems based on uv
             curing polymers on glass. In *Workshop Alternative patterning*
             methods for the manufacture of optical components and systems
             (ACAPOLY), 3. 9. 2010, Berlin, Germany, September 2010.

[Vre11]   Andrej Vrecko. Deliverable report d11: Optical detection system.
             Technical report, NANODETECT project. OPTOTEK d. o. o.,
             Laser and optical technology, 2011.

[Wat]   Michael A. Wattiaux.   *Milk composition and nutritional*
             value. Babcock Institute for International Dairy Research and
             Development, University of Wisconsin-Madison.

[WDZ+07]   Ferdinand Walther, Polina Davydovskaya, Stefan Zuercher,
             Michael Kaiser, Helmut Herberg, Alexander M Gigler, and
             Robert W Stark.   Stability of the hydrophilic behavior of
             oxygen plasma activated su-8. *Journal of Micromechanics and*
             Microengineering, 17(3):524, 2007.

[WFS+01]   M. B. Wabuyele, S. M. Ford, W. Stryjewski, J. Barrow, and
             S. A. Soper.   Single molecule detection of double-stranded
             dna in poly(methylmethacrylate) and polycarbonate microfluidic
             devices. *ELECTROPHORESIS*, 22(18):3939–3948, 2001.

[WIHM02]   Hengzi Wang, Pio Iovenitti, Erol Harvey, and Syed Masood. Opti-
             mizing layout of obstacles for enhanced mixing in microchannels.
             Smart Materials and Structures, 11, Issue 5(1):662–667, 2002.
             Proceedings of the Eleventh International Meeting on Chemical
             Sensors IMCS-11 - IMCS 2006, IMCS 11.

[XL06]   Xiangchun Xuan and Dongqing Li.   Particle motions in

low-reynolds number pressure-driven flows through converging-diverging microchannels. *Journal of Micromechanics and Microengineering*, 16(1):62, 2006.

[XZZC09] Yi Xu, Wenpin Zhang, Ping Zeng, and Qiang Cao. A butyl methacrylate monolithic column prepared in-situ on a microfluidic chip and its applications. *Sensors*, 9(5):3437–3446, 2009.

[YB61] RS YALOW and SA BERSON. Immunological specificity of human insulin: application to immunoassay of insulin. *J Clin Invest*, 40:2190–8–, December 1961.

[YHH⁺06] Sung-Yi Yang, Suz-Kai Hsiung, Yung-Ching Hung, Chen-Min Chang, Teh-Lu Liao, and Gwo-Bin Lee. A cell counting/sorting system incorporated with a microfabricated flow cytometer chip. *Measurement Science and Technology*, 17(7):2001, 2006.

[YLGL09] Ling Yu, Yingshuai Liu, Ye Gan, and Chang Ming Li. High-performance uv-curable epoxy resin-based microarray and microfluidic immunoassay devices. *Biosensors and Bioelectronics*, 24(10):2997 – 3002, 2009.

Acknowledgment

First of all, I would like to thank Prof. Walter Lang, who facilitated this thesis at IMSAS.

Further I would like to thank Prof. Carsten Harms and his team of researchers of ttz/BIBIS, especially Anna Lena Schomacker, who complemented this thesis and its previous research projects within the biological application.

I also would like to thank Prof. Anheier and Prof Vellekoop for assessing this thesis.

Furthermore I would like to thank everyone who supported, motivated or helped me in one way or another along the rocky road to this thesis.

My special thanks to Sven, for his love, support and patience during the past years it has taken me to finish my thesis.

My infinite thanks go to my lovely family, who enabled me to reach so far.